The study of peptide ion channels by electrochemical techniques

Jackson, Thomas James

The Study of Peptide Ion Channels by Electrochemical Techniques

Thomas James Jackson

A thesis submitted in part fulfilment
of the requirements for the degree of
Doctor of Philosophy.

Department of Chemistry
Durham University

September 2007

The Study of Peptide Ion Channels by Electrochemical Techniques

Thomas James Jackson

Abstract

The synthesis of the gramicidin A (gA) analogue gram-2-(nicotinamido)ethyl carbamate (gAN) has been performed. Like gA itself, monomers of the nicotinamide analogue undergo self-assembly in lipid membranes to form K^+ selective transmembrane ion channels. Scanning electrochemical microscopy (SECM) has been used to monitor the movement of permeable ions across these channels under a range of physiological conditions.

Feedback curve results suggest that K^+ ions only pass across the channels when a certain external potential, referred to as the switching potential, is applied to the membrane. This implies that ion transport in the system is controlled by the redox properties of the nicotinamide sub-unit, which acts as a pendant able to occlude the channel opening in the '*ball and chain*' model of inactivation. Chronoamperometric measurements demonstrate that the gAN channel can be repetitively cycled between the opened and closed states. This controllable, predictable switching behaviour has possible applications in membrane transport and drug delivery systems.

The permeability of gAN channels to Tl^+ and Eu^{3+} ions has also been tested by cyclic voltammetry (CV) and electrochemical impedance spectroscopy (EIS) with gold electrode supported lipid bilayers. Results indicate that the channel is permeable to the Tl^+ ion although not to the multicharged Eu^{3+} ion, which is believed to bind occluding the channel entrance. It was also possible to directly monitor the passage of Tl^+ ions across the gAN channel by using Prussian Blue as a dual-purpose electrolyte and electrochromic indicator.

Declaration

The research described in this thesis was undertaken in the Department of Chemistry of Durham University between October 2003 and October 2006. All work is my own, other than where specifically stated otherwise. No part of this work has been submitted previously for a degree at this or any other University.

Statement of Copyright

Table of Contents

Chapter 6: Chronoamperometry and Cyclic Voltammetry

Chapter 7: Scanning Kelvin Nanoprobe and Impedance Spectroscopy

Chapter 8: Conclusions

Appendices

List of Symbols and Abbreviations

Below are listed some of the common symbols and abbreviations used throughout this work. It is not an exhaustive list – any other symbols or abbreviations will be defined as and when they occur in the text.

The usual unit is that commonly used in electrochemical measurements. If a different unit is used in a particular case this will also be indicated in the text.

Symbol	Meaning	Usual Unit
A	Generic reactant	
	Area	cm^2
a	Radius of tip metal disc in SECM	μm
B	Generic product	
C	Capacitance	F
C_{DL}	Double-layer capacitance	F
$[X]$	Bulk concentration of species X	mol cm^{-3}
$[X]_{x=0}$	Surface concentration of species X	mol cm^{-3}
D	Diffusion co-efficient	cm^2 s^{-1}
d	Tip-substrate distance in SECM	μm
E	Electrode potential	V
	Electric field strength	V cm^{-1}
E^{Θ}	Standard electrode potential	V
E_F	Fermi level	eV
E_z	Potential of zero charge	V
e	Elementary charge	1.6022×10^{-19} C
e^-	Electron	
F	Faraday constant	96485.4 C mol^{-1}
f	Frequency	s^{-1}
G	Gibbs free energy	J mol^{-1}
G^{Θ}	Standard Gibbs free energy	J mol^{-1}
i	Current	A
J	Flux	mol cm^{-2} s^{-1}
K	Equilibrium constant	

k_B	Boltzmann constant	1.38066×10^{-23} J K^{-1}
k_f	Heterogeneous rate constant of forwards (oxidation) reaction	cm s^{-1}
k_b	Heterogeneous rate constant of backwards (reduction) reaction	cm s^{-1}
k^o	Standard heterogeneous rate constant	cm s^{-1}
L	Normalised tip-substrate distance in SECM (L = d/a)	
N_A	Avogadro's number	mol^{-1}
n	Stoichiometric number of species	
O	Generic oxidised form of an electroactive species	
Q	Charge	C
q	Charge	C
R	Generic reduced form of an electroactive species	
	Molar gas constant	8.31451 J K^{-1} mol^{-1}
	Resistance	Ω
R_{CT}	Charge-transfer resistance	Ω
R_g	Radius of tip shield in SECM	μm
r	Radius of electrode	cm
T	Absolute temperature	K
t	Time	s
u	Mobility	cm^2 V^{-1} s^{-1}
v	Scan rate	V s^{-1}
	Frequency	s^{-1}
x	Distance from working electrode surface	cm
Z'	Real contribution towards impedance	Ω
Z''	Imaginary contribution towards impedance	Ω
z	Stoichiometric charge	
α	Transfer co-efficient	
β	Esin-Markov co-efficient	
δ	Diffusion layer thickness	cm
ε	Permittivity	C N^{-1} m^{-2}

ε_0	Permittivity of a vacuum	8.854×10^{-12} C N^{-1} m^{-2}
ξ	Zeta potential	V
η	Overpotential	V
θ	Phase angle	rad
λ	Wavelength	m
μ	Chemical potential	J mol^{-1}
σ	Surface charge density	C cm^{-2}
τ	Time period	s
Φ	Work function	eV
ϕ	Electrostatic potential	V
ω	Frequency	rad s^{-1}

Abbrev.	Meaning
AFM	Atomic force microscopy
Ala	Alamethicin
BLM	Bilayer lipid membrane
CA	Chronoamperometry
CD	Circular dichroism
CE	Counter electrode
CV	Cyclic voltammetry
DPV	Differential pulse voltammetry
EIS	Electrochemical impedance spectroscopy
gA	Gramicidin A
gAN	Gram-2-(nicotinamidyl)ethyl carbamate
gD	Gramicidin D
gE	Gramicidin A ethylenediamine
HMDE	Hanging Mercury Drop Electrode
IHP	Inner Helmholtz plane
NPV	Normal pulse voltammetry
OHP	Outer Helmholtz plance
PB	Prussian Blue
PC	Phosphatidylcholine
PTE	Phosphatidylthioethanol

PZC	Potential of zero charge
RE	Reference electrode
RG	Shield / tip ratio in SECM
SAM	Self-assemble monolayer
sBLM	Supported BLM
SECM	Scanning electrochemical microscopy
UME	Ultra microelectrode
UV	Ultraviolet
WE	Working electrode

List of Illustrations

List of Tables

Acknowledgements

I'd like to take this opportunity to thank the many people who have assisted me throughout the work presented in this thesis.

Firstly, I'd like to thank my supervisors, Dr. Ritu Kataky and Dr. John Sanderson, for the invaluable support, advice and assistance they have given me over the past three years.

The other members of the research group, both past and present, also deserve a special mention for all of the advice they have given, poor jokes they have endured and patience they have demonstrated. In particular my thanks go to Aidan Rhodes, for assisting me with Kelvin probe measurements, and Francisco Aguiar, for his hands-on knowledge of the equipment. A special thanks also to my good friends Amit Chakraborty and Anil Suri.

My final words of thanks go to my parents and grandparents. Mum and Dad, thanks for supporting me throughout my years at Durham and just being there when I needed you. Granda, thank you for support and reassurance and Gran, although you're no longer here in person, thanks for all the happy memories and warm, wise words you have provided me over the years.

Chapter 1
Introduction

1.1 Reasons for research

In recent decades synthetic ion channels have attracted considerable attention as nanoscale device candidates[1,2,3] and the catalysis of ion movement across lipid membranes has been achieved in several synthetic systems.[4,5] It is desirable to be able to control this activity by modulating the flow of ions in a predictable manner. Such modulation can be achieved by engineering the channel structure.[6]

Gramicidin A (gA) is a naturally occurring 15-residue polypeptide produced by the soil bacteria *Bacillus brevus*. It is composed of alternating D- and L- amino acids, and forms monovalent cation-selective channels in bilayer lipid membranes (BLMs). The gA molecule possesses an N-terminus formyl group and C-terminus ethanolamine group. A channel is formed when two gA monomers come together in either an entwined double helix (DH) arrangement or head-to-head (N-terminal-to-N-terminal) helical dimer (HD) arrangement. Recent reports indicate the HD form is the principle conducting structure. The internal pore diameter is 3 - 4 Å and the channel length ~ 26 Å.[7]

The structure of gA has been well characterised by both solution-[8] and solid-state NMR,[9] circular dichroism (CD)[10] and X-ray crystallography.[11,12,13] The gA channel is blocked by divalent cations.[14] CD studies show no change in conformation when gA channels are treated with divalent cations.[15] This seems to preclude an allosteric blocking mechanism, and implies a simple steric obstruction of the channel lumen.

The high level of characterisation, understanding of the mode of ion transport and possibility of C-terminal functionality make gA an ideal template for the development of a system of tuneable ion flow. In previous work thermal '*gating*' properties were conferred on gA channels by functionalising the C-terminus with a carbamate-tethered amine group.[6] In the modified channels the pendant amine groups were located at either end of the pore and were able to move freely within the limit of their tether. Depending on the temperature the amine groups were either positioned in free space or so as to occlude the channel openings, thereby blocking the passage of K^+ ions. Four conductance levels were determined, corresponding to the *cis* / *trans* configurations of

the pendant amines on opposite sides of the membrane. Using the same methodology it should be possible to functionalise the C-terminus with some redox active group that will confer potential-dependent opening-closing properties on the gA channel. Such molecular assemblies should find a practical use in membrane transport and drug delivery systems.

In the past patch-clamp[16] techniques have been used for the study of peptide ion channels.[17] This method, whereby a fine electrode is either touched on or through the membrane under investigation, allows the determination of channel currents. Patch-clamp techniques have successfully been used in the determination of the conductance levels of the voltage-gated Na^+ channel,[18,19] but even recent refinements of the technique (such as the *perforated patch*)[20] have the obvious drawback that they are invasive and potentially destructive making it difficult to obtain successive data from the same substrate.

Contrast patch-clamp with scanning electrochemical microscopy (SECM)[21] that is, on the whole, a non-invasive technique although penetration mode measurements can be obtained at various depths in a soft substrate. In SECM a UME is positioned in close proximity to the substrate, approximately 2 or 3 tip diameters from the substrate surface. A potential is applied to the tip, which is then moved relative to the substrate and the current response recorded as a function of tip-substrate position. The micrometer geometry of the tip allows high resolution topographical images to be obtained in lower concentration, higher resistance electrolyte solutions and under ambient conditions.

These characteristics lend SECM and other non-invasive electrochemical techniques to the study of novel peptide ion channels, with the ultimate goal of developing redox controllable nanoscale devices.

1.2 Aims of research

The aims of the research presented in this thesis are:

(a) The design and synthesis of a novel gA analogue with controllable, potential-dependent channel switching properties.

(b) To test the potential-dependent switching properties of the membrane-bound channels by using the non-invasive technique of SECM. Also to observe the effect on channel conduction, if any, of varying electrolyte conditions.

(c) To observe the permeation, if any, of the redox active ions Tl^{+} and Eu^{3+} through the gA and gAN channels by using a combination of SECM, CV and EIS.

1.3 Overview of this thesis

Chapters 2 and 3 give an introduction to the underlying electrochemical principles and techniques used and peptide chemistry that will be the foundation of this investigation. Chapter 2 considers in some detail the structure and properties of the electrode surface interfacial region, the mass transport of electrolyte to the surface and kinetics of the heterogeneous reaction when it arrives there. This chapter also focuses on cyclic and pulse voltammetry, chronoamperometry, scanning Kelvin nanoprobe microscopy (SKN), electrochemical impedance spectroscopy (EIS) and scanning electrochemical microscopy (SECM) – the non-invasive techniques used to characterise peptide ion channel behaviour later on. The role, spectral, structural and functional properties of gA and alamethicin are discussed in detail in Chapter 3. In gAN the C-terminal ethanolamine of gA is functionalised by the addition of an NAD unit. This means it is also pertinent to discuss the redox processes of the introduced NAD(P)/H unit because of its bearing on the synthetic channel's conduction properties.

Chapter 4 goes on to consider the design, synthesis, characterisation and purification of gAN. This nicotinamide-modified peptide was designed as a likely contender for the '*ball and chain*' model of channel inactivation proposed by Armstrong and Benzanilla.[22]

Chapter 5 explains how the SECM feedback curve technique was used to investigate the passage of ions across gA and gAN channels in a variety of electrolyte conditions. Feedback curves were obtained by lowering the UME tip close to peptide treated supported lipid membranes, applying a potential and then gradually retracting the tip as the current response was monitored. The current trend is characteristic of the membrane conducting / insulating behaviour. The affect on the feedback curve current of different membranes was observed when K^{+} was substituted for $N(CH_4)^{+}$ in the supporting electrolyte. Feedback and UV measurements were also used to monitor the passage of

Tl^+ ions across gA and gAN channels. These experiments were performed in Prussian Blue which would serve as a dual-purpose electrolyte and electrochromic indicator.

In Chapter 6 chronoamperometry was used to observe the potential dependent open-closed switching of the membrane inserted gAN channels immersed in a range of electrolyte solutions. The electrode potential was switched between channel open and channel closed extremes, as determined by the earlier SECM feedback curve measurements. CV experiments were performed in order to observe the passage of Tl^+ ions across both gA and gAN peptide channels. This was achieved by the use of gold (electrode) adsorbed bilayers, treated with the peptide of interest and immersed in either K^+ or Tl^+ electrolyte solution.

The final experimental chapter, Chapter 7, provides details of SKN scans of gold-adsorbed bilayers treated with the peptides of interest. The contact potential differences (CPD) of the different lipid environments were measured and compared. As with the earlier CV measurements, EIS data was collected using gold (electrode) adsorbed bilayers, treated with the peptide of interest and immersed in either K^+ or Tl^+ electrolyte solution. In the case of gAN-treated supported bilayers the working electrode was biased at channel open and channel closed extremes and Nyquist and Bode plots obtained. Data was also collected with gA-treated supported bilayers under otherwise identical conditions. The charge transfer resistance, R_{CT}, and double layer capacitance, C_{DL}, of each electrode treatment was calculated. It was also possible to calculate the coverage of the electrode under each experiment condition.

1.4 References

1. C. J. Stankovic, S. H. Heinemann, J. M. Delfino, F. J. Sigworth and S. L. Screiber, *Science*, 1989, **244**, 813
2. M. J. Pregel, L. Jullien, J. M. Lehn, *Angew. Chem. Int. Ed. Engl.*, 1992, **31**, 1637
3. M. R. Ghadiri, J. R. Granja and L. K. Buehler, *Nature*, 1994, **369**, 301
4. N. Voyer, *J. Am. Chem. Soc.*, 1991, **113**, 1818
5. K. S. Akerfeldt, J. D. Lear, Z. R. Wasserman, L. A. Chung and W. F. DeGrado, *Acc. Chem. Res.*, 1993, **26**, 191
6. G. A. Woolley, A. S. I. Jaikaran, Z. Zhang and S. Peng, *J. Am. Chem. Soc.*, 1995, **117**, 4448
7. O. S. Smart, J. M. Goodfellow and B. A. Wallace, *Biophys. J.*, 1993, **65**, 2455
8. A. S. Arseniev, I. Barsukov, V. F. Bystrov, A. L. Lomize and Y. A. Ovchinnikov, *FEBS Lett.*, 1985, **186**, 168
9. R. R. Ketcham, K. -C. Lee, S. Huo and T. A. Cross, *J. Biomol. NMR*, 1996, **8**, 1

10. W. R. Veatch, E. T. Fossel and E. R. Blout, *Biochemistry*, 1974, **13**, 5249
11. B. A. Wallace and K. Ravikumar, *Science*, 1988, **241**, 182
12. D. A. Langs, *Science*, 1988, **241**, 188
13. B. M. Burkhart, R. M. Gassman, D. A. Langs, W. A. Pangborn and W. L. Duax, *Biophys. J.*, 1998, **75**, 2135
14. E. Bamberg and P. Läuger, *J. Membr. Biol.*, 1977, **35**, 351
15. K. He, H. W. Huang and Y. Wu, *Biophys. J.*, 1991, **59**, 318a
16. A. L. Hodgkin and A. F. Huxley, *J. Physiol.*, 1952, **117**, 500
17. O. P. Hamill, A. Marty, E. Neher, B. Sakmann and F. J. Sigworth, *Pflügers Arch.*, 1981, **391**, 85
18. H. Lerche, N. Mitrovic, V. Dubowitz and F. Lehmann-Horn, *Ann. Neurol.*, 1996, **39**, 599
19. N. Mitrovic, A. L. George, R. Heine, S. Wagner, U. Pika, U. Hartlaub, M. Zhou, H. Lerche, C. Fahlke and F. Lehmann-Horn, *J. Physiol.*, 1994, **478**, 395
20. R. Horn and S. J. Korn, *Methods Enzymol.*, 1992, **207**, 149
21. A. J. Bard, G. Denuault, C. Lee, D. Mandler and D. O. Wipf, *Acc. Chem. Res.*, 1990, **23**, 357
22. C. M. Armstrong and F. Bezanilla, *J. Gen. Physiol.*, 1977, **70**, 567

Chapter 2

Electrochemical Principles and Techniques

2.1 The interfacial region

2.1.1 *General overview*

The region where the electrolyte solution meets the working electrode (WE) surface is known as the *interfacial region*. The structure of the interfacial region is of interest as it is the location of electron-transfer processes at the WE surface. The interfacial region can be further sub-divided into the *electrolyte double-layer* and the *space-charge region*. The electrolyte double layer exists in solution in the immediate proximity of the WE surface. The space-charge region exists within the WE itself.

The electrode-electrolyte interface can be considered as the two parallel plates of a capacitor. Changes in WE potential result in the accumulation or depletion of charge on the opposing plates. The ability of the interface to store charge is known as the *capacitance*, C. In the case of a small change in charge density arising from a small change in potential, the *differential capacitance*, C_d, is given by:

$$C_d = \frac{\partial \sigma_m}{\partial E} \qquad (1)$$

where σ_m is the excess charge density on the metal electrode surface. The potential at which the electrode charge density equals the solution charge density at the electrode surface, $\sigma_m = \sigma_s = 0$, is known as the *potential of zero charge* (PZC). The PZC, E_z, is also shown as the minimum on a plot of σ_m against E.

As the value of C_d varies with potential, it is sometimes more appropriate to consider the integral capacitance, C_i. C_i is the average of C_d over the potential range $E_z \leq E$.

$$C_i = \frac{\sigma_m}{(E - E_z)} \qquad (2)$$

2.1.2 *Electrolyte double-layer*

2.1.2.1 *Initial proposal: the Helmholtz model*

The double layer model proposed by H. L. F. von Helmholtz considers ions as hard spheres in solution.[1,2] The hard spheres arrange on both the solid and liquid side of the interface and the charge-charge interactions are confined to this immediate region only. The arrangement of the charges is similar to that in a parallel plate capacitor: one plate is the metal-solution interface and the other the rigid arrangement of oppositely charged ions at the electrode surface. The thickness of the double-layer, x_H, is equal to the ionic radius of the surfaced-ordered ions. The potential difference, E, and differential capacity, C_d, across the double-layer is given by:[1,2]

$$E = \frac{\sigma x_H}{\varepsilon_0 \varepsilon} \tag{3}$$

$$C_d = \frac{\sigma}{E} = \frac{\varepsilon_0 \varepsilon}{x_H} \tag{4}$$

where σ is the uniform charge density on the WE surface, ε_0 the permittivity of free space (8.854×10^{-12} C^2 N^{-1} m^{-2}) and ε the permittivity of the capacitive layer, which is assumed to be independent of distance.

One shortfall of the Helmholtz model, as incorrectly implied in equation 4, is that C is a constant for a given electrode-electrolyte combination. In reality the thickness of the double-layer and capacitance depends on the electrode potential and electrolyte concentration. The model also incorrectly assumes: firstly, that the double-layer is confined to the region immediately above the WE surface and does not extend further into the electrolyte: secondly, that the double-layer ions are unpolarisable, unsolvated point charges.

2.1.2.2 *The Guoy-Chapman model (1913)*

The effects of electrolyte concentration and potential on double-layer capacitance were first taken into account by Guoy and Chapman.[3,4] Contrary to the Helmholtz idea of a rigid arrangement of ions at the WE surface, this model proposes variable double-layer thickness with the presence of a *compact-layer* of ions near the electrode and a *diffuse-layer* towards bulk solution. The sparsity of ions in a dilute electrolyte means the diffuse-layer is thicker than in a more concentrated solution. Conversely, the abundance

of ions in a concentrated electrolyte causes compression of the compact-layer. The distribution of electrolyte ions at a certain distance from the electrode surface is given by the Boltzmann equation:

$$n_i = n_i^0 exp\left(\frac{-z_i e\phi_\Delta}{k_B T}\right) \quad (5)$$

$$\phi_\Delta = \phi - \phi_s \quad (6)$$

where n_i^0 is the number of ions i in bulk solution, z the charge on ions i, ϕ the electrostatic potential at a certain point in the solution, e the electronic charge, k_B the Boltzmann constant and T the Kelvin temperature.

Guoy and Chapman went on to consider the charge density of successive lamellae of solution extending out from the electrode surface. The charge density at distance x from the electrode is given by:

$$\rho(x) = \sum_i n_i z_i e = \sum_i n_i^0 z_i e exp\left(\frac{-z_i e\phi_\Delta}{k_B T}\right) \quad (7)$$

$$\frac{\partial^2 \phi_\Delta(x)}{\partial x^2} = -\frac{\rho(x)}{\varepsilon_r \varepsilon_0} \quad (8)$$

The Boltzmann and Poisson equations (equations 5 and 8) can be combined to form the Poisson-Boltzmann equation:

$$\frac{\partial^2 \phi_\Delta(x)}{\partial x^2} = -\frac{e}{\varepsilon_r \varepsilon_0}\sum_i n_i^0 z_i exp\left(\frac{-z_i e\phi_\Delta}{k_B T}\right) \quad (9)$$

Further integration and rearrangement of the Poisson-Boltzmann equation eventually leads to the Guoy-Chapman equation for double-layer capacitance:[3,4]

$$C_d = \frac{\partial \sigma_m}{\partial \phi_{\Delta,0}} = \sqrt{\left(\frac{2z^2 e^2 \varepsilon_r \varepsilon_0 n_i^0}{k_B T}\right)} cosh\left(\frac{ze\phi_{\Delta,0}}{2k_B T}\right) \quad (10)$$

Although the Gouy-Chapman model improved on Helmholtz's work it still didn't match with experimental data, particularly at very small and large distances from the electrode surface. A significant failure of this model is that ions are still considered as point charges that can approach infinitely close to the electrode surface. In reality, the approach of the ions is limited by their radius. The model is only effective at an electrode potential close to the PZC.

2.1.2.3 *The Stern model (1924)*

Stern, in agreement with Guoy and Chapman, considered that the double-layer consisted of an ordered compact-layer of ions near the electrode, which became increasingly diffuse out towards bulk solution. Stern combined the Helmholtz model for potentials far from E_z with the Guoy-Chapman model for potentials closer to E_z.[5] The overall capacitance of the interface is considered to be a combination of Helmholtz and Guoy-Chapman capacitors in series:

$$\frac{1}{C_d} = \frac{1}{C_{d,H}} + \frac{1}{C_{d,GC}} \qquad (11)$$

$$\frac{1}{C_d} = \frac{x_H}{\varepsilon_0 \varepsilon} + \frac{1}{\sqrt{\left(\frac{2\varepsilon_r \varepsilon_0 z^2 e^2 n_i^0}{k_B T}\right)} \cosh\left(\frac{ze\phi_{\Delta,0}}{2k_B T}\right)} \qquad (12)$$

The plane between the compact and diffuse layers is known as the *outer Helmholtz plane* (OHP).

2.1.2.4 *The Graham model (1947)*

Graham proposed the presence of *specifically adsorbed* ions at the electrode surface.[6] Specifically adsorbed ions are either partly or fully unsolvated and are bound directly to the electrode surface. They can have either the same or opposite charge as the electrode, but are attracted much more strongly than their solvated counterparts.

The extent of specific adsorption is dependent on the electrolyte concentration and effects E_z. Variation of E_z with concentration is known as the *Esin-Markov* effect.[7] Under Esin-Markov conditions a plot of E_z against the natural logarithm of the electrolyte activity is linear. The slope gives the *Esin-Markov co-efficient*, β. An example Esin-Markov plot and data are shown in Table 1.

$$\beta = \frac{1}{RT}\left(\frac{\partial E_z}{\partial \ln a_{salt}}\right)_{\sigma_m} = \left(\frac{\partial E_z}{\partial \mu_{salt}}\right)_{\sigma_m} \qquad (13)$$

Table 1. *Potassium iodide: an example of iodide specific adsorption.*[6]

[KI]/ M	E_z/ V vs. SCE
1.0	-0.82
0.1	-0.72
0.01	-0.66
0.001	-0.59

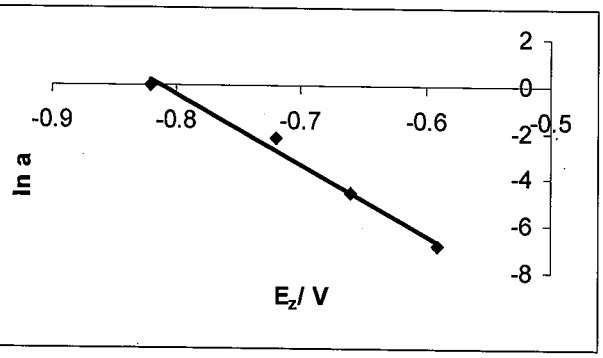

Specific adsorption of anions is indicated by a decrease in E_z with concentration increase. Specific adsorption of cations is indicated by an increase in E_z with concentration increase. No specific adsorption is present if $\beta = 0$.

The imaginary plane that passes through the centre of the specifically adsorbed ions is known as the *inner Helmholtz plane* (IHP).

2.1.2.5 *The Bockris, Devanathan and Müller model (1963)*

The Bockris, Devanathan and Müller model consolidates many of the ideas of the previous models, but also considers the effect of solvent on the interface.[8] As the concentration of solvent is much greater than that of solute there will be a predominance of solvent molecules at the interface. In the case of a polar solvent, the molecular dipoles arrange at the charged electrode surface. Specifically adsorbed ions are also present with the solvent in the IHP.

The layer after the IHP comprises an ordered arrangement of non-specifically adsorbed ions, which remain solvated. This is the OHP. The diffuse-layer comes after the OHP. At a certain distance from the electrode the ordering of the ions fails. The potential of this plane is known as the zeta potential, ξ.

2.1.3 *The space-charge region*

In metals the space charge region is very narrow and consideration can be confined to the movement of electrons to and from the metal surface. There are several useful reviews about band theory and conductor, semi-conductor and insulator properties,[9,10] but these are beyond the scope of this chapter. Instead an introduction to the work function and Kelvin probe, relevant to our work in Chapter 7, is provided.

The work function, Φ, of a conducting material is defined as the minimum energy required to remove an electron from the Fermi level, E_F, through the surface, to a point infinitely far away. In 1898 Scottish scientist William Thomson, latterly known as Baron Kelvin of Largs, described a method of determining the value of Φ.[11] In a lecture to the Royal Institution Kelvin demonstrated that an electrical potential exists between the surfaces of two conducting plates when they are brought into contact. Electrons flow between the plate of higher work function and lower work function, creating a *contact potential difference* (CPD).

The traditional Kelvin method of determining work functions relies on a flat reference electrode suspended above a sample electrode. A capacitive charge builds up between the two surfaces and the CPD can be measured. Unfortunately, this method can not be used for continuous scans due to the need for charge dissipation between successive measurements. A method was developed by Zisman that could cope with changes in CPD over time or distance. Zisman developed a Kelvin probe utilising a vibrating reference tip above a stationary sample.[12] As the tip vibrated the potential changed periodically causing a variation of capacitance between the tip and sample. This allows the continuous measurement of CPD – the underlying principle of the modern-day Kelvin probe.

Recall that the work function, Φ, is the energy required to move an electron from the Fermi level, E_F, to a point infinitely far away outside the conducting material. Consider two conducting metals, with Fermi levels E_{F1} and E_{F2} and work functions Φ_1 and Φ_2, with complete electrical separation (Figure 1(a)). When the surfaces are brought into electrical contact their Fermi levels equalise, corresponding to a change in work function as electrons flow from Φ_1 to Φ_2 (Figure 1(b)). By analogy to a capacitor, equal and opposite charges are present on the surfaces of the two metals. The difference between the work functions of the two metals is known as the contact potential, V_C. The

contact potential can be measured by applying a backing potential, V_B, to the probe tip (Figure 1(c)). The backing potential at zero net charge is equal to $-V_C$, allowing the contact potential to be easily calculated.

Figure 1. *The role of Fermi levels and work functions in the Kelvin probe.*

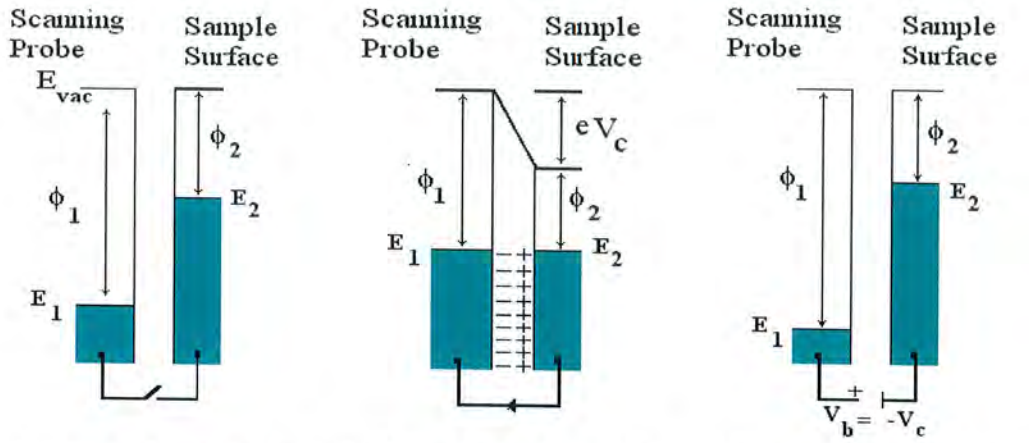

(a) Probe tip and sample surface of differing E_F and Φ.

(b) Tip and surface brought into contact.

(c) Backing potential applied to sample surface.

With a vibrating tip, as in Zisman's system, the capacitance is given by the following equation:

$$C = \frac{Q}{V} = \frac{\varepsilon_0 A}{d} \qquad (14)$$

where C is the capacitance, Q the charge, V the potential, A the tip surface area, ε_0 the permittivity of the dielectric (usually free space) and d the distance between the capacitor plates (the tip and substrate). As the tip is vibrating the tip-substrate distance, therefore capacitance is constantly changing. The capacitance increases as the tip gets closer to the substrate and decreases as the tip is retracted. As the charge on the plates and work functions are constant values, the changing capacitance with tip vibration must be due to potential variation. The voltage appears as a sinusoidal waveform, with a peak to peak voltage, V_{PTP}, given by:

$$V_{PTP} = (\Delta V - V_B) R C_0 \omega \varepsilon \sin(\omega t + \phi) \qquad (15)$$

where ΔV is the potential difference between the tip and substrate, V_B is the backing potential, R is the converter resistance, C_0 is the probe capacitance, ω is the angular frequency of vibration, ϕ is the phase angle, t is the time and ε is a parameter known as the *modulation index*. The value of $\varepsilon = d_1 / d_0$ where d_1 is the mean tip-substrate distance and d_0 the amplitude of vibration.

When $V_{PTP} = 0$ the value of $V_B = -V_C$. The vibrating tip has the advantage of being able to determine contact potentials and work functions continuously, without the need for capacitive discharge between measurements. This makes the probe ideally suited for microscopy and collecting data over a longer duration. In addition to the CPD values topographical information can be obtained by measuring the capacitance, which is inversely proportional to tip-substrate distance, throughout the tip vibration. Work function values obtained by the Kelvin probe are not absolute values, but relative to the work function of the probe.

Applications of the Kelvin probe are discussed in more detail in Chapter 7.

2.2 Mass transport

2.2.1 *General overview*

Ions in the electrolyte solution can move between the anode and cathode by three different modes of transport: *diffusion, migration* and *convection.* Each mode of mass transport contributes to the total observed current, i_t, at the WE.

$$i_t = i_d + i_m + i_c \qquad (16)$$

Diffusion is the spontaneous movement of electrolyte species from a region of high concentration to a region of lower concentration. Migration is the movement of charged particles under the influence of an electric field. Neutral particles do not undergo migration. Convection is due to the forced movement of electrolyte solution either mechanically, as in the case of hydrodynamic experiments, or naturally, due to a temperature-induced density gradient within the solution.

Experimental conditions are usually adjusted to favour a particular mode of mass transport. For example, the addition of a large excess of ionic salt, known as *supporting electrolyte*, to the electroactive species results in the damping out of migration effects.

Measurements performed in a controlled-temperature, vibration-free environment have minimal convection. *Hydrodynamic* experiments, where the WE is rotated in the electrolyte solution, have a greatly enhanced convection contribution.

2.2.2 *Diffusion*

Diffusion is the movement of a species from a region of high concentration to a region of lower concentration. The flux, J, is a common measure of the rate of mass transport at a given point at the electrode surface. The flux is related to the electrode current by:

$$i = -nAFJ \qquad (17)$$

For one-dimensional diffusion, as is the case for diffusion to a macroelectrode, the flux is related to the concentration gradient according to Fick's laws:[13,14]

$$J_d = -D(\nabla[A]) \qquad (18)$$

$$\nabla = \frac{\partial}{\partial x} \;\&\; \nabla^2 = \frac{\partial^2}{\partial x^2} \qquad (19)$$

$$\frac{\partial[A]}{\partial t} = D(\nabla^2[A]) \qquad (20)$$

The observed current depends on the diffusion co-efficient, D, which depends on the solvent used, the molecular weight and size of the electroactive species and the temperature. The del-operator, ∇, and the Laplacian, ∇^2, are defined by the symmetry of the electrode surface. The combination of equations 17 and 18 gives the general expression for current response:

$$i = nFAD\frac{\partial[A]}{\partial x} \qquad (21)$$

2.2.3 *Migration*

In bulk solution, far from the electrode surface, concentration gradients are negligible and mass transport is mainly due to migration of charged species, A, under the influence of a potential, E. As previously mentioned, neutral species do not contribute to migration. The total migrational flux, J_m, is the sum of the individual fluxes:

$$J_m = \sum_A -\frac{z_A F}{RT} D_A [A] \frac{\partial E}{\partial x} \quad (22)$$

$$J_m = \sum_A -\frac{z_A F}{RT} D_A [A] (\nabla E) \quad (23)$$

The mobility, u, of a charged species is related to the diffusion co-efficient by the *Einstein-Smoluchowski* equation:[15]

$$u_A = \frac{|z_A| F D_A}{RT} \quad (24)$$

The magnitude and direction of a migration current depends on the charge on the ion. In the absence of convection an anion will diffuse to a negatively charged WE, but will simultaneously migrate to a positively charged CE. The observed i_d will therefore be cancelled out by the opposing i_m. The addition of supporting electrolyte reduces the i_m contribution, hence causing amplification of the observed i_d.[16]

2.2.4 *Convection*

The bulk flow of electrolyte can occur due to either mechanical stirring, called *forced convection*, or temperature induced density gradients, called *natural convection*. The convectional flux is given by:

$$J_c = [A] v \quad (25)$$

where v is the velocity vector (the component of velocity in a particular direction). In hydrodynamic experiments convection is the major form of mass transport.

2.2.5 *The Nernst-Planck equation*

The equations for diffusion, convection and migration can be combined to give an overall equation for the spatial variation of each species. The *Nernst-Planck* equation is given by:

$$\frac{\partial [A]}{\partial t} = D\nabla^2 [A] - v\nabla [A] + \frac{z_A F}{RT} D\nabla([A]\nabla E) \quad (26)$$

The *Nernst-Planck* equation describes how the concentration at a given point varies through time due to diffusion, convection and migration.

2.2.6 *Microelectrodes*

Microelectrodes (also known as ultramicroelectrodes (UMEs)) are electrodes that have one dimension of < 20 μm. The simplest and most popular microelectrode is the microdisc electrode, which is fabricated by sealing a fine wire or carbon fibre in a glass or plastic capillary and polishing the end. Microelectrodes differ from conventionally sized electrodes by virtue of their increased current density, lower capacitive charging and reduced ohmic drop. These characteristics make microelectrodes particularly useful for experiments in resistive media[17] or in the absence of supporting electrolyte,[18] so they particularly lend them self to *in vivo* measurements in biological systems.[19,20]

In diffusion-controlled experiments macroelectrodes have one-dimensional diffusion normal to the plane of the surface, whereas microelectrodes have one-dimensional diffusion only for the short time after electrolysis when the diffusion layer thickness is small compared to the electrode surface area. At subsequent times, as the diffusion layer expands, non-linear (convergent) diffusion occurs at the microelectrode edges resulting in enhanced current density. Unlike macroelectrodes the convergent contribution means that current does not scale with electrode area. As the capacitive charging current is small, much faster scan rates are possible in potential-sweep techniques like CV.

The flux and concentration gradient at the microdisc electrode is given by:[21]

$$J_d = -D(\nabla[A]) \qquad (18)$$

$$\nabla^2 = \frac{\partial^2[A]}{\partial x^2} + \frac{\partial^2[A]}{\partial r^2} + \frac{1}{r}\cdot\frac{\partial[A]}{\partial r} \qquad (27)$$

$$\frac{\partial[A]}{\partial t} = D(\nabla^2[A]) \qquad (20)$$

The steady-state limiting current of a microdisc electrode is given by:

$$i_{ss} = 4nFD[A]_{bulk}r \qquad (28)$$

Recall from section 2.1.2 that the electrode-electrolyte interface consists of an array of highly ordered molecules at the electrode surface. This arrangement is analogous to the parallel plates of a capacitor. When a potential is applied to the electrode the resulting current has both a Faradiac and capacitive contribution. In a potential-step experiment the capacitive current, i_C, is given by the following equation:

$$i_C = \frac{\Delta E}{R} exp\left(\frac{-t}{RC}\right) \qquad (29)$$

In this case R is the solution resistance which is independent of the electrode area and C is the double layer capacity which is proportional to the electrode area. The product RC is sometimes referred to as the cell time constant.

Since C is proportional to the electrode area the value of RC decreases with electrode radius. This results in microelectrodes displaying a much quicker response to potential perturbations than their macroscopic counterparts. The increased rate of mass transport means reactions that display electrochemical reversibility at macroelectrodes (fast electron-transfer) may show *quasi-* or *irreversible* electrode kinetics at microelectrodes.

2.3 **Electrode kinetics**

2.3.1 *General overview*

Electrochemical processes are composed of two different reaction types: *heterogeneous* reactions and *homogeneous* reactions.

Heterogeneous electrochemical reactions involve electron-transfer between two species in an electrochemical couple. The process usually occurs at the working electrode surface, when electrons transfer between the solid-state electrode and solution-state electroactive species. Heterogeneous chemical reactions, such as dissolution or surface adsorption, may also occur.

Homogeneous electrochemical reactions involve species in the solution-state. They can be further classified as first order, involving a single species (e.g. isomerisations), or second order, involving two species (e.g. collisional interactions).

2.3.2 *Heterogeneous electrochemical reactions*

Consider the following simple one-electron reduction process:

$$A + e^- \underset{k_b}{\overset{k_f}{\rightleftharpoons}} B \qquad (30)$$

Recall from section 2.2.2 that the general expression relating the current response to the reactant concentration gradient is given by:

$$i = nFAD\frac{\partial[A]}{\partial x} \qquad (21)$$

The rate constants can be incorporated into equation 21 to give the following analogy:

$$i = nFA\left(k_b[B] - k_f[A]\right) \qquad (31)$$

Butler[22] and Volmer[23] derived a pair of expressions that relate the rate constants, k_f and k_b, with the reversible formal potential, E_f^0, a standard rate constant, k^0, and a transfer co-efficient, α. The *transfer coefficient* has a value between zero and unity and describes the slope of the transition-state energy profile. It influences the shape, although not the position, of the voltammetric response. The transfer co-efficient has a typical value of 0.5. Note that the nomenclature E_f^0 is used instead of E^0 because the measurements are not usually performed under standard conditions of unit activity, temperature and pressure.

$$k_f = k_0 exp\left(\frac{-\alpha nF\left(E - E_f^0\right)}{RT}\right) \qquad (32)$$

$$k_b = k_0 exp\left(\frac{(1-\alpha)nF\left(E - E_f^0\right)}{RT}\right) \qquad (33)$$

The rate constants are related to the current by the Butler-Volmer equation:[22,23]

$$i = nFAk_0\left[[A]_{x=0} \exp\left(\frac{-\alpha nF\left(E - E_f^0\right)}{RT}\right) - [B]_{x=0} \exp\left(\frac{(1-\alpha)nF\left(E - E_f^0\right)}{RT}\right)\right] \quad (34)$$

As indicated by equation 34 when the system is in equilibrium $k_f[A] = k_b[B]$ there is no overall current. The absence of current indicates that there is no concentration gradient and therefore $[A]_{x=0} = [A]_{bulk}$. Remembering that $\alpha \sim 0.5$ for heterogeneous transfer at a metal electrode surface:

$$[A]\exp\left(\frac{-\alpha nF\left(E - E_f^0\right)}{RT}\right) = [B]\exp\left(\frac{(1-\alpha)nF\left(E - E_f^0\right)}{RT}\right) \quad (35)$$

$$\exp\left(\frac{nF\left(E - E_f^0\right)}{RT}\right) = \frac{[A]}{[B]} \quad (36)$$

$$E = E_f^0 + \frac{RT}{nF} ln\frac{[A]}{[B]} \quad (37)$$

The calculation of heterogeneous rate constants from CV data is considered further in Chapter 6.

2.3.3 *Homogeneous electrochemical reactions*

Quite often a heterogeneous electron-transfer process is accompanied by a homogeneous chemical reaction involving the products and/or reactants. The E and C notation introduced by Testa and Reinmuth[24] is a convenient method of classifying a sequence of heterogeneous (E) and homogeneous (C) processes. A detailed explanation of these processes in beyond the scope of this review because our experiments focus primarily on electron-transfer at the electrode surface. The main homogeneous reaction sequences and their corresponding rate equations are shown in Table 2.

Table 2. *Summary of key homogeneous reactions (adapted from reference 25)*

Reaction	Steps	Rate Equation
E	$A + e^- \longrightarrow B$	*Not applicable*
EC	$A + e^- \longrightarrow B$ $B \xrightarrow{k} C$	$\frac{\partial[B]}{\partial t} = -k[B]$ & $\frac{\partial[C]}{\partial t} = k[B]$

ECE	$A + e^- \longrightarrow B$ $B \xrightarrow{k} C$ $C + e^- \longrightarrow D$	$\frac{\partial[B]}{\partial t} = -k[B]$ & $\frac{\partial[C]}{\partial t} = k[B]$
CE	$A \underset{k_b}{\overset{k_f}{\rightleftharpoons}} B$ $B + e^- \longrightarrow C$	$\frac{\partial[A]}{\partial t} = -k_f[A] + k_b[B]$ & $\frac{\partial[B]}{\partial t} = k_f[A] - k_b[B]$
DISP1	$A + e^- \longrightarrow B$ $B \xrightarrow{k} C$ $B + C \longrightarrow A + D$	$\frac{\partial[A]}{\partial t} = k[B]$ & $\frac{\partial[B]}{\partial t} = -k[B]$
DISP2	$A + e^- \longrightarrow B$ $B \longrightarrow C$ $B + C \xrightarrow{k} A + D$	$\frac{\partial[A]}{\partial t} = k[B]^2$ & $\frac{\partial[B]}{\partial t} = -2k[B]^2$
EC'	$A + e^- \longrightarrow B$ $B + S \xrightarrow{k} A$	$\frac{\partial[A]}{\partial t} = k[B][S]$ & $\frac{\partial[B]}{\partial t} = -k[B][S]$
C	$B \underset{k_b}{\overset{k_f}{\rightleftharpoons}} C$	$\frac{\partial[B]}{\partial t} = -k_f[B] + k_b[C]$ & $\frac{\partial[C]}{\partial t} = k_f[B] - k_b[C]$

2.4 Voltammetry for the study of electron-transfer processes

2.4.1 *Cyclic voltammetry*

Cyclic voltammetry (CV) is a widely used method of acquiring qualitative information about electrochemical reactions.[26] CV is particularly useful for obtaining information about the thermodynamics of redox reactions, the kinetics of heterogeneous electron-transfer, coupled chemical reactions and adsorption processes. The ease of determining the redox potentials of electroactive species, and the ability to monitor the effect of media on redox processes, often makes CV the first method of choice in electroanalytic study.

2.4.1.1 *Basic principles*

Three electrodes are immersed in a solution of the electroactive species of interest: the working electrode (WE), reference electrode (RE) and counter electrode (CE).

The WE potential is measured relative to the RE potential by a potentiostat. For a given temperature and type of RE, the potential is fixed and known. The RE is connected to the potentiostat by a very high resistance circuit, preventing current flow in that electrode. The CE acts as a sink of electrons, completing the electrochemical circuit. Current flows between the WE and CE via the electroactive species in solution.

An initial potential, E_0, is applied to the WE and the potential is then swept to a second value, E_f. The potential is then swept back from E_f to E_0. This cycle can be repeated as shown in Figure 2, depending on the type of experimental data sought. The variation of WE potential with time, takes the shape of a triangular waveform.

Figure 2. *Variation of working electrode potential with time.*

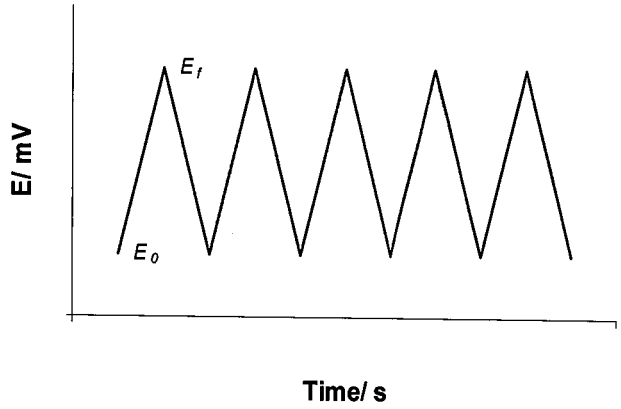

During the potential sweep the WE current is measured by the potentiostat. Data is logged on a personal computer. At the end of the sweep or series of sweeps the computer or data recorder draws a plot of WE current against potential. This plot is called a *cyclic voltammogram.*

2.4.1.2 *Practical considerations*

These considerations apply equally to CV and the other voltammetric techniques.

The CV experimental conditions are such that mass transport of the electroactive species occurs by diffusion only. A background electrolyte is usually added in order to avoid migration currents and maintain conductivity. Measurements are performed in unstirred solution to avoid mechanically induced convection currents. Additionally, the cell can be water-jacketed and the temperature thermostatically controlled to minimise natural convection. The cell must also be kept away from sources of vibration. The

polarisability and solubility of tetraalkylammonium salts makes them a suitable supporting electrolyte for organic solvents. Simple alkali metal salts or buffers are usually the supporting electrolyte of choice in aqueous systems.

The concentration of the electroactive species is usually between 10^{-3} and 10^{-5} M and the background electrolyte one hundred times greater. Heterogeneous electron transfer at the interfacial region creates a *Faradaic* current, due to the formal transfer of electrons between the electroactive species and WE surface. The ordering of oppositely charged ions at the WE also gives rise to a capacitive charge build-up at the electrical double-layer. Any change in WE potential will result in a capacitive discharge of the double-layer, and associated *non-Faradaic* contribution to the WE current.

It is important that high purity samples and electrolytic solution are used. The slightest trace of contamination can be detrimental to the success of CV experiments. For aqueous solutions the usual procedure is to remove oxygen, which is reducible between -0.8 and -0.2 V against the saturated calomel electrode (SCE). For aprotic solvents purification needs to be applied much more stringently. Several effective procedures have been developed for removing protic impurities such as water.[27,28,29] In practice it is not possible to completely remove water from aprotic solvents and the walls of the cell. Hammerich and Parker developed a technique of creating a super-dry environment within the cell,[30] involving the direct addition of superactive alumina. Early alumina drying attempts were found to be incompatible with certain sensitive analytes. Use specially designed cells, like those designed by Kiesele, can counteract this problem.[31]

The smoothness and cleanliness of the working electrode surface must be perfectly reproduced between experiments to avoid high background currents and noise. This is achieved by systematic polishing with diamond or alumina slurry.[32]

The flow of current between the WE and CE is affected by the resistance of the electrolyte solution, R_u. In addition to the applied WE potential the observed cell potential includes components due to this solution resistance and the liquid junction potential, discussed below.

$$E_{obs} = E_{app} + IR_u + E_{ljp} \qquad (38)$$

In order to minimise the IR_u term, also referred to as the *ohmic drop* of the electrolyte, the WE and RE are positioned as close to each other as possible. The internal circuitry of the potentiostat minimises the electrolyte ohmic drop further by driving the potential between the WE and CE to a compensating level.[33] The internal resistance of the potentiostat electronic circuitry, WE and CE also contribute to a potential loss.

The silver / silver chloride (Ag/AgCl) electrode (equation 39) is usually the RE of choice because of ease of preparation, non-toxicity and stability of the potential. This has overtaken the saturated calomel electrode (SCE),[34] which has the main disadvantage of containing mercury (equation 40).

$$AgCl + e \rightleftharpoons Ag + Cl^- \qquad (39)$$

$$1/2\ HgCl_2 + e \rightleftharpoons Hg + Cl^- \qquad (40)$$

To prevent the RE filling solution from contaminating the WE solution, the two phases are separated by a porous glass sinter or frit. The potential drop associated with the separation is known as the *liquid-junction potential,* E_{ljp}. E_{ljp} is compensated for by the introduction of a salt bridge. E_{ljp} arises from the different ionic mobilities of the separated phases. In order to minimise E_{ljp} the bridge is soaked in a salt containing a cation and anion of approximately equal ionic mobilities. The approximately equal but opposite migration of the liquid-junction ions cancels out much of the E_{ljp}.

2.4.1.3 *Electron-transfer processes*

The cyclic voltammogram for the reversible one-electron oxidation of ferrocene to ferricinium is shown in Figure 3. The shape of the voltammogram is very distinctive, and characteristic of a reversible process.

Figure 3. *Reversible one-electron oxidation: Cp_2Fe to Cp_2Fe^+.*

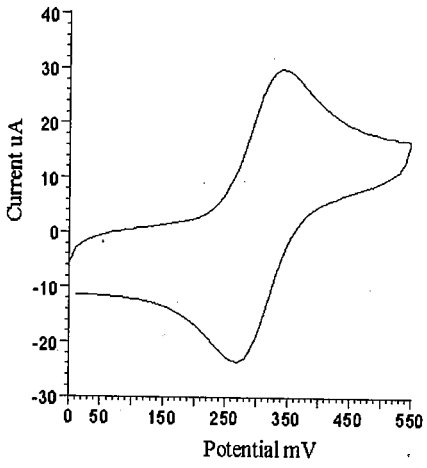

Cyclic voltammogram of ferrocene carboxylic acid in pH 7 phosphate buffer. Scan rate = 400 mVs^{-1}.

For a macroelectrode diffusion of the electroactive species occurs in one-dimension, perpendicular to the electrode surface. Consider the following simple one electron oxidation process where A is the oxidised reactant and B is the reduced product:

$$A + ne^- \rightleftharpoons B \qquad (41)$$

The current is given by:

$$i = nFAD\left(\frac{\partial[A]}{\partial x}\right)_{x=0} \qquad (21)$$

Initially only species A is present at an electrode surface concentration $[A]_{x=0}$. As the WE potential is swept from E_0 towards E_f the value of $[A]_{x=0}$ decreases due to reduction of A and formation of B. During the sweep $[A]_{x=0}$ is depleted, $\partial[A]/\partial x$ increases, J_A increases and therefore i increases. Eventually the value of $[A]_{x=0}$ becomes zero and i reaches a maximum, i_p. Any further increase in E results in the expansion of the *Nernst diffusion layer*. As the Nernst diffusion layer expands the distance between unreacted A and the WE surface increases and J_A and i decrease. An identical process for the oxidation of B back to A occurs when the WE potential sweep is reversed.

Some important parameters can be deduced from the shape and magnitude of a cyclic voltammogram. For a reversible electron-transfer process, one with rapid heterogeneous kinetics, the oxidative (anodic) peak potential, E_{pa}, and the reductive (cathodic) peak

potential, E_{pc}, have $57/n$ mV separation. The ratio of anodic and cathodic peak currents, $i_{pa}/i_{pc} = 1$. The *Randles-Sevcik equation* provides a convenient way of calculating i_p for a reversible couple at 298 K:

$$i_p = (2.69 \times 10^5) n^{3/2} A D_A^{1/2} \nu^{1/2} [A]_{bulk} \qquad (42)$$

where A is the electrode area (cm^2), $[A]_{bulk}$ is the bulk concentration (mol cm^{-3}), D_A is the diffusion coefficient ($cm^2\ s^{-1}$) and ν is the scan rate ($V\ s^{-1}$).

2.4.2 *Pulse voltammetry*

In pulse voltammetry (PV) a potential step is applied to the WE and the resulting current measured. The PV techniques were originally intended for measurements with the dropping mercury electrode (DME), with the intention of synchronising potential pulses with drop growth. The diffusion layer was renewed when the drop fell between measurements. During the potential step the capacitive contribution to the current dies down much faster than the Faradaic contribution, so current measurement is delayed until towards the end of the pulse.

2.4.2.1 *Normal pulse voltammetry*

In normal pulse voltammetry (NPV) a potential baseline, E_{bl}, at which no Faradaic process occurs, is applied to the WE. At regular time intervals short potential pulses of gradually increasing amplitude are applied. The pulses are usually less than 5 seconds apart and 50 – 100 ms duration. The current is measured towards the end of the pulse. An output plot of sampled current against step potential is produced.

Figure 4. *Normal pulse voltammetry potential waveform.*

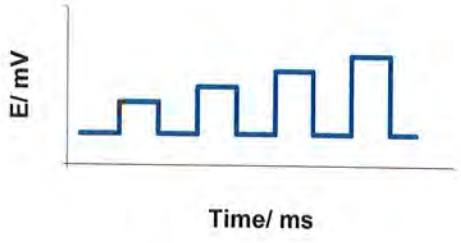

The Faradaic current is obtained from the following equation:

$$i = \frac{nFAD_O^{1/2}[O]}{\pi^{1/2}(\tau - \tau')^{1/2}} \quad (43)$$

where τ is the time between adjacent pulse rises, τ' is the time between the rise and fall of adjacent pulses (therefore $\tau - \tau'$ is the pulse duration).

Contrary to its polarographic origin NPV is usually performed using solid electrodes. Unlike the DME, where diffusion layer and electroactive surface are renewed between drops, successive pulses at the solid electrode can cause accumulation of reaction products and fouling at the surface. This causes degradation in the response compared to the polarographic measurement, but can be overcame in three ways: by using chemically reversible systems, convective renewal and diffusive renewal.

2.4.2.2 *Differential pulse voltammetry*

Differential pulse voltammetry (DPV) is similar to NPV except that E_{bl} is increased incrementally between pulses and the current is recorded twice in each pulse cycle: immediately before the pulse and immediately prior to the end of the pulse. A typical DPV potential waveform is shown in Figure 5. The pulse height, ΔE, typically in the range 10 – 100 mV, is maintained in relation to E_{bl}. An output plot of sampled current difference, $\delta i = i(\tau) - i(\tau')$, against step potential is produced.

Figure 5. *Differential pulse voltammetry potential waveform.*

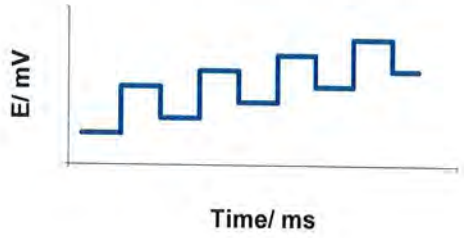

For a reversible system the peak potential, E_p, is given by equation 44, where $E_{1/2}$ is the potential at half peak height.

$$E_p = E_{1/2} \pm \frac{\Delta E}{2} \quad (44)$$

$$\delta(i)_{max} = \frac{nFAD_O^{1/2}[O]}{\pi^{1/2}(\tau-\tau')^{1/2}} \cdot \left(\frac{1-\sigma}{1+\sigma}\right) \qquad (45)$$

$$\sigma = exp\left(\frac{nF}{RT} \cdot \frac{\Delta E}{2}\right) \qquad (46)$$

The maximum current during the pulse can be calculated from equation 45, where the parameter σ accounts for the potential change during the pulse.

2.4.3 *Chronoamperometry*

In chronoamperometry (CA) a value of E_{bl} is chosen at which no Faradaic process occurs at the WE. After a short time period, usually less than 50 seconds, the potential is stepped and held at a value at which the surface concentration of electroactive species is effectively zero (eg. instantaneous reversible reaction at the WE surface). As mass transport under these conditions is solely by diffusion, the current-time curve reflects the change in concentration near the surface. As reactant is consumed near the surface the diffusion layer expands, the slope of the concentration profile decreases and the current decays with time. A typical potential waveform and macroelectrode current response are shown in Figure 6:

Figure 6. *Chronoamperometry potential and current profiles.*

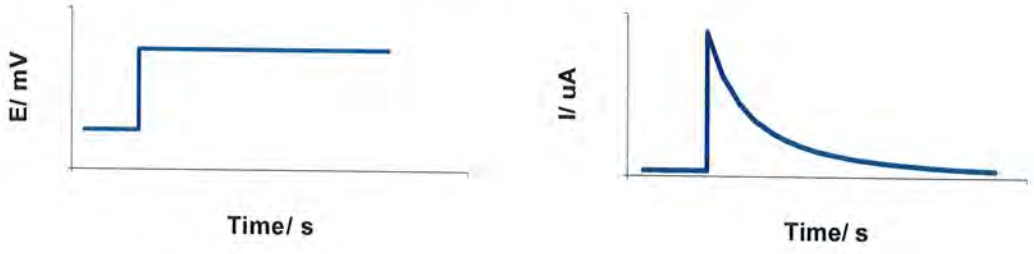

The current at a given time after the potential step can be calculated from the Cottrell equation (equation 47):[35]

$$i(t) = \frac{nFAD_O^{1/2}[O]}{\pi^{1/2}t^{1/2}} \qquad (47)$$

The Cottrell equation shows the current is proportional to $1 / t^{1/2}$ and a plot of $it^{1/2}$ against time should give a straight line. The diffusion coefficient, D_O, and electroactive

electrode area, A, can easily be obtained by rearranging the equation. It is often desirable to calculate the value of A from electrochemical rather than geometric data. This is because geometric calculations assume a smooth, uniform surface whereas in reality any surface roughness increases the effective area.

2.5 Electrochemical impedance spectroscopy (EIS)

2.5.1 *About impedance*

The electrical resistance is the ability of a circuit element to resist the passage of current. According to Ohm's law the resistance, R, is equal to the ratio of voltage, E, to current, I.

$$R = \frac{E}{I} \tag{48}$$

Ohm's law is only applicable to resistors in simple direct current (DC) circuits. In more complicated alternating current (AC) circuits several different elements (capacitors, inductors etc.) contribute to the overall circuit resistance and Ohm's law is abandoned. Impedance, Z, is the ability of a circuit to resist the passage of alternating current.

$$Z = \frac{E}{I} \tag{49}$$

In an electrochemical cell electron flow can be impeded by slow preceding reaction, slow electrode kinetics and diffusion, which can be considered analogous to the resistive circuit elements in an AC circuit.

2.5.2 *Impedance measurements*

EIS is used to study electrochemical processes at the electrode surface. A small AC voltage perturbation is applied to the electrode, the current response measured and impedance obtained as a function of AC frequency. The AC voltage perturbation, E_t, expressed as a function of time is given by:

$$E_t = E_0 \sin(\omega t) \tag{50}$$

where E_t is the potential at time t, E_0 is the amplitude of the signal and ω the radial frequency. The radial frequency, ω, is related to the Hertz frequency, f, by:

$$\omega = 2\pi f \tag{51}$$

In real systems the current response, I_t, to the AC voltage perturbation is out of phase by angle θ due to a combination of the impeding circuit elements:

$$I_t = I_0 \sin(\omega t + \theta) \tag{52}$$

The impedance as a function of frequency is therefore given by:

$$Z = \frac{E_t}{I_t} = \frac{E_0 \sin(\omega t)}{I_0 \sin(\omega t + \theta)} = |Z| \frac{\sin(\omega t)}{\sin(\omega t + \theta)} \tag{53}$$

The potential perturbation and current response can also be expressed as complex functions:

$$E_t = E_0 \sin(j\omega t) \tag{54}$$

$$I_t = I_0 \sin(j\omega t - j\theta) \tag{55}$$

Considering Euler's relationship, $exp(j\theta) = cos(\theta) + jsin(\theta)$, the impedance can be written as:

$$Z = \frac{E_0 \sin(j\omega t)}{I_0 \sin(j\omega t - j\theta)} = |Z| exp(j\theta) = |Z|(\cos\theta + j\sin\theta) = Z' + jZ'' \tag{56}$$

where Z' and Z'' are real and imaginary contributions to the impedance respectively. The modulus, $|Z|$, can be calculated from the vector combination of the Z' and Z" components. The relationship between $|Z|$, Z' and Z" is shown in Figure 7:

Figure 7. *Relationship between* $|Z|$, *Z' and Z".*

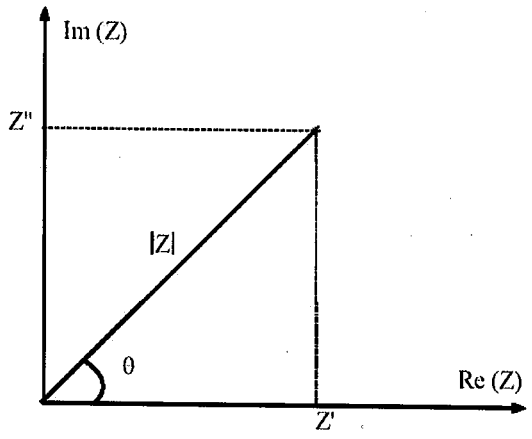

$$|Z| = \sqrt{(Z')^2 + (Z'')^2} \qquad (57)$$

$$tan\theta = \frac{Z''}{Z'} \qquad (58)$$

The data is usually displayed as a *Nyquist* (*Z"* against *Z'*) or *Bode* plot ($log|Z|$ or θ against $log\omega$).

In the Nyquist plot shown (Figure 8(a)) the frequency reaches its highest value towards the left, where the semicircle touches the *Z'* axis. At low frequencies, towards the right where the semicircle touches the *Z'* axis, the impedance is approximately a combination of the uncompensated solution resistance, R_S, and charge-transfer resistance, R_{CT}. At low frequencies the AC voltage waveform and resulting current tend towards DC behaviour, explaining the purely resistive nature of the impedance value.

The main advantage of the Nyquist plot is that it is easy to observe the effects of ohmic resistance. If data is collected at sufficiently high frequency the curve can be extrapolated downwards and the *Z'* intercept read to give a value of resistance. The shape of the curve does not change with resistance so it is easy to compare data collected under different experimental conditions. A disadvantage of this plot format is that the frequency does not appear explicitly and it is only possible to calculate the electrode capacitance if the frequency is known. As shown in Figure 8(a) the frequency at $Z''(\omega)_{max}$ can be used to calculate the resistance if R_{CT} is known.

Figure 8. *Example Nyquist plot.*

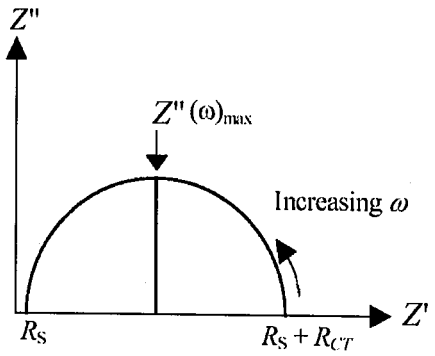

(a) Nyquist plot for a simple electrode reaction.

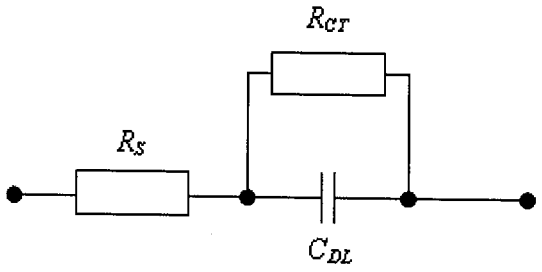

(b) Circuit equivalent of the electrode reaction. Note at low frequencies there is negligible charge-transfer across the capacitor, so the circuit is effectively a combination of R_S and R_{CT}.

The Bode plot corresponding to Figure 8(a) is shown in Figure 9. This format has several distinct advantages over the Nyquist plot. Since frequency appears on one of the axes, it is easy to understand from the plot how impedance is related to frequency. The frequency scale is logarithmic allowing a wide range of values to be plotted on the graph, but with each decade given equal weight. Similarly, since $log|Z|$ is used on the y-axis a wide range of impedance values can be compared on the same axes. This can be an advantage when the impedance is strongly dependent on frequency, as in the case of a capacitor.

Values of C_{DL}, R_S, $R_S + R_{CT}$ and θ_{max} can be obtained directly from the plot as indicated by Figure 9.

Figure 9. *Example Bode plot.*

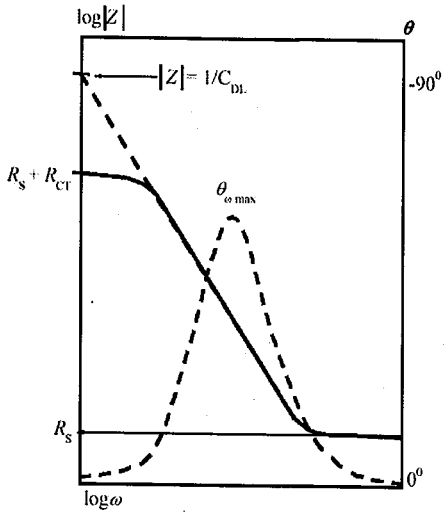

The Bode plot corresponding to the same data shown in the Nyquist plot, Figure 8(a).

2.6 Patch-clamp measurements

2.6.1 *General overview*

Hodgkin and Huxley used the voltage-clamp technique with intracellular microelectrodes to provide the first detailed description of the action potential in nerve axons.[36] The technique is now the method of choice for the study of ion channels. A pair of sharp microelectrodes, of tip diameter < 0.1 μm, are mounted either side of the substrate of interest. One electrode applies a potential to the substrate, while the other measures the resulting current across the substrate.

This work was refined by Neher and co-workers, who won a Nobel Prize for their development of a patch-clamp technique which allows the current of single transmembrane channels to be recorded.[37] Patch clamping allows the direct electrical measurement of ion channel currents while simultaneously controlling the cell's membrane potential. There are 4 main modes of patch clamping – the whole-cell, cell-attached, outside-out and inside-out configurations. These configurations differ in the physical interaction between the measuring tip and cell substrate. The whole-cell and cell-attached variants are of most relevance to our work.

2.6.2 *Whole-cell measurements*

Whole-cell measurements are obtained by gently touching the micropipette tip on the surface of the cell. Gentle suction is applied to rupture the cell membrane in the tip-contact region, so a low-resistance pathway is created between the tip and cell interior.

The cell is voltage-clamped at the potential of this contacting tip and a second electrode monitors current flow across the entire cell surface. The current measured corresponds to the average current of many simultaneously conducting channels superimposed on noise. Whole-cell measurements afford quick and simple results and analysis, so it is the configuration used most frequently.

Figure 10. *Patch clamp set-ups.*

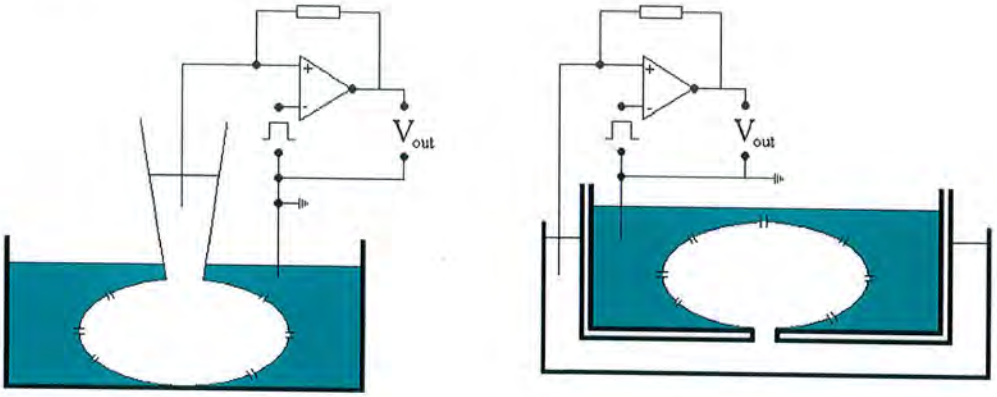

(a) Classical whole-cell configuration. *(b) Patch clamp chip and circuit.*

A disadvantage of whole-cell measurements is that the current observed is uncompensated for the ohmic drop across the tip-cytoplasm junction. Another drawback is that ions and molecules present in the cytoplasm can diffuse up through the patch clamp and 'leak' from the cell by a non-physiological process. Again, this unnatural leakage is uncompensated for in the measured current. The perforated-patch technique of Horn and Korn overcomes the membrane leakage problem by providing a membrane-intact means of recording.[38] In this adaptation the pipette-tip solution is filled with a pore-forming antibiotic like amphotericin B. Just as before, the tip is touched against the membrane surface but instead of physical disruption by suction the low-resistance pathway is created by the self-assembly of amphotericin channels in the region of the interface.

2.6.3 *Cell-attached measurements*

For cell-attached measurements the micropipette tip is gently touched on the surface of the membrane. In contrast to whole-cell measurements, the membrane is not ruptured and a high resistance interface exists between the tip and membrane surface. The

background noise signal is finely attenuated by the instrumentation and single channel currents can be resolved.[37]

Single-channel recordings in cell-attached mode have shown that many channels, in particular the voltage gated Na^+ channel, display only two conductance levels corresponding to channel closed (zero current) and channel open (constant current) states.[39,40]

2.7 Scanning electrochemical microscopy (SECM)

2.7.1 *Probe microscopy*

Probe microscopy relies on a miniature measuring probe being scanned over the surface of a target substrate in three dimensions. A computer records the probe location and the local signal collected by the probe tip. Two main attractions make the probe microscopy methods popular. Firstly, high-resolution topographical information can be retrieved. This is complimented by being able to view the substrate under ambient conditions. From an electrochemical point of view, it was found that scanning tunnelling microscopy (STM) could be used for electrolyte solution / solid interface measurements.[41] In 1990 Bard successfully combined a probe microscopy with the use of ultra microelectrodes (UMEs), marking the birth of SECM.[42] Bard's initial work focused on the interaction of the probe tip and substrate surface, investigating the so-called feedback mode.[43,44]

2.7.2 *Basic principles*

The scanning electrochemical microscope (SECM) is composed of four key components:

(a) A three electrode set-up. The working electrode is of UME dimensions (≤ 20 μm radius), which is often referred to as the tip.

(b) A precision tip positioning device, comprising three piezo-electric motors mounted at right angles to each other.

(c) A bipotentiostat capable of measuring currents on the femto ampere scale.

(d) A facility for data collection, normally in the form of a personal computer.

A schematic representation of the SECM instrument is shown in Figure 11.

Figure 11. *Representation of the SECM.*

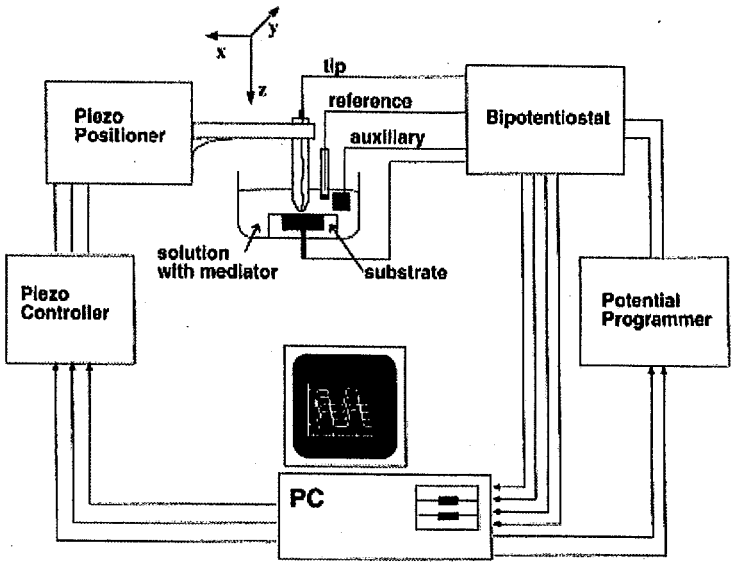

Block diagram of typical SECM apparatus. The substrate (target) may or may not be connected directly to the bipotentiostat.[45]

In common with the other potentiostatic methods current flows between the tip and CE and the tip potential is measured relative to a known reference. In bipotentiostatic mode measurements can be made with a second potential applied to the substrate.

SECM experiments fall into two broad categories:

(a) *Tip active*, in which the probe interacts with the substrate surface creating an electrochemical response.

(b) *Tip passive*, in which the probe is held stationary and monitors an externally induced electrochemical response at the fixed location on the substrate surface.

Mass transport to the tip is by diffusion and, to a much lesser extent, migration. Convection, due to mechanically forced movement of the electroactive solution towards the tip, makes only a negligible contribution due to the very slow tip movement during measurements.

There are five main modes of SECM imaging: amperometric feedback, tip generation / tip collection, penetration, potentiometric detection and ion-transfer feedback.

2.7.3 *Amperometric feedback mode*

A UME polarised at high constant potential in bulk electrolyte solution displays a steady-state current $i_{T,\infty}$. The observed current is dependent on mass transport of the electroactive species (hereafter called the '*mediator*') to the tip surface. The tip surface is usually disk shaped, and in such cases $i_{T,\infty}$ can be calculated from the equation:

$$i_{T,\infty} = 4nFDca \qquad (59)$$

where n is the stoichiometric number of electrons involved in the tip electrode process, a is the radius of the tip metal disc, F is the Faraday constant, D is the diffusion coefficient and c is the bulk concentration of the reacting species.

As the SECM tip is moved closer to the substrate surface, the magnitude of the tip current either increases or decreases. A decrease in tip current is termed a negative feedback, whereas an increase is a positive feedback.

Negative feedback is caused when the substrate surface obstructs passage of the mediator to the approaching tip surface. Mediator obstruction results in a decrease in the rate of heterogeneous electron-transfer at the tip surface. In most cases the probe tip is encircled by a glass shield, which also contributes to the negative feedback term. The shield to tip ratio, *RG*, is given by:

$$RG = \frac{R_g}{a} \qquad (60)$$

where R_g is the radius of the glass shield at the tip and a the radius of the tip metal disc. In the case of an $RG = 10$ tip the following equation can be used to quantify the shielding effect:

$$\frac{i_{T,L}}{i_{T,\infty}} = \frac{1}{0.15 + \left(\frac{1.5385}{L}\right) + 0.5exp\left(\frac{-1.14}{L}\right) + 0.0908exp\left(\frac{L-6.3}{1.017L}\right)} \qquad (61)$$

where the normalised tip-substrate distance $L = d/a$, d is the tip-substrate distance and a the radius of the tip surface.

Negative feedback is exhibited by electrically insulating substrates or those substrates where the electron-transfer at the probe tip is irreversible.

Positive feedback occurs when there is an amplification of tip current as the tip nears the substrate. This behaviour is exhibited by electrically conducting substrates or those substrates where the electron-transfer at the tip is spontaneous and reversible. The conducting substrate regenerates the mediator, causing an increase in its local concentration, and allowing it to further react at the adjacent tip. Mirkin and co-workers proved the following equation for the current ratio:[46]

$$\frac{i_{T,L}}{i_{T,\infty}} = \left(\frac{0.78377}{L}\right) + 0.3315exp\left(\frac{-1.0672}{L}\right) + 0.68 \quad (62)$$

Positive feedback can be used to monitor the tip-substrate distance of a conducting target. Again, this equation applies when $RG = 10$.

The two feedback equations (equations 61 and 62) hold true for diffusion-controlled heterogeneous reactions in the range $0.5 \geq L \leq 20$.

Two-dimensional amperometric feedback measurements (also known as '*area scans*') on the substrate are also easily performed. As the tip, with applied potential, is slowly scanned over the substrate repeated feedback profiles are obtained. The data is presented as a current map of the substrate, with regions of differing feedback contrasting in colour. When area scans are obtained in negative feedback mode, a small current indicates upward projections on the substrate surface, whereas a large current indicates downward projections.

Figure 12. *Copper minigrid area scan.*

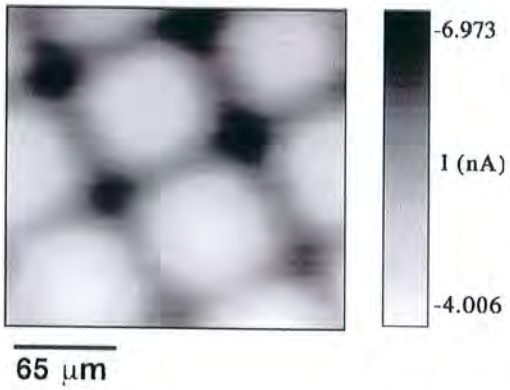

SECM area scan of a copper minigrid immersed in ruthenium hexamine solution. A 5 μm Pt tip was used at a distance of 10 μm from the target surface. Higher tip current shows as a darker image.[47]

Using an electrolyte combination of low miscibility can also have a marked effect on the detected current.[48] This effect can be similar to either positive or negative feedback. Hindered diffusion of the mediator across the electrolyte-electrolyte boundary results in a negative feedback-like result. This occurs when the species reacting at the tip has low solubility in the second electrolyte. However, a mediator may be dissolved in the second electrolyte, which regenerates the electroactive species in the first. Mediated electron-transfer between the electrolyte phases causes a positive feedback effect and causes a tip current increase.

2.7.4 *Generation / collection mode*

In some circumstances the substrate surface changes the electrolyte concentration profile in the region immediately above it. In substrate generating / tip collection (SG / TC) mode the SECM measuring tip can be used to collect information on this profile change.[49]

The probe tip can also be used to generate concentration disturbances about the target surface. In this case the target substrate, connected to the potentiostat, collects information on the profile change. This is known as tip generating / substrate collection (TG / SC) mode.

2.7.5 *One-dimensional (penetration) mode*

In penetration mode the UME probe tip is moved on the Z-axis towards and into the soft substrate surface. Penetration mode experiments have been performed on biological

tissue samples and enzyme containing gels to monitor the concentration of species at different depths from the sample surface.[50]

2.7.6 *SECM measuring tips*

The size, shape and type of measuring tip have a large bearing on the information obtained in an SECM experiment. Traditionally, SECM tips have been made by sealing a micrometer diameter gold, platinum or palladium wire or carbon fibre in the lumen of a glass capillary as shown in Figure 13. The capillary end is then heat-sealed, bevelled and polished. Bevelling ensures the glass shield enclosing the conductive fibre does not interfere with the approach of the tip to the target surface, and also prevents the diffusion path of the electroactive species from being hindered. The small diameter of the micro wires or carbon fibre makes them susceptible to damage during the heat-sealing process. For this reason, purpose-built pipette pullers are used in the fusion process.[51]

Figure 13. *Illustration of an SECM measuring tip.*

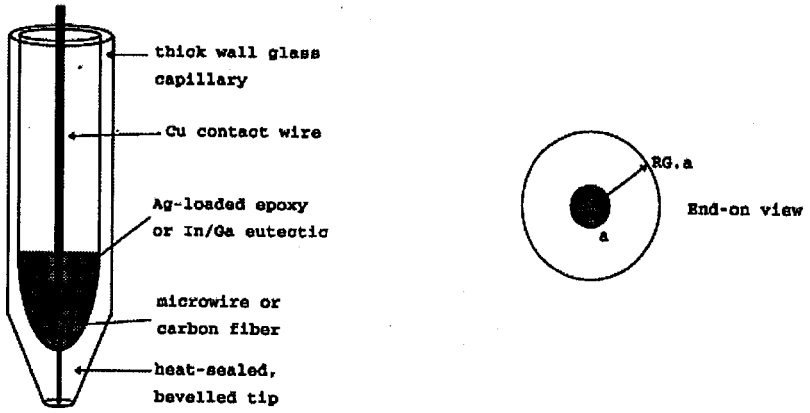

The main advantages of using a UME over a conventional macroelectrode are the high spatial resolution and fast mass transport achievable. Unlike macroelectrodes, where diffusion to the electrode surface is confined to one dimension, UMEs allow radial diffusion. In effect, this means UMEs can detect a greater current per unit concentration of analyte, hence UMEs are particularly suitable for the study of high-resistance electrolyte systems and systems where the addition of supporting electrolyte is undesirable.

There is great interest in the production of nanometre-sized tips to try and refine these two properties even more. The electrochemical etching of Pt / Ir rods in saturated $CaCl_2$

and HCl has been successfully employed in the production of nanometre scale tips.[46] More recently tips that are slightly recessed into the glass shield have been prepared in a similar fashion.[52] When the recessed tip is approached to the target surface it is possible to trap and detect individual molecules in the shield pocket.[53]

Some species are not readily oxidised or reduced at the surface of the traditional metal disc SECM tip. These species cannot be monitored amperometrically with the metal tip, so are incompatible with SECM. However, chemical modification of the probe tip can be carried out, making it suitable for the analysis of these poorly oxidised or reduced species. Horrocks successfully modified a carbon disc electrode by coating the fibres with horseradish peroxidase (HRP).[54] HRP was tethered to the carbon surface by a redox polymer chain. The modified electrode was used as a biosensor for hydrogen peroxide.

Ion-selective electrodes (ISEs) had been used as a potentiometric probe for biological systems long before the advent of SECM. An ISE tip can be used in SECM for the detection of electrochemically inactive species like NH_4^+ and alkali metal cations. These ISEs are constructed using micropipettes. An ion-selective layer is added towards the tip surface then the pipette is back filled with reference electrode filling solution. Finally the reference electrode, usually a silver wire coated with silver chloride, is suspended in the filling solution. An Ag / AgCl micropipette has proved to be a successful way of monitoring Cl^- flux.[55] These ISEs are passive sensors, which do not affect the electroactive species concentration gradient near the substrate. The potentiometric nature of the tips prevents them being of use for accurate tip-substrate distance measurements. Consequently early experiments had the frequent problem of tip crash: where the ISE measuring tip ploughed into the substrate often damaging the target surface. Second-generation probe tip ISEs overcame this problem by the incorporation of a second barrel (Figure 14), as first proposed by Wei.[56] The second barrel contains a metal microelectrode, typically gallium, which acts as an amperometric sensor in feedback mode.[57]

Figure 14. *Double barrelled SECM tip.*

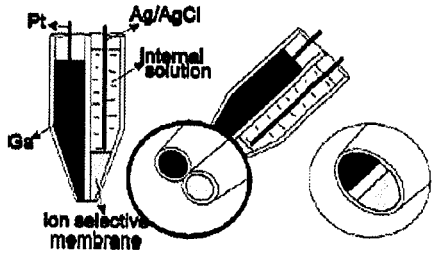

Double barrelled SECM tip. The first barrel encloses the gallium amperometric tip for distance estimation. The second barrel encloses the ion-selective membrane and internal reference.

2.8 References

1. H. L. F. von Helmholtz, *Ann. Physik*, 1853, **89**, 211
2. H. L. F. von Helmholtz, *Ann. Physik*, 1879, **7**, 337
3. G. Guoy, *Compt. Rend.*, 1910, **149**, 654
4. D. L. Chapman, *Phil. Mag.*, 1913, **25**, 475
5. O. Stern, *Z. Elektrochem.*, 1924, **30**, 508
6. D. C. Grahame, *Chem. Rev.*, 1947, **41**, 441
7. O. A. Easin and B. F. Markov, *Acta Physicochem. USSR*, 1939, **10**, 353
8. J. O'M. Bockris, M. A. Devanathan and K. Müller, *Proc. R. Soc.*, 1963, **A274**, 55
9. P. A. Cox, *The Electronic Structure and Chemistry of Solids*, Oxford University Press, Oxford, 1987
10. A. R. West, *Basic Solid State Chemistry*, John Wiley and Sons Ltd., Chichester, 1999
11. Baron Kelvin of Largs, *Philos. Mag.*, 1898, **46**, 82
12. W. A. Zisman, *Rev. Sci. Instrum.*, 1932, **3**, 367
13. A. Fick, *Phil. Mag.*, 1855, **10**, 30
14. A. Fick, *Poggendorff's Annel. Physik*, 1855, **94**, 59
15. M. von Smoluchowski, *Ann. Physik (Leipzig)*, 1906, **21**, 756
16. K. B. Oldham, *J. Electroanal. Chem.*, 1992, **337**, 91
17. M. J. Peña, M. Fleishmann and N. Garrard, *J. Electroanal. Chem.*, 1987, **220**, 31
18. A. M. Bond, M. Fleischmann and J. Robinson, *J. Electroanal. Chem.*, 1984, **168**, 299
19. R. M. Wightman, E. Strope, P.M. Plotsky and R. N. Adams, *Nature*, 1976, **262**, 145
20. R. M. Wightman, *Science*, 2006, **311**, 1570
21. M. A. Dayton, J. C. Brown, K. J. Stutts and R. M. Wightman, *Anal. Chem.*, 1980, **52**, 946
22. J. A. V. Butler, *Trans. Faraday Soc.*, 1924, **19**, 729 and 734
23. T. Erdey-Gruz and M. Volmer, *Z. Physik. Chem.*, 1930, **150A**, 203
24. A. C. Testa and W. H. Reinmuth, *Anal. Chem.*, 1961, **33**, 1320
25. J. Alden, D. Phil Thesis, University of Oxford, 1998, section 1.3.2
26. J. Heinze, *Angew. Chem. Int. Ed. Engl.*, 1984, **23**, 831
27. J. Julliard, *Pure Appl. Chem.*, 1977, **49**, 885
28. J. F. Coetzee, *Pure Appl. Chem.*, 1977, **49**, 221
29. H. Kiesele, *Anal. Chem.*, 1980, **52**, 2230
30. O. Hammerich and V. D. Parker, *Electrochim. Acta*, 1973, **18**, 5

31. H. Kiesele, *Anal. Chem.*, 1981, **53**, 1952
32. T. J. Cardwell, J. Mocak, J.H. Santos and A. M. Bond, *Analyst*, 1996, **121**, 357
33. D. D. McDonald, *Transient Techniques in Electrochemistry*, Plenum Press, New York, 1977, Chapter 2
34. A. W. Bott, *Current Separations*, 1995, **14**, 64
35. F. G. Cottrell, *Z. Physik. Chem.*, 1902, **42**, 385
36. A. L. Hodgkin and A. F. Huxley, *J. Physiol.*, 1952, **117**, 500
37. O. P. Hamill, A. Marty, E. Neher, B. Sakmann and F. J. Sigworth, *Pflügers Arch.*, 1981, **391**, 85
38. R. Horn and S. J. Korn, *Methods Enzymol.*, 1992, **207**, 149
39. H. Lerche, N. Mitrovic, V. Dubowitz and F. Lehmann-Horn, *Ann. Neurol.*, 1996, **39**, 599
40. N. Mitrovic, A. L. George, R. Heine, S. Wagner, U. Pika, U. Hartlaub, M. Zhou, H. Lerche, C. Fahlke and F. Lehmann-Horn, *J. Physiol.*, 1994, **478**, 395
41. H. Y. Liu, F. R. F. Fan, C. W. Lin and A. J. Bard, *Chem. Soc.*, 1986, **108**, 3838
42. A. J. Bard, G. Denuault, C. Lee, D. Mandler and D. O. Wipf, *Acc. Chem. Res.*, 1990, **23**, 357
43. A. J. Bard, F. R. F. Fan, D. T. Pierce, P. R. Unwin, D. O. Wipf and F. Zhou, *Science*, 1991, **254**, 68
44. A. J. Bard, F. R. F. Fan, J. Kwak and O. Lev, *Anal. Chem.*, 1989, **61**, 132
45. M. V. Mirkin and B. R. Horrocks, *Anal. Chim. Acta*, 2000, **406**, 119
46. M. V. Mirkin, F. R. F. Fan and A. J. Bard, *J. Electroanal. Chem.*, 1992, **328**, 47
47. G. Nagy and L. Nagy, *Fresenius J. Anal. Chem.*, 2000, **366**, 735
48. C. Wei, A. J. Bard and M. V. Mirkin, *J. Phys. Chem.*, 1995, **99**, 16033
49. R. D. Martin and P. R. Unwin, *Anal. Chem.*, 1998, **70**, 276
50. S. D. Kolev, G. Nagy and E. Pungor, *Anal. Chim. Acta*, 1991, **254**, 167
51. E. Neher, *Angew. Chem. Int. Ed. Engl.*, 1992, **31**, 824
52. F. R. F. Fan and A. J. Bard, *Science*, 1995, **267**, 871
53. F. R. F. Fan, J. Kwak, A. J. Bard, *J. Am. Chem. Soc.*, 1996, 118, 9669
54. B. R. Horrocks, D. Schmidtke, A. Heller and A. J. Bard, *Anal. Chem.*, 1993, **65**, 3605
55. G. Denuault, M. H. Troise-Frank and L. M. Peter, *Faraday Discussions*, 1992, **94**, 23
56. C. Wei, A. J. Bard, G. Nagy and K. Tóth, *Anal. Chem.*, 1995, **67**, 1346
57. C. Wei, A. J. Bard, I. Kapui, G. Nagy and K. Tóth, *Anal. Chem.*, 1996, **68**, 2651

Chapter 3

The Peptide-Lipid Environment

3.1 Peptide ion channels

3.1.1 *Gramicidin A*

Gramicidin A (gA) is a naturally occurring 15-residue polypeptide produced by the soil bacteria *Bacillus brevus*. It is composed of alternating D- and L- amino acids, and forms monovalent cation-selective channels in bilayer lipid membranes (BLMs). The primary structure of gA is shown in Figure 15 and Table 3.

Figure 15. *Structure of gramicidin A.*

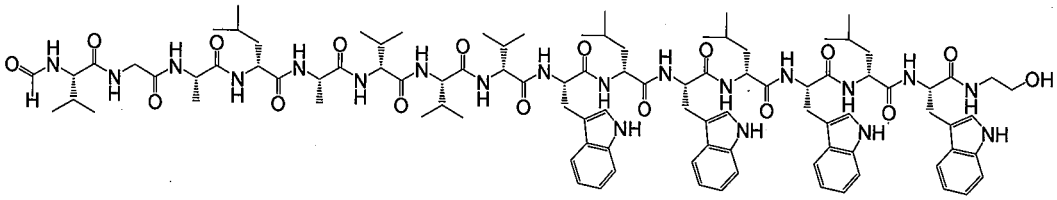

Table 3. *Amino acid sequence of the gramicidins.*

Peptide	*Sequence (*see note)*
Gramicidin A (gA)	*formyl-L-Val-Gly-L-Ala-D-Leu-L-Ala(5)-D-Val-L-Val-D-Val-L-Trp-D-Leu(10)-L-Trp-D-Leu-L-Trp-D-Leu-L-Trp(15)-ethanolamine*
Gramicidin B (gB)	*formyl-L-Val-Gly-L-Ala-D-Leu-L-Ala(5)-D-Val-L-Val-D-Val-L-Trp-D-Leu(10)-L-Phe-D-Leu-L-Trp-D-Leu-L-Trp(15)-ethanolamine*
Gramicidin C (gC)	*formyl-L-Val-Gly-L-Ala-D-Leu-L-Ala(5)-D-Val-L-Val-D-Val-L-Trp-D-Leu(10)-L-Tyr-D-Leu-L-Trp-D-Leu-L-Trp(15)-ethanolamine*

**Figures in parentheses represent the residue position within the chain.*

Bacillus brevus produces a mixture known as gramicidin D (gD) which is composed of gA (~ 80%) and two other structural variants (gramicidins B and C). The variants differ from gA at position 11, with the substitution of tryptophan for either phenylalanine (in the case of gB) or tyrosine (in the case of gC).

The gA primary structure is absent of polar and hydrophilic residues, resulting in over all hydrophobicity and low water solubility. The presence of N-terminal formyl and C-terminal ethanolamine groups further contributes to the hydrophobic nature by preventing the formation of zwitterionic forms. When dissolved in highly polar organic

solvent, such as the 1:1 dimethylsulfoxide / acetone mixture employed by Roux and co-workers, gA exists as a disordered array of monomers.[1] In less-polar organic solvents gA exists as a mixture of parallel and antiparallel entwined dimers and unstructured monomers.[2,3] The exact composition of the dimer / monomer mixture is dependent on the solvent type, temperature and peptide concentration. Four dimeric forms have been identified each of which has two interwoven monomers ~ 31 Å in length, 5.6 residues per turn held together by 28 hydrogen bonds (Figure 16). The dimers have been extensively studied using solution-state NMR[4] and circular dichroism (CD) spectroscopy.[5]

Figure 16. *Solution-state gA dimers.*[7]

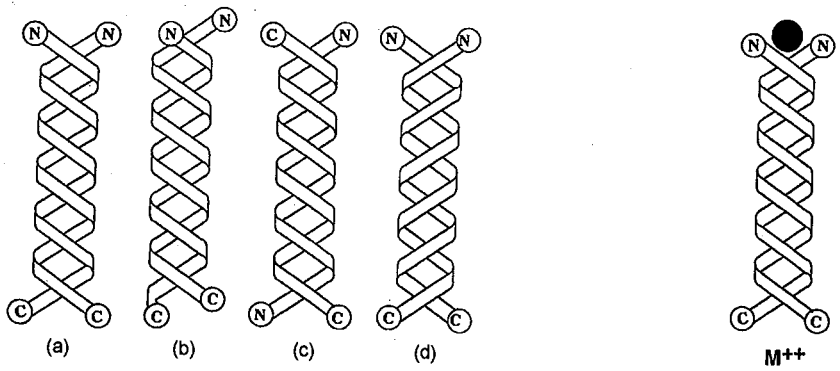

The four gA double-helical conformers found in solution.

Proposed stabilisation of conformer (a) by multivalent cation binding at the N-terminus.

CD has been used to observe conformational changes that arise in the solution-state entwined dimers with the introduction of monovalent[6] or multivalent[7] cations. The introduction of Cs^+ to a methanol solution of gA results in a large change in CD spectrum, indicative of a change in helix motif and handedness. In comparison, vesicle-bound gA shows a similar structure in the presence and absence of Cs^+. This suggests that the solution conformation is different to that in membranes. Subsequently, the change in ellipticity was used to monitor conformational change following the addition of divalent cation salts to gA in methanol solution. Spectral change was found to be dependent on cationic and anionic radii, but independent of cationic charge. The greatest change in conformation occurred when the solution was treated with CaX_2, where $X \neq F$. This has led to the postulation that Ca^{2+} binds to the N-terminal cavity, producing a net positive charge at the C-terminus, which in turn associates with X^-.

It was Urry who first considered the structure of the membrane-inserted gA channel back in the early 1970's. Urry predicted that channels were formed when the lateral diffusion of monomers in the membrane led to the formation of head-to-head (N-terminal-to-N-terminal) dimers.[8] A similar model with tail-to-tail (C-terminal-to-C-terminal) dimerisation was considered by Bradley and co-workers a few years later.[9] It was also suggested that since gA adopted entwined helical dimers in less-polar organic solvents, they might also adopt that configuration to span the hydrophobic core of the BLM. To this end Veatch proposed parallel and antiparallel double β-helices.[5]

Figure 17. *The initial proposed structures of gA channels.*[10]

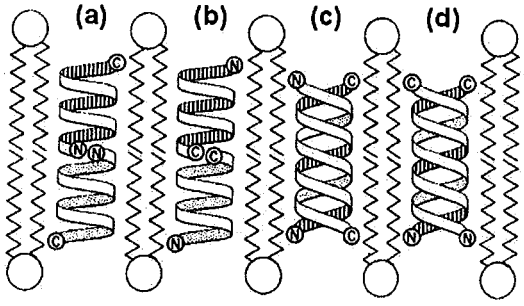

(a) N-to-N dimerisation proposed by Urry,[8] (b) C-to-C dimerisation proposed by Bradley,[9]
(c) antiparallel double β-helix proposed by Veatch,[5] (d) parallel double β-helix proposed by Veatch.[5]
(a) and (b), the helical dimers (HDs), have 6.3 residues per turn and are therefore denoted $\beta^{6.3}$-helices.

The predominant conformation of gA in phosphatidylcholine vesicles was determined using ^{13}C and ^{19}F NMR spectroscopy.[10] Specific ^{13}C and ^{19}F nuclei were incorporated in the N- and C-terminal groups, and the accessibility of these to paramagnetic probes was observed by chemical shift and relaxation time measurements. Results showed that the C-terminus was located at the vesicle surface, whereas N-terminus was buried deep within the bilayer, in agreement with Urry's N-terminal-to-N-terminal dimer described earlier.

Two distinctive gramicidin channel structural families have been identified: the Urry helical dimer (HD) structure and the Veatch double helix (DH) structure. For each of the two families, high-resolution structures have been determined by X-ray crystallography and NMR spectroscopy.[11] HD structures have been determined by solid-state NMR, in oriented lipid bilayers,[12] and solution-state NMR, in detergent micelles.[13] Solution-state NMR[14,15] and X-ray crystallography[16,17,18] have been used to determine DH structures.

The HD form is characterised by two monomeric β-helices, with 6.3 residues per turn (hence denoted $\beta^{6.3}$-helices) bound via the N-termini, forming a transmembrane dimer (Figure 18). The internal pore diameter is 3 - 4 Å and the channel length ~ 26 Å.[19] The pore of the HD form opens and closes by the association/dissociation of the two peptide chain N-termini. Six intermolecular hydrogen bonds stabilise the HD as it spans the lipid bilayer (Figure 18).[20]

Figure 18. *HD channel formation by lateral diffusion and association of gA monomers.*

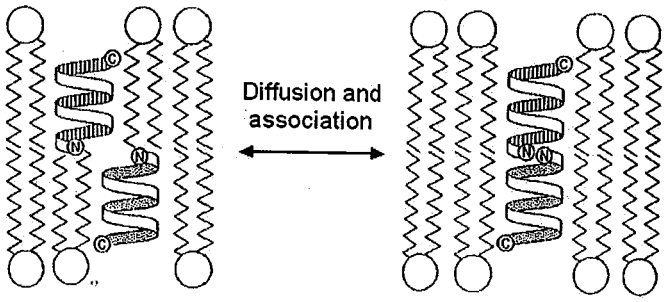

The DH structure is characterised by two hydrogen-bonded β-strands, entwined to form a double β-helix capable of spanning the lipid bilayer (Figure 19(b)). The DH structures determined so far differ in chain orientation, helix handedness, stagger and number of residues per helix turn. Recent reports indicate the HD form is the principle conducting structure.[21,22] Only in a few exceptional circumstances has conduction been observed in the DH form.[23,24,25]

In both HD and DH forms the combination of β-sheet motif and alternating residue handedness results in the hydrophobic side chains residing on the outer face of the channel and hydrophilic backbone amides and carbonyls lining the channel lumen. The combination of hydrophobic outer and hydrophilic lining results in an optimised ion-conduction pathway being partitioned within the lipid bilayer.

Figure 19. *Gramicidin HD and DH forms.*[26]

(a) HD structure determined from solid state NMR in oriented lipid bilayers.[2]

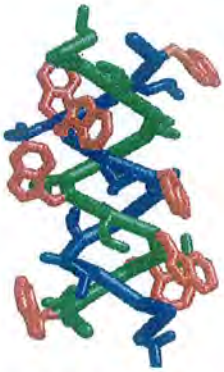

(b) DH structure of gramicidin A determined by X-ray crystallography.[6]

Gramicidin channels are permeable to monovalent cations in the following order: $H^+ >> Cs^+ > Rb^+ > K^+ > Na^+ > Li^+$.[27] This corresponds to the Eisenman sequence, indicating the dehydration energies of the cations are an important factor. The only anomaly is the high permeation of the H^+ ion, which has a relatively low dehydration energy compared to the group 1 metal cations. This can be explained in terms of a Grotthus chain-like system, whereby transfer across the channel is facilitated by protons 'hopping' along the oxygen lone pairs in a continuous row of water molecules. The H^+ conduction of single channel in glyceryl monooleate bilayer has been measured at 530 pS at 59 mV applied potential, which corresponds to 10^9 H^+ s^{-1}.[28] The current response is proportional to H^+ concentration up to ~ 4 mol dm^{-3} where a plateau occurs due to channel saturation.

The gA channel is blocked by divalent cations.[29] CD studies show no change in conformation when gA channels are treated with divalent cations. This seems to preclude an allosteric blocking mechanism, and implies a simple steric obstruction of the channel lumen. X-ray diffraction of gA in oriented multibilayer channels indicates that Ba^{2+} binds at the mouth of the channel.[30] In the X-ray study a pair symmetrical ion binding sites were found at 13.0 ± 0.2 Å from the channel mid point for Ba^{2+} and 9.6 ± 0.3 Å from the channel mid point for Tl^+. The Tl^+ result is particularly noteworthy because it indicates binding a third of the way down the channel, instead of at the channel opening. NMR studies show that Mn^{2+} affects the proton relaxation times of gA in SDS micelles and also indicate the channel-obstruction mechanism.[31]

3.1.2 *Alamethicin*

Alamethicin, isolated from the fungus *Trichoderma viride*, is a 20 residue peptide the structure of which is shown in Figure 20. For clarity the amino acid sequence is also shown in Table 4. Alamethicin is a peptide antibiotic that produces voltage-dependent conductance in BLMs. The major structure of alamethicin was elucidated by a combination of electron impact mass spectrometry (EI MS) and ^{13}C NMR.[32]

Figure 20. *Structure of alamethicin.*

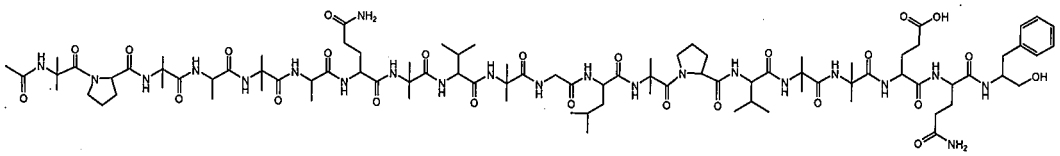

Table 4. *Amino acid sequence of the alamethicin.*

Peptide	*Sequence (*see note)*
Alamethicin	*Ac-Aib-L-Pro-Aib-L-Ala-Aib(5)-L-Ala-L-Gln-Aib-L-Val-Aib(10)-Gly-L-Leu-Aib-L-Pro-L-Val(15)-Aib-Aib-L-Gln-L-Pheol.*

**Figures in parentheses represent the residue position within the chain.*

As with gramicidin the natural product can have slight structural variation. Position 18 can either be Gln (as shown in Figure 20) or Glu. These two isomers are separable by thin-layer chromatography and have been designated R_f50 (in the case of Gln) and R_f30 (in the case of Glu). Alamethicin is a member of the peptaibol family of peptide antibiotics. Peptaibols are short, linear peptides characterised by the presence of several α-aminoisobutyric acid (Aib) residues and a C-terminal amino alcohol instead of the usual carboxylic acid. The high proportion of Aib imposes conformational constraints on the alamethicin chain, which is usually restricted to the α- or 3^{10}-helical forms.[33] Peptaibol chain lengths vary between 11 and 20 residues. Those with ≥ 16 amino acids have sufficient length to span the BLM and readily form ion channels. Molecular structures have been obtained for two common long peptaibols: the 20-residue alamethicin[34] and the 16-residue antiamoebin.[35]

In the crystalline form alamethicin exists as a trimer absent of an axial channel. The individual monomers were found to be structurally similar and an overall conformation was proposed. The proposed structure has predominantly α-helical structure from N-terminus to Pro(14), a bend just after Pro(14) and a second α-helical structure from

Val(15) to Pheol(20). Fourier-transform infrared (FT-IR) spectroscopic measurements have revealed limited 3^{10}-type hydrogen bonding along the chain length,[36] indicating an overall α- / 3^{10}-hybrid structure. Attempts to quantify the proportion of 3^{10}-helix in the monomer by CD have proved unsuccessful because the α- and 3^{10}-spectra are closely matched and difficult to resolve.[37]

The X-ray structure of alamethicin[34] indicates that the molecule is amphipathic (containing both polar and non-polar domains) in nature. The polar side chains of Gln(7) and Glu(18) occur at one side of the helix whereas the non-polar side chains of Val, Aib, Ala and Leu occur at the other. This observation, combined with the lack of axial channel and strong concentration-dependence on channel formation, have led to the proposed formation of helical bundle structures spanning the BLM.[38] When alamethicin is added to a lipid membrane it is believed to exist as an equilibrium mixture of disorganised aqueous phase monomers and semi-organised membrane-adsorbed monomers. When a positive potential is applied the N-termini of the membrane-adsorbed monomers, which represent the positive end of the peptide dipole, are repelled down through the bilayer.[39] Although the trans-membrane state is highly unstable (hydrophilic residues are buried within the bilayer) lateral diffusion and collision with other trans-membrane monomers leads to the formation of bundles. The monomers in the bundle can be considered in similar terms to the staves of a barrel hence the structure is often referred to as the '*barrel-stave*' model. The stave monomers are arranged so that the polar side chains line a central channel and non-polar side chains occupy the exterior face of the bundle in contact with the lipid membrane.

Statistical studies have shown peptaibol channels are composed of bundles of 6 – 12 parallel helical monomers.[40,41] The alamethicin pore diameter has been calculated as ranging from 3 – 10 Å for bundles of 6 – 8 monomers.[42] The peptaibols display typical channel properties such as voltage response and high flux. Unlike most other peptaibols, alamethicin demonstrates multiple conduction states, thought to be the result of monomers adding to the bundle as the membrane potential is changed.

3.1.3 *Structural features of gramicidin and the peptaibols*

Despite the peptaibols having widely different primary structures they share a variety of common structural properties:[43]

(a) *Aromatic residues are located in the region of the polar head group / non-polar tail group interface.* This is because aromatic amino acids are intermediate in polarity. In each gramicidin monomer of the HD form, the four tryptophans are located towards the C-terminal end, which, in turn, is located towards the bilayer surface.[44] Becker and co-workers have postulated that the aromatic side chain/bilayer dipole interaction gives added stability to the HD configuration.[45] In the peptaibols characterised to date there are very few aromatic amino acids. Tryptophan has been found only at peptaibol terminal ends, as has phenylalanine in all but one exception. This places aromatic residues near the bilayer surface, consistent with the residue distribution seen in gramicidin and the outer membrane proteins.

The length of the peptide chain corresponds with the thickness of the membrane hydrophobic region. The gramicidin and peptaibol models are of comparable length to the hydrophobic, hydrocarbon core of the lipid membrane. Harroun carried out X-ray diffraction experiments on gramicidin inserted into a range of different lipid membranes.[46] Lipids of a variety of fatty acid chain lengths were chosen. It was found that the lipid bilayer was able to distort slightly in the region of the channel to counteract '*hydrophobic mismatch*', and accommodate the peptide chain. These observations were in agreement with the previous theoretical calculations on hydrophobic mismatch proposed by Helfrich.[47]

(c) *Multimerisation causes channel opening and closing.* In the lipid bilayer gramicidin monomers, in the closed state, diffuse on the membrane plane until a pair of monomers marry up into an HD array, now in the open state. Channel opening in this way is equilibrium controlled: the greater the concentration of monomer, the greater the likelihood of two monomers interacting and forming the open state. For peptaibols the single helical monomer is the closed state, whereas multimeric helical bundles form the open channel.

(d) *Monomers have a high level of intramolecular hydrogen bonding, whereas multimers have a low level of intermolecular hydrogen bonding.* In gramicidin HD, the monomer is stabilised by ~ 18 intramolecular hydrogen bonds, but the dimer stabilised by only 6 intermolecular hydrogen bonds. Peptaibol monomers are stabilised by many hydrogen bonds, along the entire length of the helix. It is thought that peptaibol bundles are stabilised by only a few intermolecular hydrogen bonds per helical monomer: these

are probably towards the terminal ends of the peptaibol chains, not distributed along the chain as in the monomeric case.

(e) *The pore lumen is composed of hydrophilic amino acids.* It is necessary that the channel be lined with hydrophilic groups, in order that there be a favourable interaction with water and ions during their passage across. Gramicidin has no polar or hydrophilic side chains, so the hydrophilic channel lining is achieved by the orientation of the peptide backbone carbonyl groups. With one exception (alamethicin, which has an E residue in position 18) the peptaibols have no polar amino acid side chains, and appear to use hydrophilic side chains (glutamine, hydroxyproline) to line the lumen. In common with gramicidin, some backbone carbonyls also contribute to the lining. The gramicidin internal diameter is ~ 3 - 4 Å, imposing a high level of selectivity on the channel. K^+ ions can only cross the gramicidin channel in single file. The pore diameters of the large peptaibol bundles are far greater than that of the gramicidin dimers. This supports the observation that the peptaibol channels are far less selective about which ions can pass through.

3.2 Lipid membranes

3.2.1 *Preparation of lipid membranes*

The natural lipid membrane is a complex fluid mosaic of lipids and proteins.[48] The high structural complexity means it is difficult to study ion transport across complete, naturally occurring membranes. As membrane ion transport is an area of great interest synthetic, simplified membrane models have been developed. These synthetic models fall into three main categories: the black lipid membranes, vesicles and supported lipid membranes.

3.2.1.1 *Black lipid membranes*

Robert Hooke noticed the first black lipid membranes in 1672. Hooke was observing soap bubbles under a primative microscope and happened to note the following observations:[49]

"there appear several (black) holes, which by degrees increase and grow bigger, and several of them break into one another until at length they become very conspicuous and big.... It is pretty hard to imagine, what curious net or invisible body it is, that should keep the form of the bubble...."

Hooke had realised the potential advantages of having such a large bubble surface area formed by such a small amount of material. The BLM can be formed with a surface area of several millimetres and are a good, simplified model for characterising the physio-chemical properties of lipid membranes. One disadvantage the BLM has over supported membranes is sensitivity to changes in osmotic pressure and surface tension: any sudden changes in these cause immediate rupture and failure of the model. The sensitivity can be overcome by supporting the BLM on a solid substrate. BLMs can be prepared in two main ways: the first method involves constructing a membrane by dissolving lipid in decane. In contrast solvent-free membranes are made by dispersing lipid in a buffered aqueous solution contained in the upper compartment of a two-compartment cell, with the compartments separated by a narrow aperture.[50] Slowly draining the aqueous lipid contents from the upper compartment to the lower compartment, results in monolayer film formation over the aperture. Syringing buffer into the lower compartment raises the level of the lipid solution back through the aperture, resulting in a second monolayer being formed tail to tail with the first.

3.2.1.2 *Vesicles*

The most common method of producing large unilamellar vesicles is by rapid and repeated extrusion of multilamellar vesicles through polycarbonate membranes, as described by Hope and co-workers.[51] The resulting vesicles are commonly referred to as LUMETs (large multilammelar vesicles produced by extrusion techniques).

Hope's initial work employed phosphatidylcholine (PC), phosphatidylethanolamine (PE) and phosphatidylserine (PS) isolated from both egg albumin and soya bean. The lipids were dried and dissolved in aqueous buffer with vortexing. The buffer solution, now containing self-assembled multilamellar vesicles, was then injected into the first of two chambers separated by two stacked polycarbonate membrane filters of 100 nm pore size. The aqueous lipid was then forced through the polycarbonate filter into the second chamber. This was achieved by applying cylinder nitrogen at a pressure of 100 – 500 psi to the now sealed first chamber. Lipid solution collected in chamber two was re-extruded into chamber one and the process repeated ten times. A freeze-thaw procedure, with liquid nitrogen as the cryogen, was then applied to the lipid solution. After several freeze-thaw cycles the thawed solution was sized again through fresh polycarbonate filters.

The freeze-thaw procedure used in the preparation is thought to lead to an equilibration between the interior core of the vesicle and the exterior bulk aqueous phase. This equilibration process gives rise to an increased entrapment yield[52,53,54] and to the fragmentation of large vesicles into smaller ones.[55]

3.2.1.3 *Supported membranes*

Bacteriorhodopsin functions as a light-driven proton pump, and is the sole protein found in the purple membranes of Halobacteria.[56] Early experiments on BLMs treated with bacteriorhodopsin were limited due to membrane size and instability.[57,58] Soya bean phospholipid was introduced to a Millipore filter by simply immersing the filter in a solution of lipid in hexadecane (150 mg/ml).

Setaka and co-workers were first to report the construction of a lipid bilayer supported on a stretched cellulose sheet.[59] A cellulose sheet was laid flat in the base of a shallow trough and then covered with water. Drops of EPC cholesterol were added to the surface, which dispersed to form a lipid monolayer at the water-air interface. The stretched sheet was then raised up through the monolayer, which then assembled on the damp cellulose. Two of these cellulose-supported monolayers were combined, tail to tail, to give an overall lipid bilayer.

Lipid monolayers have been prepared on a quartz surface.[60] A quartz slide was placed in the base of a shallow trough, which was filled with buffered aqueous tris-acetic acid solution. A monolayer of 1-palmitoyl-2-oleoyl-*sn*-glycero-3-phosphocholine was formed on the aqueous surface and transferred to the quartz, as the slide was gently lifted from the base of the trough. Unilamellar vesicles prepared by the extrusion and freeze-thaw method were injected onto the quartz supported monolayer surface. Total internal reflection fluorescence microscopy was used to observe the monolayer, and it was found the vesicles fused with it to form a bilayer.

The brush technique is a simple method of preparing BLMs on polycarbonate or cellulose membranes.[61,62] The solvent was removed *in vacuo* from an EPC in chloroform solution. The dry lipid residue was then suspended, with vortexing, in buffered aqueous solution. A thin lipid film was then painted onto a flattened and

stretched polycarbonate membrane using a soft-bristled brush. The self-assembly of a lipid bilayer could be observed using an environmental scanning electron microscope.

3.3 NAD(P)$^+$ and NAD(P)H

3.3.1 *Occurrence and role in nature*

Nicotinamide adenine dinucleotide (NAD) and nicotinamide adenine dinucleotide phosphate (NADP) are pyridine-based nucleotides found in all living systems.[63] NADP differs structurally from NAD in that it has a phosphate group at the 2' position of the adenine ribose (Figure 21).

Figure 21. *Structure of NAD$^+$/NADP$^+$ (oxidised nicotinamide sub-unit).*

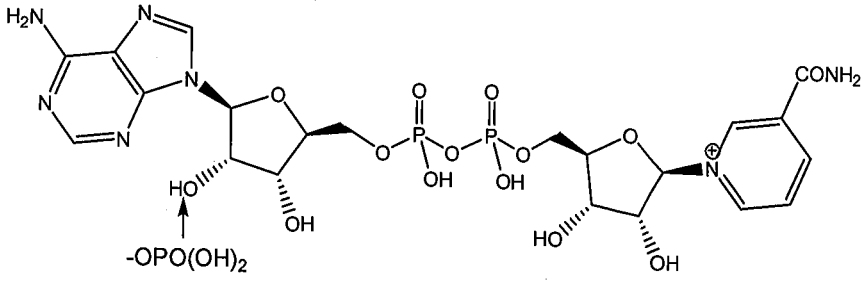

NADH/NADPH (reduced nicotinamide sub-unit).

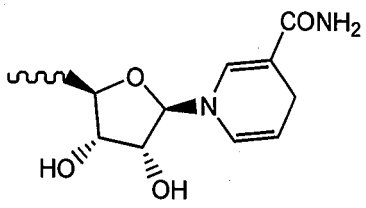

These nucleotides act as coenzymes for the reaction of more than 400 types of oxidoreductase. The role of the coenzyme in the reaction is to act as a reversible donor/acceptor of a hydride ion equivalent from the substrate. This characteristic makes NAD/NADP an essential component in biological electron transfer processes. The structure of NAD$^+$ (the oxidised form of NAD) in solution has been determined by NMR,[64,65] circular dichroism[66] and fluorescence spectroscopy.[67] The general consensus is that NAD$^+$ in solution exists as a mixture of folded and unfolded forms. The folded form has both aromatic rings in close proximity. It has been proposed that ordered parallel stacking of the rings occurs, with an inter-ring distance of less than 0.39 nm.[68,69] Conversely, a less rigid model with an inter-ring distance of 0.45 nm and imperfect stacking has been proposed.[70] The enzyme bound NAD$^+$ nucleotide adopts an unfolded

and extended configuration.[71] Conversion of the oxidised ($NAD(P)^+$) to reduced (NAD(P)H) form is brought about by the transfer of a proton and two electrons: a net hydride transfer at the nicotinamide C-4 position. Hydride transfer between the nucleotide and oxidoreductase is stereospecific. Depending on the particular circumstance either the *S*- or *R*- hydrogen of the reduced dihydronicotinamide is transferred to the substrate, or the *S*- or *R*- hydrogen of the substrate is transferred to the oxidised pyridinium ring (Figure 22).

Figure 22. *Stereospecific oxidation and reduction of NAD(P)H/NAD(P)$^+$.*

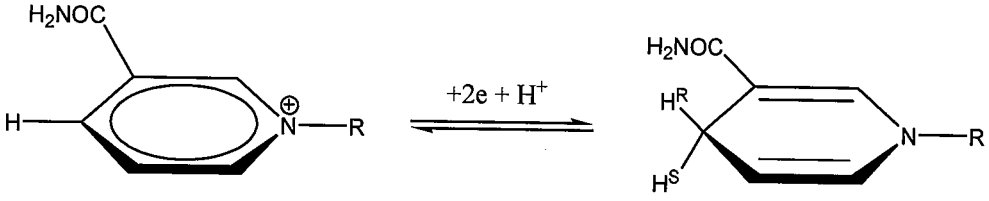

The use of deuterated forms of the coenzymes enabled elucidation of the stereospecific hydride transfer mechanism.[72] For reactions involving NAD(P)-dependent dehydrogenases, the following general equation applies:

$$Substrate + NAD(P)^+ \rightarrow Product + NAD(P)H + H^+ \qquad (63)$$

In the mitochondrial process of oxidative phosphorylation[73] electrons are transferred from NADH to O_2 via a step-wise transfer between enzymes. The resulting O^{2-} combines with $2H^+$ to yield a molecule of water:

$$NADH + H^+ + \tfrac{1}{2}O_2 \rightarrow NAD^+ + H_2O \qquad (64)$$

Oxidative phosphorylation also yields three moles of ATP for every mole of NADH oxidised.

3.3.2 *Electrochemical oxidation*

The electrochemical oxidation of NADH has been extensively studied using a wide range of electrode materials including glassy carbon (GC), carbon fibre, platinum and gold. The electrode material has a significant affect on the over-potential, demonstrated by the observation of oxidation peaks at ~ 0.474, ~ 0.775 and 1.0 V for carbon, platinum and gold electrodes, respectively.[76]

The oxidation process results in fouling of the electrode surface. Careful pre-treatment is needed to obtain reproducible results between runs. Samec and Elvin performed a thorough investigation of the oxidation of NADH at GC, platinum and gold electrodes.[77] The CVs obtained from the different electrode materials were compared in order to determine the mode and extent of adsorption. The different electrodes were immersed in buffered NADH solution at open circuit potential before being thoroughly rinsed. Subsequent CV experiments with the treated electrodes in blank buffer solution showed residual NADH oxidation peaks. It was also concluded that NADH was strongly adsorbed at platinum and gold electrodes, whereas NAD^+ was strongly adsorbed at GC. In the case of NADH adsorption at platinum and gold there is an unspecified second oxidation product that poisons the electrode.

The NADH oxidation mechanism has been extensively studied. One of the early investigations, that of Blaedel and Haas, used CV to investigate the oxidation properties of several NADH analogues.[78] In acetonitrile two oxidation peaks were observed in the absence of base, demonstrating stepwise oxidation of the model compounds. In aqueous solution only a single oxidation peak is evident, even at relatively fast scan rates, and no re-reduction occurs on the reverse sweep.[79] This combination of evidence suggests the presence of two electron-transfers and an irreversible chemical step in the reaction mechanism. Accordingly an ECE oxidation mechanism has been proposed:[78,80]

$$\begin{aligned} NADH &\xrightarrow{-e^-} NADH^{\bullet+} \\ NADH^{\bullet+} &\xrightarrow{-H^+} NAD^{\bullet} \\ NAD^{\bullet} &\overset{-e^-}{\rightleftharpoons} NAD^+ \end{aligned} \qquad (65)$$

The experiments of Blankespoor and Miller confirmed that NAD^+ is an inhibitor for the oxidation process and established the k_{H+} rate constant in the region of 10^6 s^{-1}.[81] This value was corroborated by Matsue and co-workers who determined a more precise figure of 6×10^6 s^{-1} for the proton elimination step.[82] It has been suggested that C-H bond cleavage of the proton elimination step is mediated by surface bound oxygen species, as depicted in Figure 23.[76,77]

Figure 23. *Electrode surface species as redox mediators (adapted from reference 83).*

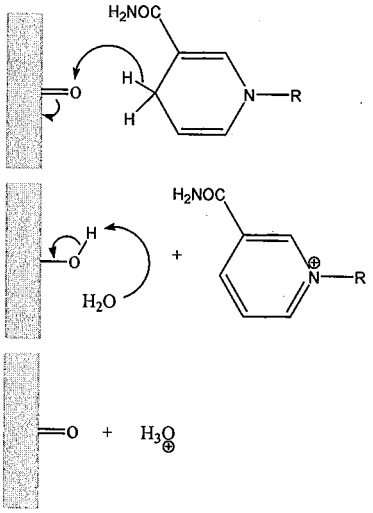

(a) Oxidation of NADH including movement of H from C^4 of the nicotinamide ring to a proton acceptor.

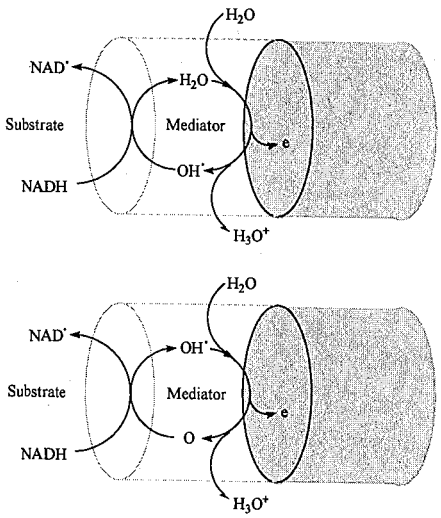

(b) Proposed surface oxygen redox systems as mediators in NADH oxidation.

3.3.3 *Electrochemical reduction*

The reduction of NAD^+ has been observed in the polarography experiments of Burnett and Underwood.[84] Two one-electron reduction peaks were observed at half-wave potentials $E_{1/2}$ = *-1.12 V* and $E_{1/2}$ = *-1.72 V* in pH 9 buffered solution. Alkaline pH was chosen to minimise hydrolysis of the nucleotide and tetraalkylammonium salts were added to suppress adsorption of NAD^+ at the electrode surface.

One suggestion for the first cathodic process is that NAD^+ undergoes a rapid and reversible one-electron reduction to form an NAD radical. The radical undergoes dimerisation and then proton mediated disproportionation (DISP1) to give NAD^+ and NADH.

$$NAD^+ + e^- \rightleftharpoons NAD^\cdot \qquad (66)$$
$$2NAD^\cdot \longrightarrow (NAD)_2$$
$$(NAD)_2 + H^+ \longrightarrow NAD^+ + NADH$$

The electron-transfer responsible for the second peak has been the subject of much speculation. Again, this electron-transfer process can only be studied at alkaline pH to prevent hydrolysis of the co-enzyme. The variation of E with pH was observed as ~ 20 mV/pH unit, which is much lower than the analogous expected single-electron variation

of 59 mV/decade. The difference in the observed (~ 20 mV/pH) and expected (59 mV/decade) has led to the suggestion that H_3O^+ is not the only proton source participating in this process. It is believed a second proton donor, HX, interacts with the NAD radical.

$$NAD^{\cdot} + HX \rightleftharpoons [NAD^{\cdot}\text{-}H\text{-}X^-] \qquad (67)$$
$$[NAD^{\cdot}\text{-}H\text{-}X^-] \xrightarrow{+e^-} [NADH\text{-}X^-]$$
$$[NADH\text{-}X^-] \xrightarrow{-X^-} NADH$$

3.4 References

1. B. Roux, R. Bruschweiler and R. R. Ernst, *Eur. J. Biochem.*, 1990, **194**, 57
2. W. R. Veatch and E. R. Blout, *Biochemistry*, 1974, **13**, 5257
3. D. A. Langes, *Science*, 1988, **241**, 188
4. V. F. Bystrov and A. S. Arseniev, *Tetrahedron*, 1988, **44**, 925
5. W. R. Veatch, E. T. Fossel and E. R. Blout, *Biochemistry*, 1974, **13**, 5249
6. B. A. Wallace, *Biophys. J.*, 1984, **45**, 114
7. D. A. Doyle and B. A. Wallace, *Biophys. J.*, 1998, **75**, 635
8. D. W. Urry, *Proc. Natl. Acad. Sci. USA*, 1971, **68**, 672
9. R. J. Bradley, D. W. Urry, K. Okamoto and R. Rapaka, *Science*, 1978, **200**, 435
10. S. Weinstein, B. A. Wallace, E. R. Blout, J. S. Morrow and W. Veatch, *Proc. Natl. Acad. Sci. USA*, 1979, **76**, 4230
11. B. A. Wallace, *J. Struct. Biol.*, 1998, **121**, 123
12. R. R. Ketcham, K. -C. Lee, S. Huo and T. A. Cross, *J. Biomol. NMR*, 1996, **8**, 1
13. A. S. Arseniev, I. Barsukov, V. F. Bystrov, A. L. Lomize and Y. A. Ovchinnikov, *FEBS Lett.*, 1985, **186**, 168
14. V. F. Bystrov and A. S. Arseniev, *Tetrahedron*, 1988, **44**, 925
15. S. M. Pascal and T. A. Cross, *J. Mol. Biol.*, 1992, **26**, 1101
16. B. A. Wallace and K. Ravikumar, *Science*, 1988, **241**, 182
17. D. A. Langs, *Science*, 1988, **241**, 188
18. B. M. Burkhart, R. M. Gassman, D. A. Langs, W. A. Pangborn and W. L. Duax, *Biophys. J.*, 1998, **75**, 2135
19. O. S. Smart, J. M. Goodfellow and B. A. Wallace, *Biophys. J.*, 1993, **65**, 2455
20. A. M. O'Connell, R. E. Koeppe and O. S. Andersen, *Science*, 1990, **250**, 1256
21. O. S. Anderson, H. -J. Apell, E. Bamberg, D. D. Busath, R. E. Koeppe, F. J. Sigworth, G. Szabo, D. W. Urry and A. Woolley, *Nature Struct. Biol.*, 1999, **6**, 609
22. T. A. Cross, A. Arseniev, B. A. Cornell, J. H. Davis, J. A. Killian, R. E. Koeppe, L. K. Nicholson, F. Separovic and B. A. Wallace, *Nature Struct. Biol.*, 1999, **6**, 610
23. S. V. Sychev, L. Barsukov, V. Y. Ivanov, *Eur. Biophys. J.*, 1993, **22**, 279
24. N. Mobashery, C. Nielson and O. S. Anderson, *FEBS Lett.*, 1997, **412**, 15
25. T. P. Galbraith and B. A. Wallace, *Faraday Discussions*, 1998, **111**, 159
26. B. A. Wallace, *BioEssays*, 2000, **22**, 227
27. V. B. Myers and D. A. Haydon, *Biochim. Biophys. Acta (Biomembranes)*, 1972, **274**, 313
28. M. Akeson and D. W. Deamer, *Biophys. J.*, 1991, **60**, 101
29. E. Bamberg and P. Läuger, *J. Membr. Biol.*, 1977, **35**, 351

30. K. He, H. W. Huang and Y. Wu, *Biophys. J.*, 1991, **59**, 318a
31. A. P. Golovanov, I. L. Barsukov, A. S. Arseniev, V. F. Bystrov, S. V. Sukhanov and L. I. Barsukov, *Biopolymers*, 1991, **31**, 425
32. R. C. Pandey, J. C. Cook, Jr. and K. L. Rhinehart, Jr., *J. Am. Chem. Soc.*, 1977, **99**, 8469
33. C. Toniolo and E. Benedetti, *Trends Biochem. Sci.*, 1991, **16**, 350
34. R. O. Fox and F. M. Richards, *Nature*, 1982, **300**, 325
35. C. F. Snook, G. A. Woolley, G. Oliva, V. Pattabhi, S. P. Wood, T. L. Blundell and B. A. Wallace, *Structure*, 1998, **6**, 783
36. P. I. Haris and D. Chapman, *Biochim. Biophys. Acta*, 1988, **943**, 375
37. M. Cascio and B. A. Wallace, *Proteins: Struct. Funct. Genet.*, 1988, **4**, 89
38. G. Baumann and P. Mueller, *J. Supramol. Struct.*, 1974, **2**, 538
39. H. Duclohier and H. Wróblewski, *J. Membr. Biol.*, 2001, **184**, 1
40. G. Boheim, *J. Membr. Biol.*, 1974, **19**, 277
41. H. Duclohier, C. F. Snook and B. A. Wallace, *Biochim. Biophys. Acta (Biomembranes)*, 1998, **1415**, 255
42. O. S. Smart, J. Breed, G. R. Smith and M. S. P. Sansom, *Biophys. J.*, 1997, **72**, 1109
43. G. A. Wallace, *BioEssays*, 2000, **22**, 227
44. W. Hu, K. C. Lee and T. A. Cross, *Biochemistry*, 1993, **32**, 7035
45. M. D. Becker, D. V. Greathouse, R. E. Koeppe and O. S. Andersen, *Biochemistry*, 1991, **30**, 8830
46. T. A. Harroun, W. T. Heller, M. T. Weiss, L. Yang and H. W. Huang, *Biophys. J.*, 1999, **76**, 937
47. P. Helfrich and E. Jacobson, *Biophys. J.*, 1990, **57**, 1075
48. S. J. Singer and G. L. Nicholson, *Science*, 1972, **175**, 720
49. H. T. Tien and A. L. Ottova, *J. Membr. Sci.*, 2001, **189**, 83
50. A. Weise, M. Munstermann and T. Gutsmann, *J. Membr. Biol.*, 1998, **162**, 127
51. M. J. Hope, M. B. Bally, G. Webb and P. R. Cullis, *Biochim. Biophys. Acta*, 1985, **812**, 55
52. U. Pick, *Arch. Biochem. Biophys.*, 1981, **212**, 186
53. K. Ansai, M. Yoshida and Y. Karino, *Biochim. Biophys. Acta*, 1990, **1021**, 21
54. C. J. Chapman, W. L. Erdahl, R. W. Taylor and D. R. Pfeiffer, *Chem. Phys. Lipids*, 1990, **55**, 73
55. R. C. McDonald, F. D. Jones and R. Qiu, *Biochim. Biophys. Acta*, 1994, **1191**, 362
56. D. Oesterhelt and W. Stoeckenius, *Nature New Biol.*, 1971, **233**, 149
57. L. A. Drachev, A. D. Kaulen, S. A. Ostroumov and V. P. Skulachev, *FEBS Lett.*, 1974, 39, 43
58. L. A. Drachev, V. N. Frolov, A. D. Kaulen, E. A. Liberman, S. A. Ostroumov, V. G. Plakunova, A. Y. Semenov and V. P. Skulachev, *J. Biol. Chem.*, 1976, **251**, 7059
59. M. Setaka, M. Yano, T. Kwan and H. Shimizu, *J. Biochem.*, 1979, **86**, 355
60. E. Kalb, S. Frey and L. K. Tamm, *Biochim. Biophys. Acta*, 1992, **1103**, 307
61. S. Amemiya and A. J. Bard, *Anal. Chem.*, 2000, **72**, 4940
62. W. Hanke and W. Schlue, *Planar Lipid Bilayers: Methods and Applications*, Academia Press, London, New York, 1993
63. H. B. White III, *Evolution of Coenzymes and the Origin of Pyridine Nucleotides*, Academic Press, New York, 1982.
64. A. P. Zens, T. J. Williams, J. C. Wisowaty, R. R. Fisher, R. B. Dunlap, T. A. Bryson and P. D. Ellis, *J. Am. Chem. Soc.*, 1975, **97**, 2850

65. R. M. Riddle, T. J. Williams, T. A. Bryson, R. B. Dunlap, R. R. Fisher and P. D. Ellis *J. Am. Chem. Soc.*, 1976, **98**, 4286
66. D. W. Miles and D. W. Urry, *J. Biol. Chem.*, 1968, **243**, 4181
67. S. F. Velick, *J. Biol. Chem.*, 1958, **233**, 1455
68. R. H. Sarma, V. Ross and N. O. Kaplan, *Biochemistry*, 1968, **7**, 3052
69. G. McDonald, B. Brown, D. Hollis and C. Walter, *Biochemistry*, 1972, **11**, 1920
70. A. P. Zens, T. A. Bryson, R. B. Dunlap, R. R. Fisher and P. D. Ellis, *J. Am. Chem. Soc.*, 1976, **98**, 7559
71. C. E. Bell, T. O. Yates and D. Eisenberg, *Protein Sci.*, 1997, **6**, 2084
72. F. A. Loewus, F. H. Westheimer and B. Vennesland, *J. Am. Chem. Soc.*, 1953, **75**, 5018
73. C. K. Mathews and K. E. van Holde, *Biochemistry (2nd edition)*, Chapter 15, Benjamin Cummins, Menlo Park CA, 1996
74. P. J. Elving, C. O. Schmakel and K. S. V. Santhanam, *Crit. Rev. Anal. Chem.*, 1976, **6**, 1
75. W. J. Blaedel and R. A. Jenkins, *Anal. Chem.*, 1974, **47**, 1337
76. P. J. Elving, W. T. Bresnahan, J. Moiroux and Z. Samec, *Bioelectrochem. Bioenerg.*, 1982, **9**, 365
77. Z. Samec and P. J. Elving, *J. Electroanal. Chem.*, 1983, **144**, 217
78. W. J. Blaedel and R. G. Haas, *Anal. Chem.*, 1970, **42**, 918
79. R. D. Braun, K. S. V. Santhanam and P. J. Elving, *J. Am. Chem. Soc.*, 1975, **97**, 2591
80. J. Ludvig and J. Volke, *Anal. Chim. Acta*, 1988, **209**, 69
81. R. L. Blankespoor and L. L. Miller, *J. Electroanal. Chem.*, 1984, **171**, 231
82. T. Matsue, M. Suda, I. Uchida, T. Kato, U. Akiba and T. Osa, *J. Electroanal. Chem.*, 1987, **234**, 163
83. A. J. Bard, M. Stratmann and G. S. Wilson (eds), *Encyclopedia of Electrochemistry, Volume 9: Bioelectrochemistry*, Wiley-VCH, Weinheim, 2002
84. J. N. Burnett and A. L. Underwood, *Biochemistry*, 1965, **4**, 2060

Chapter 4

Synthesis of a Novel Peptide Redox Switch

4.1 Introduction

Gramicidin A (gA) is a naturally occurring 15-residue peptide antibiotic. The gA monomer is comprised of alternating D- and L-amino acids and has an N-terminus formyl group and C-terminus ethanolamine group.[1] Cation selective channels are formed in the bilayer lipid membrane (BLM) by head-to-head (N-terminus-to-N-terminus) dimerisation of gA monomers. The peptide monomers adopt a $\beta^{6.3}$ right-handed helical conformation. Dimerisation occurs due to the lateral diffusion and association of the monomers within opposite leafs of the BLM.

The head-to-head structure is supported by the observation that chemical modification of the N-terminus results in reduced channel formation by the modified monomers. This effect has been noticed in a wide range of N-terminal variants, including the desformyl,[2] acetyl[3] and pyromellityl[4] forms. Conversely, chemical modification of the C-terminus has significantly less effect on channel formation supporting the idea that these termini are located at the periphery of the dimer.[5] The CD spectra of gA modified with either C-terminal acetyl or ethylenediamine show no significant difference to the unmodified form, indicating C-terminus modification has no influence on the peptide secondary structure.

Previous studies have demonstrated that modification of the C-terminus ethanolamine with carbamate groups produces channels with modified conductance properties. In particular single molecules of gramicidin A-ethylenediamine (gE), in which the terminal amino group is positively charged under physiological conditions, showed multiple conductance levels when studied with patch clamp techniques.[6,7] In the open form gE displayed a maximum conductance that was approximately half that of gA, with additional conductance levels that were ~ 90%, ~ 50% and ~ 40% of this maximal value (Figure 24). These conductance levels were attributed to *cis / trans* isomerism of the carbamate group, with the positive ammonium group obstructing the channel entrance and/or exit in the *cis* isomer, but lying away from the channel axis in the *trans* form (Figure 25).

Figure 24. *Single channel currents of gE in various salt solutions (from reference 7).*

Single channel currents for gE in various salt solutions at 150 mV applied potential. Solutions are 1 M XCl, 5 mM N,N-bis(2-hydroxyethyl)-2-aminoethanesulfonic acid (pH 6.3), except HCl, where the concentration used was 0.1 M with no added buffer. Note the four distinct conductance states in each case.

Figure 25. *C-terminus functionalised gA channel cis/trans isomers (from reference 7).*

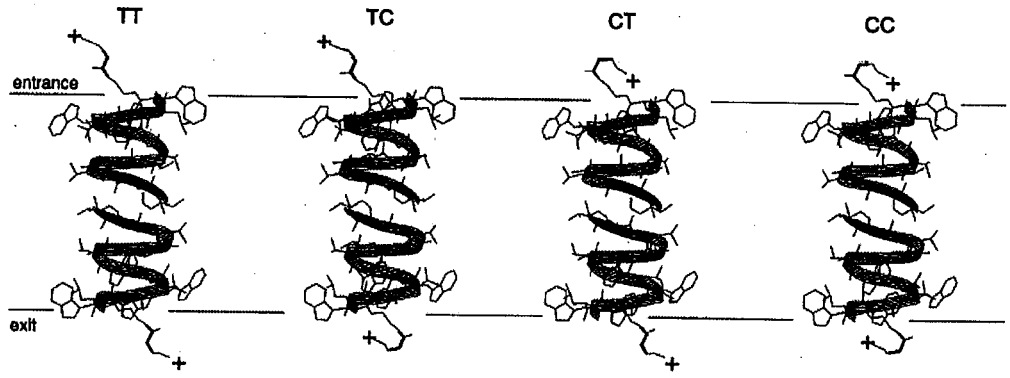

The four possible *cis / trans* combinations were then responsible for the four observed conductance levels. It was additionally observed in control experiments, that the positively charged group was essential for the production on this effect. The obstruction of the gE *cis* isomer channel by the pendant ammonium group is an example of the *ball and chain* model of channel inactivation proposed by Armstrong and Benzanilla.[8] In this model a change in potential causes one part of the molecule to activate which results in depolarisation and opening of the channel. Elsewhere in the same molecule inactivation occurs when a different part, a pendant group (the '*ball*') which is attached by a flexible linkage (the '*chain*'), moves to occlude the channel opening. The *ball* is positively charged and depolarisation confers a negative charge on the binding site

allowing for electrostatic interaction. Molecular modelling has revealed that the gE ammonium pendant is free to move within the limits of its tether.

It was considered that the nicotinamide derivative gram-2-(nicotinamidyl)ethyl carbamate (gAN) was a potentially interesting target, as in the oxidised form the molecule would possess a positive charge in the same location as gE and should therefore display similar conductance properties. In the reduced form however, this charge would be removed and the channel should conduct, providing a means of producing redox-controlled channel activity. In this chapter we detail the synthesis, purification and characterisation of the gAN potential-dependent redox switch.

Figure 26. *Structure of gAN.*

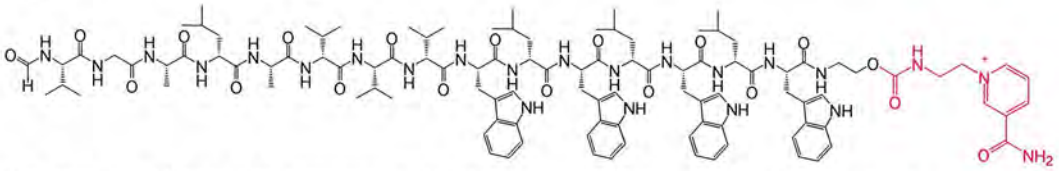

The structure of gAN. For convenience the black segment of the molecule is abbreviated as 'Gram' in future schemes.

4.2 Experimental procedure

NMR Data:	*Aromatic protons are labelled according to the ring atom they are bonded to. The highest priority ring atom is designated as atom 1: the next atom in a clockwise direction is designated atom 2 and so on.*

4.2.1 *Synthesis of gram-ethylenediamine (gE)*

Gramicidin D (340 mg, 0.18 mmol) was dissolved in dry THF (1.5 ml) and strirred under nitrogen at 0 °C. Triethylamine (0.14 ml, 1.9 mmol) was added dropwise to the stirred solution. 4-nitrophenylchloroformate (370 mg, 1.8 mmol) was dissolved in dry THF (1 ml) with stirring. The chloroformate solution was added dropwise to the stirred gramicidin solution by cannulation. The resulting pale yellow solution was stirred under nitrogen at 0 °C for 1 hour.

The reaction mixture was added dropwise to a mixture of ethylenediamine (0.73 ml, 10.9 mmol) in DMF (1 ml) and stirred under nitrogen at room temperature for 1 hour. Excess THF was removed from the reaction mixture *in vacuo*. Addition of ice-cold high

purity water (10 ml) to the residue resulted in the precipitation of the product as a pale yellow solid. The precipitate mixture was centrifuged at 3000 rpm for 3 minutes then the supernatant was carefully decanted from the centrifuge tube. The pellet was then triturated with 10 ml of a 9:1 water / methanol mixture before a second centrifugation. The decantation and trituration process was repeated twice more. After the final decantation the product was dried for 24 hours over phosphorus pentoxide. The isolated product was used in the next step of the synthesis without further purification.

Yield: 307 mg (0.16 mmol, 89%). ESI-MS: m/z = 1969.1 [MH^+] (calc = 1969.4). TLC: chloroform / methanol / water (65:25:4), R_f = 0.50 (lit = 0.47).

4.2.2 *Synthesis of 2,4-dinitrophenyl-pyridinium-3-carboxamide chloride (DNPC)*

Nicotinamide (4.0 g, 0.033 mol) and 2,4-dinitrophenylchloride (20.0 g, 0.1 mol) were heated to 90 °C and stirred together into a homogenous melt. After 1 hour the melt was dissolved in methanol (30 ml) then treated with cold diethyl ether (300 ml). A soft yellow solid precipitated and was separated from the supernatant by decantation. The solid was redissolved in the minimum amount of methanol and precipitated a second time by the addition of cold ether. The precipitate was dried under suction, dissolved in high purity water (100 ml) and heated at reflux with powdered carbon (~ 0.5 g) for 30 minutes. The carbon was removed by filtration and the filtrate concentrated *in vacuo*. The residue was further dried *in vacuo* to give yellow-brown crystals of product. Yield = 6.81 g (0.021 mol, 64 %). ESI-MS: m/z = 289.1 [M^+] (calc = 289.2). H^1-NMR (D_2O): δ = 9.50 ppm *(1H, s, pyridine H6)*, δ = 9.30 ppm *(1H, s, dinitrophenyl H3)*, δ = 9.25 ppm *(1H, d, dinitrophenyl H5)*, δ = 9.20 ppm *(1H, d, dinitrophenyl H6)*, δ = 8.85 ppm *(1H, dd, pyridine H2)*, δ = 8.35 ppm *(1H, dd, pyridine H3)*, δ = 8.15 ppm *(1H, d, pyridine H4)*. Melting point: 139 - 141 °C.

4.2.3 *Synthesis of gram-2-(nicotinamido)ethyl carbamate (gAN)*

Crude gE (210 mg, 0.11 mmol) was dissolved in methanol (1.5 ml) with stirring. DNPC (38 mg, 0.12 mmol) was added a few granules at a time to the stirring gE solution. The addition resulted in an instant and definite colour change from pale yellow to dark red. The mixture was stirred at room temperature for 2 hours.

Addition of ice-cold high purity water (10 ml) to the reaction mixture resulted in the precipitation of the product as a pale yellow solid. The precipitate mixture was

centrifuged at 3000 rpm for 3 minutes then the supernatant was carefully decanted from the centrifuge tube. The pellet was then triturated with 10 ml of cold water before a second centrifugation. The decantation and trituration process was repeated twice more. After the final decantation the product was dried for 24 hours over phosphorus pentoxide. The crude yield was 162 mg. The crude product needed further purification by reverse-phase HPLC before undergoing electrochemical analysis.

4.2.4 *Purification of gram-2-(nicotinamido)ethyl carbamate (gAN)*

Reverse-phase high-pressure liquid chromatography (RP-HPLC) was carried out on a methanol solution of crude gAN. A Supelcosil LC-8 column (25 cm × 10 mm × 5 μm), Perkin Elmer series 200ic pump, Shimadzu CTO-6A column oven and Waters 486 tunable absorbance detector (λ = 280 nm) were used. A combination of three eluant solvents was used: Solvent A = 99.9% acetonitrile / 0.1% trifluoroacetic acid; Solvent B = 5% isopropanol / 94.9% water / 0.1% trifluoroacetic acid; Solvent C = 90% methanol / 9.9% water / 0.1% trifluoroacetic acid. The solvent elution profile is shown in Table 5.

Table 5. *HPLC elution profile for gAN purification.*

% A	% B	% C	Time (min)	Flow rate (ml/min)
0	*100*	*0*	*1*	*2*
2	*28*	*70*	*2*	*2*
2	*0*	*98*	*2*	*2*
5	*0*	*95*	*10*	*2*
10	*0*	*90*	*3*	*2*
0	*100*	*0*	*1*	*2*

All solvents used were of HPLC grade. HPLC runs were carried out at room temperature. Each eluted fraction was submitted for ESI-MS analysis: the fraction found to contain gAN *($t \sim 15.6$ mins)* was retained, the solvent removed *in vacuo* and the residue redissolved in methanol (100 ml).

The crude gAN was found to be 39% pure by HPLC trace integration (0.03 mmol, 17%). ESI-MS: m/z = 2074.4 [M^+] (calc = 2074.5).

4.2.5 *Standardisation of gAN solution*

Before performing electroanalytical experiments it was necessary to determine the concentration of the methanol solution of purified gAN. The UV-visible spectrum of gAN was measured using a Pharmacia Biotech Ultraspec 4000 UV-visible spectrophotometer and quartz cuvettes. The UV absorbance of the sample was measured over a wavelength range of 190 - 800 nm.

4.3 Results and discussion

The pentadecapeptide gE (**4**) was synthesised from gramicidin D (gD) and ethylenediamine as outlined in Scheme 1. Gramicidin D is a naturally occurring, commercially available mixture of 85% gramicidin A (**1**), 10% gramicidin B and 5% gramicidin C. The gE molecule has an amino group, protonated under physiological conditions, which is bound to the C-terminus by a flexible carbamate linker vide the *ball and chain* model. The gA C-terminus alcohol attacks the chloroformate carbonyl resulting in loss of the chloride. The carbonyl of the gA-chloroformate intermediate (**3**) is then attacked by ethylenediamine resulting in formation of the desired gE product (**4**) and the resonance stabilised, low pK_a *p*-nitrophenyl anion.

Scheme 1. *Synthesis of gE.*

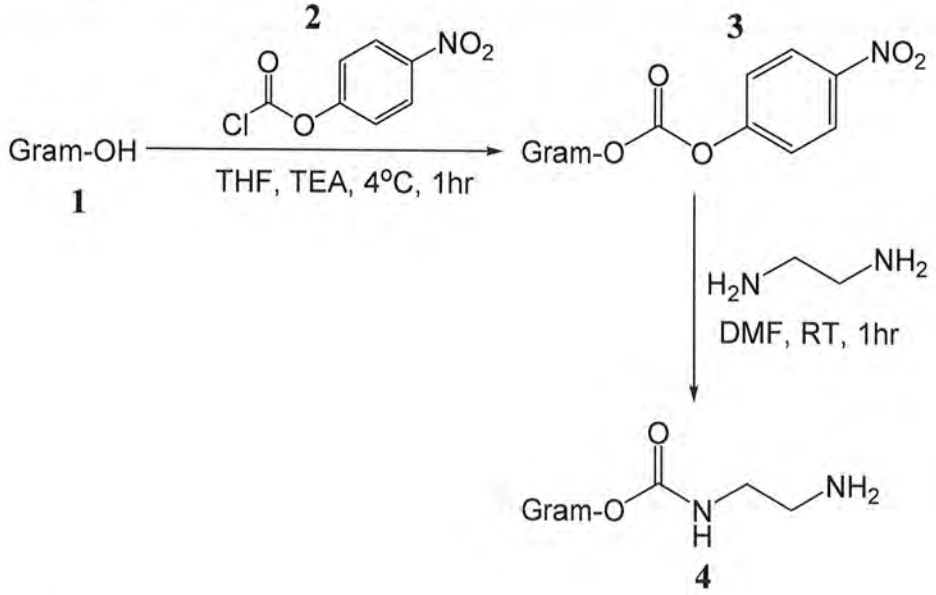

Reaction of a room temperature methanolic solution of gE (**4**) with 2,4-dinitrophenyl-pyridinium-3-carboxamide chloride (DNPC) (**5**) resulted in the desired nicotinamide-modified analogue gAN (**6**) (Scheme 2):

Scheme 2. *Synthesis of gAN.*

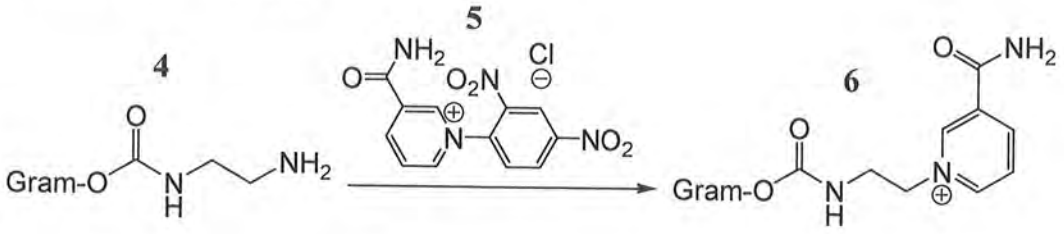

The mechanism of gAN (**6**) formation is shown in Scheme 4.

The crude gAN (**6**) product was purified by RP-HPLC with detection of the product achieved by measuring the UV absorbance of the eluant at 280 nm. Samples were hand injected and eluant fractions collected manually. The HPLC chromatogram of gAN (**6**) is shown in Figure 27. The chromatogram shows the purified peak as less intense than the crude peak. This is because the purified sample had been eluted once already and was therefore more dilute when re-injected to the column. ESI-MS of the eluted gAN (Figure 28) confirms the presence of the molecular ion at m/z = 2074.4 [gAN^+]. For the purposes of contrast an ESI-MS of the starting material is shown in Figure 29.

The DNPC (**5**) was synthesised according to the method of Lettré (Scheme 3):[9]

Scheme 3. *Synthesis of DNPC.*

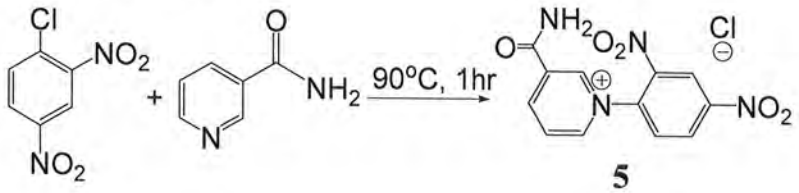

Figure 27. *HPLC chromatograms of crude and purified gAN.*

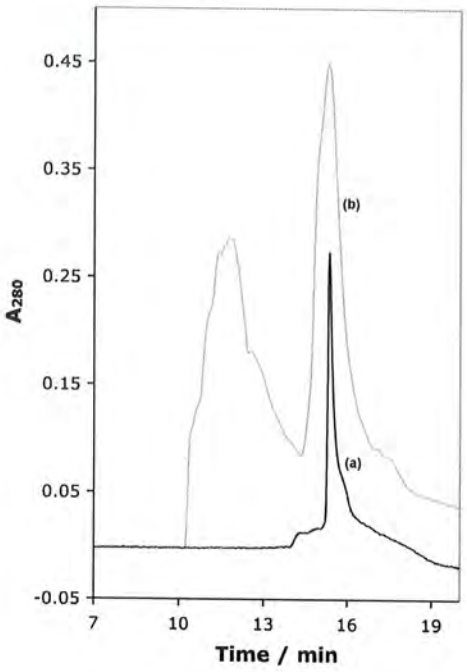

(a) Purified (~ 90 %) gAN previously eluted from the column and redissolved in methanol.

(b) Crude gAN (~ 39 %) isolated from synthesis.

Figure 28. *Electrospray ionisation (positive ion mode) mass spectrum of gAN.*

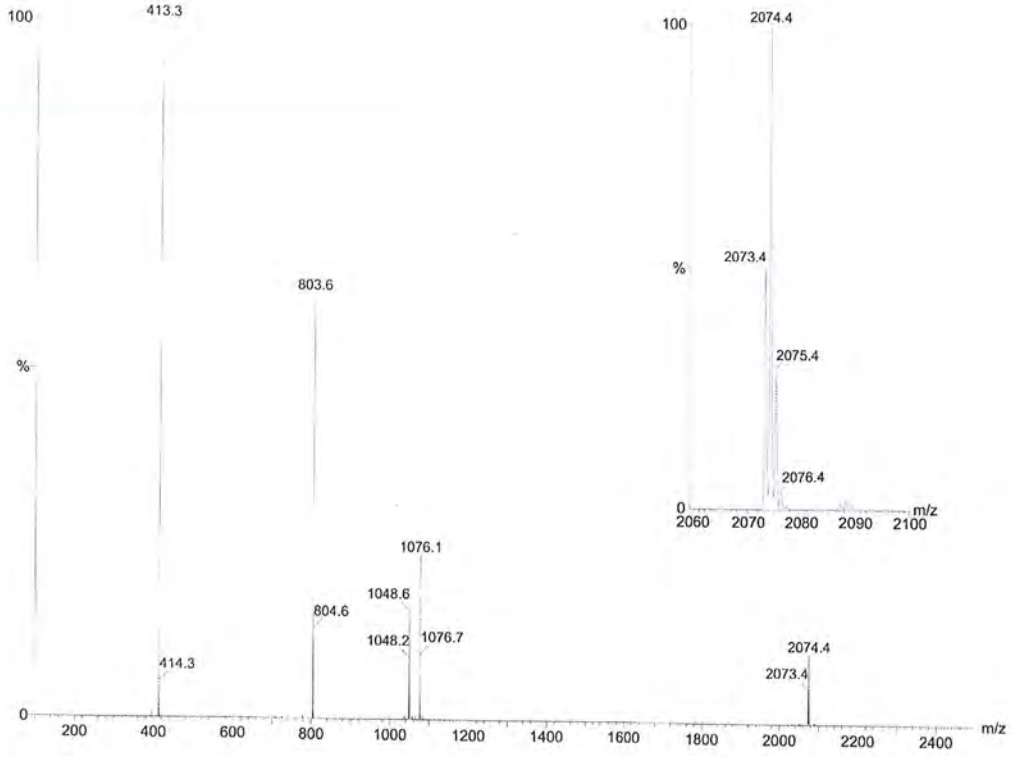

ESI-MS of gAN HPLC elution peak (a) shown in Figure 27. Inset shows molecular ion at m/z = 2074.4.

Figure 29. *Electrospray ionisation (positive ion mode) mass spectrum of gD.*

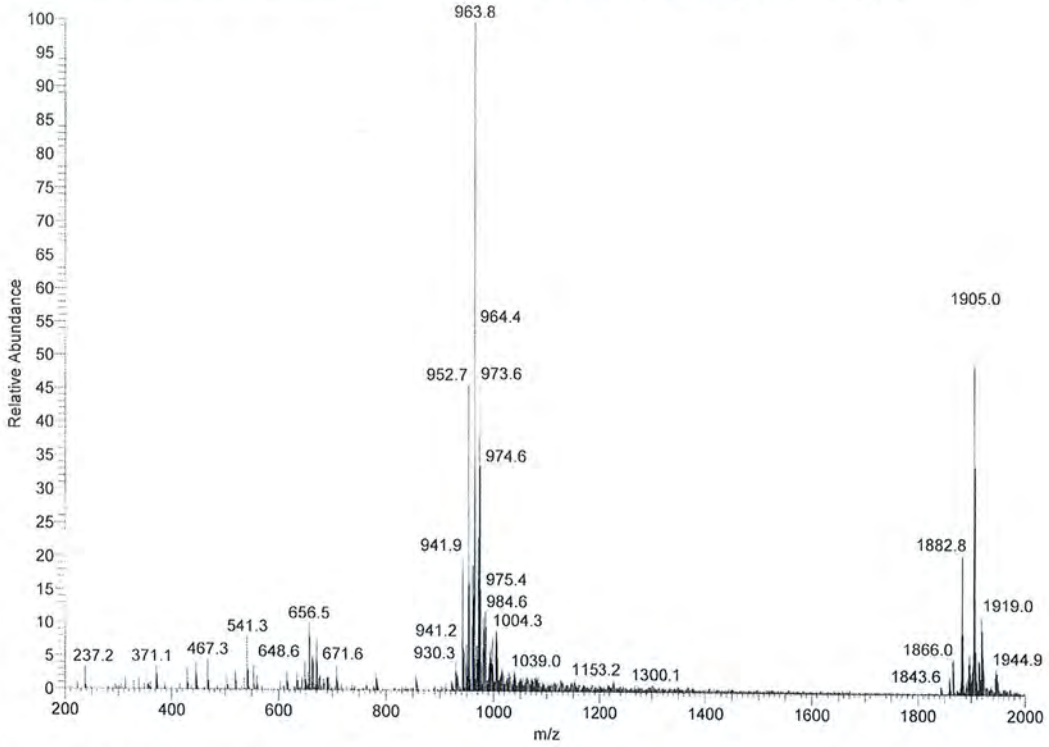

ESI-MS of gD starting material. Peak at m/z = 1905.0 corresponds to gA + Na^+.

Scheme 4. *Mechanism of gAN formation.*

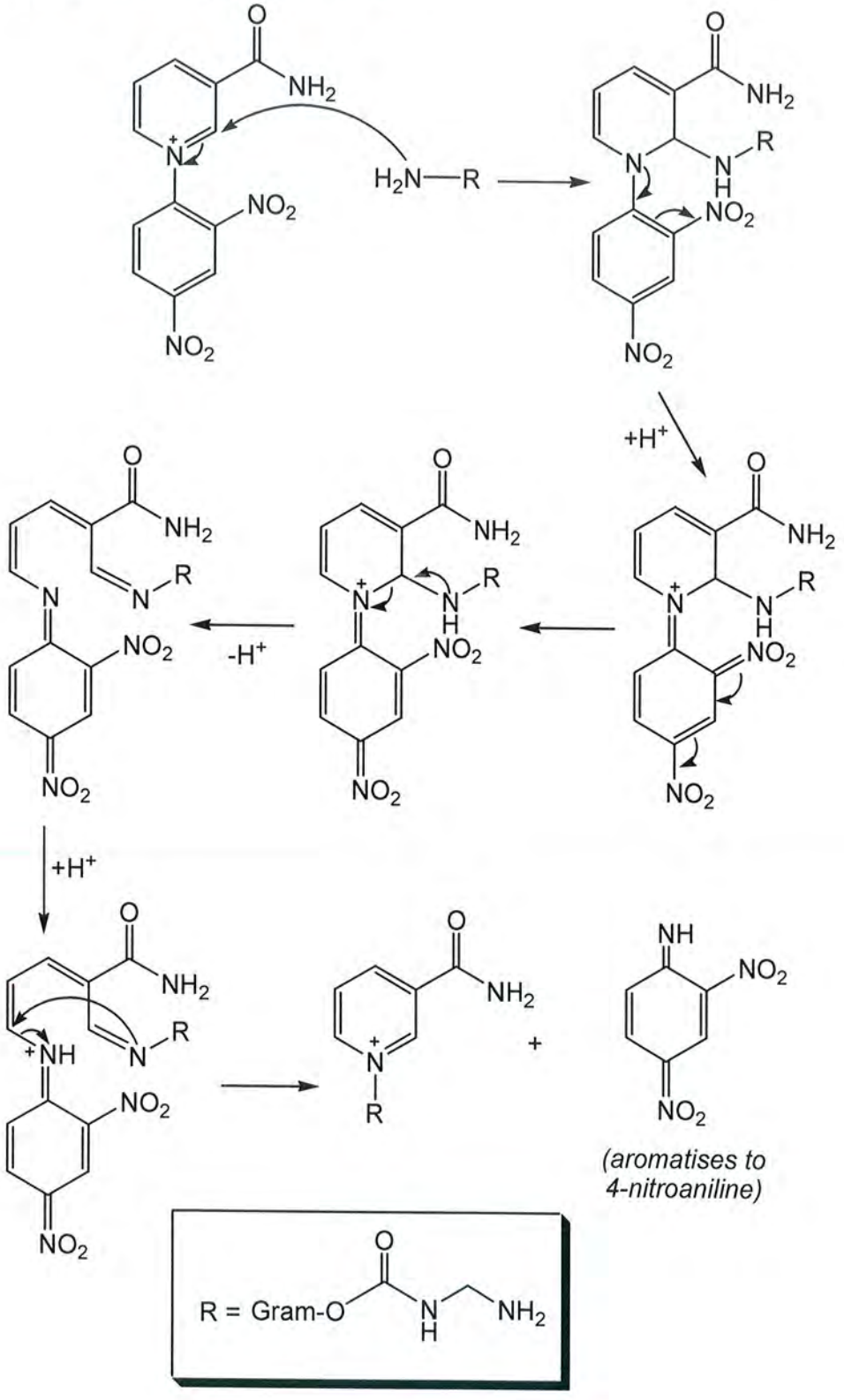

The gAN-containing HPLC fraction was reduced *in vacuo* to remove all trace of the elution solvent before being redissolved in methanol to make a working stock solution. The concentration of the gAN stock was determined by UV absorbance measurements and quantification of the aromatic tryptophan sidechains at 280 nm. The UV absorbance, A, is given by the Beer-Lambert law:

$$A_\lambda = \varepsilon_\lambda cl \qquad (68)$$

Where ε is the extinction co-efficient, c the concentration of the peptide and l the pathlength of the cuvette.

The extinction co-efficient of tryptophan is 5690 mol^{-1} dm^3 cm^{-1} at 280 nm,[10] therefore the extinction co-efficient of gAN due to the four tryptophans is 22760 mol^{-1} dm^3 cm^{-1} at 280 nm. Concentration of gAN = 0.12 mM.

To demonstrate the dependence of absorbance on sample concentration at 280 nm, Figure 30 shows the affect of adding gAN solution to a cuvette containing 1 ml of methanol.

Figure 30. *UV spectrum of gAN solution.*

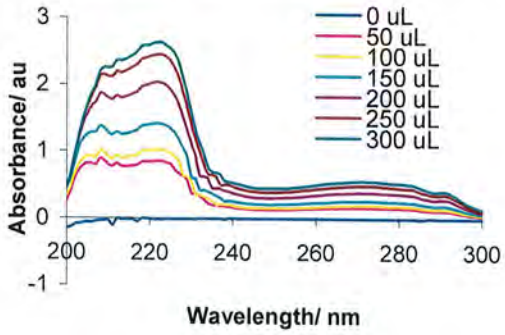

(a) Varying amounts (0 – 300 µL) of gAN stock solution were added to a cuvette containing 1 mL of methanol. The UV spectrum of each sample was recorded. The UV spectrum of 100 % gAN stock was also recorded (not plotted).

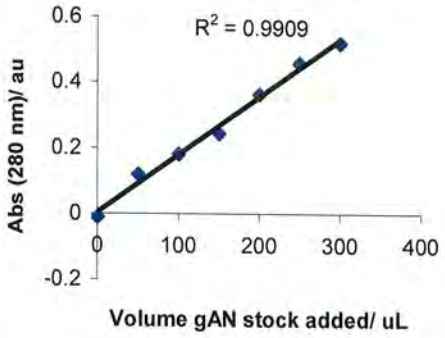

(b) Linear relationship between absorbance and gAN concentration. The extinction co-efficient of tryptophan is 5690 mol^{-1} dm^3 cm^{-1} at 280 nm,[10] therefore the extinction co-efficient of gAN due to the four tryptophans is 22760 mol^{-1} dm^3 cm^{-1} at 280 nm. The concentration of the gAN stock was determined as 0.12 mM by the Beer Lambert law.

4.4 References

1. (a) R. R. Ketchem, K. C. Lee, S. Huo and T. A. Cross, *J. Biomol. NMR*, 1996, **8**, 1; (b) B. A. Wallace, *Bioessays*, 2000, **22**, 227
2. J. Morrow, W. Veatch and L. Stryer, *J. Mol. Biol.*, 1979, **132**, 733
3. G. Szabo and D. Urry, *Science*, 1979, **203**, 55
4. E. Bamberg, H. Apell and H. Alpes, *Proc. Natl. Acad. Sci. USA*, 1977, **74**, 2402
5. T. Vogt, J. Killian, R. Demel and B. De Kruijff, *Biochim. Biophys. Acta*, 1991, **1069**, 157
6. G. A. Woolley, A. S. I. Jaikaran, Z. Zhang and S. Peng, *J. Am. Chem. Soc.*, 1995, **117**, 4448
7. G. A. Woolley, V. Zunic, J. Karanicolas, A. S. I. Jaikaran and A. V. Starostin, *Biophys. J.*, 1997, **73**, 2465
8. C. M. Armstrong and F. Bezanilla, *J. Gen. Physiol.*, 1977, **70**, 567
9. H. Lettré, W. Haeda and E. Ruhbaum, *Justus Liebigs Ann. Chem.*, 1953, **579**, 123
10. C. K. Mathews and K. E. Van Holde, *Biochemistry (2nd Edition)*, Benjamin Cummings, Menlo Park, California, 1995

Chapter 5

SECM of Peptide Ion Channels

5.1 Introduction

The study of the interaction of channel-forming synthetic and natural peptides within phospholipid membranes is an area of increasing interest.[1,2,3] The pore-forming mechanisms and ion-selectivities of several peptide antibiotics have been extensively investigated using a variety of techniques, amongst the most prevalent of which are fluorescence microscopy, FT-IR, electrophysiology, AFM and NMR. The dynamics of charge-transfer in bilayer lipid membranes (BLMs) is usually probed by patch-clamp amperometric microelectrodes to probe ion-fluxes in biological membranes[4,5,6] In this chapter scanning electrochemical microscopy (SECM) using ultra microelectrodes (UMEs) was used for further investigation of the ionic conduction of gA and its potential-dependent analogue gAN.

5.1.1 *SECM and ion channels*

The development of scanning electrochemical microscopy (SECM) techniques in the late 1980s by Bard and his co-workers,[7] resulted in several publications on the use of this technique in probing the kinetics of ion-transfer (IT)[8,9,10] and electron-transfer (ET) processes[11,12,13] on monolayers at the interface between two immiscible electrolyte solutions (ITIES). Tsionsky, Bard and Mirkin[13] used SECM to probe the kinetics of ion-transfer processes on the surface of BLMs using approach curves.

Amemiya and Bard used voltammetric ion-selective microelectrodes to study K^+ transfer through gramicidin channels in horizontal BLMs prepared by the brush technique.[8,10] The transport of non-electroactive ions like K^+, Na^+ and Ca^{2+} is of interest because of the trans-membrane passage of these ions in biological systems. K^+-selective microelectrodes were fabricated from pulled borosilicate capillaries with silanised walls and filled with a valinomycin in dichloroethane solution. The microelectrodes were characterised by the steady-state tip current in a range of K^+ concentrations. The ion-selective microelectrodes were used in the SECM feedback and generation-collection modes to probe K^+ transfer through gramicidin channels in glycerol monooleate bilayers.

Mauzeroll and co-workers[14] used SECM in the substrate-generation tip-collection (SG-TC) mode to monitor the passage of thallium(I) ions across gramicidin half-channels imbedded in a dioleoylphosphatidylcholine (DOPC) monolayer supported on a thallium amalgam HMDE. In SG-TC an electroactive species is generated by the substrate (the HMDE) and allowed to diffuse into bulk solution where is it detected by a UME (the SECM tip). In these experiments the electroactive species was Tl^+ which was generated when the thallium amalgam HMDE was biased to -0.75 V. The Tl^+ was then allowed to diffuse through to the sensing UME, which was biased at -1.1 V. The tip transient response for the collection of Tl^+ was repeated at several tip-substrate distances. The SG-TC experiment was repeated with HMDE substrates supporting bare and gramicidin-treated DOPC monolayers. An apparent heterogeneous rate constant (k_{het} = 2.8 ($\pm$ 0.1) $\times$ 10^{-4} cms^{-1}) for the transport of Tl^+ through the gramicidin half-channels to the tip was obtained.

More recently Cliffel and co-workers have used SECM to probe BLM resistivity, insertion of alamethicin pores and mass transport of $Ru(NH_3)_6^{3+}$ across reconstituted phosphatidylcholine (PC) bilayers.[15] BLMs were assembled over a Teflon foil aperture by a mechanism analogous to the closing of a zipper where the tails of the two opposing monolayers intercalate to form the bilayer.[16] Since the Teflon is much thicker than the BLM the two monolayers are unable to zip together all the way to the edge of the aperture. As a result of this a region forms at the edge of the aperture where the two monolayers are effectively separated by a pocket of trapped solvent. Because of its transparent appearance in optical microscopy the edge region can also be described as an annulus. The solvent rich annulus is much less resistant to $Ru(NH_3)_6^{3+}$ than the centre of the BLM as demonstrated by increased feedback current, due to increased passive ion transport in the annulus region. Area scan experiments were also used to verify the voltage control of the alamethicin channel. As previously mentioned in chapter 3 alamethicin is believed to form BLM channels in agreement with the barrel-stave model.[17] The alamethicin monomers adsorb parallel to the lipid membrane and only incorporate themselves into the membrane when exposed to sufficient membrane potential (50 mV). A marked increase in $Ru(NH_3)_6^{3+}$ permeation was observed when a positive potential was applied to alamethicin treated BLM, corroborating potential-dependent channel formation and activation.

5.1.2 *Biological membrane behaviour*

A biological membrane inserted with an ion channel can be considered analogous to a circuit component. The dielectric constant is a measure or the relative membrane capacitance which is related to the capacitance $C = Q/E$ where Q is the charge on the capacitor and E the potential. The lipid membrane has a dielectric constant, $\varepsilon \sim 2.0$ compared to ~ 80 for water at room temperature.[18] Insertion of gA creates a more polar environment, increasing the dielectric constant and allowing passage of hydrophilic cations. The effective dielectric constant, ε_{eff}, is assumed to be ~ 20.[19] When a porated insulating BLM membrane is inserted between two ionic solutions, the ionic current is limited by the transfer of permeant ions across the membrane.[20]

The difference between the concentration of cations on either side of the membrane induces a diffusion flux, J, of ions which is dependent on diffusion coefficients, D, in the ion-channel and the concentration gradients on either side of a membrane porated with ion-channels and the potential gradient:

$$\Delta J_i = -\Delta D\left(\frac{\partial \Delta c_{(1-2)}}{\partial x}\right) = v_i + \left(\frac{d\tau_i}{dt}\right) \qquad (69)$$

Where ΔD is the difference in diffusion co-efficients of the permeable cations in the aqueous phase and in the membrane ion channel, v_i is the ion transfer rate and τ_i is the concentration of ions on the membrane. The charge per unit time is the current, which splits into capacitive and a Faradaic term:[21]

$$i = \sum z_i F A J_i = \sum z_i F A v_i + \sum z_i F A\left(\frac{d\tau_i}{dt}\right) \qquad (70)$$

$$= I_F + \left(\frac{dQ}{dt}\right) = I_F + I_C$$

$$v_i = k_i^{1\to 2}\left((c_{i1} - c_{i2})exp\left[-z_i F\left(\frac{\Delta\phi_1 - \Delta\phi_2}{RT}\right)\right]\right) \qquad (71)$$

Where A is the effective area of the membrane, ϕ_1 and ϕ_2 are the electrochemical potentials in phase 1 and 2 and c_{i1} and c_{i2} are the concentrations of permeable ions in

phase 1 and 2 respectively and $k_i^{1\to2}$ is the potential dependent rate constant of ion transfer from phase 1 to phase 2 across the membrane.

As the capacitance of the membrane is fixed, the ionic current flows until the charge on the capacitor is satisfied. An excess of electrolyte solution satisfies this condition. As increasing potential gradient is applied, an increasingly polar environment is created within the ion channels. In contact with ions of appropriate radii and charge, an increase in current is expected as ions pass through the channels.[19]

Matsue and co-workers tested the permeability of lipid membrane embedded alamethicin channels to $Ru(NH_3)_6^{3+}$, $Fe(CN)_6^{3-}$ and I^-.[22] A soybean lecithin membrane was prepared over a pinhole and was mounted between the compartments of a two compartment cell, each of which was filled with equimolar KCl solution. Equal amounts of alamethicin were added to each compartment. The sensing UME tip was approached to the *cis* side of the membrane and the redox active species was added to the *trans* compartment. As the tip was biased and at membrane potentials > 50 mV the current began to increases exponentially with potential, signifying the potential-dependent insertion of the alamethicin monomer bundles. The ionic current increased with 5.6^{th} power of the alamethicin concentration suggesting an average of 5.6 monomers per channel in agreement with the barrel stave model. The equal compartment concentrations and large excess of KCl over the redox ion meant that the diffusion current attributable to the redox ion was negligible. Furthermore, owing to the large excess of KCl ionic current detected at the UME was attributed predominantly to the movement of K^+ and Cl^- ions with the electroactive species having minimal influence. As in SECM the current response was dependent on the tip-substrate distance, with greater currents observed approaching the membrane surface. The ionic flux and permselectivity of each ion was calculated from the current response and provided a good match with digitally simulated data. The relative permselectivities, P_R, of the alamethicin channel were found to be 1.0 (by definition), 0.5, 0.27, 0.03 and 0.3 for the K^+, Cl^-, $Ru(NH_3)_6^{3+}$, $Fe(CN)_6^{3-}$ and I^- ions respectively. The P_R value of $Ru(NH_3)_6^{3+}$ is comparible to the relative diffusion coefficient, indicating that the selectivity reflects the different mobility of K^+ and $Ru(NH_3)_6^{3+}$. The low selectivity for the $Fe(CN)_6^{3-}$ ion, which is small enough to pass through the alamethicin channel, was

explained in terms of electrostatic repulsion between the channel lumen carbonyl groups and the multicharged anion.

In our experiments egg phosphatidylcholine BLM, formed over a microporous polycarbonate membrane support,[19] was inserted between two aqueous electrolyte solutions containing equal and excess concentrations of the redox active $Fe(CN)_6^{3-}$ ion to maintain an equal potential on either side of the membrane and to allow the electode to remain unpolarisable for ionic current measurements (for scenario 2 and 3 *vide infra*). The schematic configuration is:

cis *trans*

$$x\ \mathrm{M}\ (\mathrm{K^+/TMA^+, Cl^-}) + \mathrm{y\ M}\ (\mathrm{4K^+, Fe(CN)_6^{3-}}) \Big| \text{Membrane} \Big| x'\ \mathrm{M}\ (\mathrm{K/TMA^+, Cl^-}) + \mathrm{y\ M}\ (\mathrm{4K^+, Fe(CN)_6^{3-}})$$

In the cell the redox active $Fe(CN)_6^{3-}$ ions influence the Faradaic current at the UME tip and maintain the potential gradient across the membrane. With the BLM inserted between two aqueous solutions three different scenarios exist:

1. The control membrane comprised of a bilayer lipid membrane (BLM) painted on a polycarbonate membrane behaves as an insulator, except when exposed to potentials high enough to porate the membrane (E_{porate}). In the presence of an electroactive species, $Fe(CN)_6^{3-}$, therefore, if the UME tip potential is held at a value conducive to reducing the $Fe(CN)_6^{3-}$ species, as the tip approached the insulating surface, tip current is affected by hindrance of the diffusion of the electroactive species, showing a negative feedback approach curve.
2. With gA inserted in the lipid membrane, the ion channel forms a locus at which permeable cations can cross the membrane and accumulate depending on the concentration gradient. Approach curves measuring ionic current (see experimental section) show pH and temperature dependent conducting behaviour, which is ***independent*** of the potential gradient applied to the membrane.
3. With a gAN inserted membrane, the channel does not allow cations to permeate through the channel when gAN is oxidised due to charge repulsion between the oxidised nicotinamide moiety and the cation and channel occlusion by the pendant nicotinamide. In the reduced state (at $< \sim$ -0.52 V) cations of suitable size and charge are able to flow through the channel. Approach curves therefore show a

potential ***dependent*** feedback behaviour as the UME tip is in close proximity (~10 μm) to the gAN porated membrane. This is represented in Figure 31:

Figure 31. *gAN / gAN$^+$ redox processes at the electrode surface.*

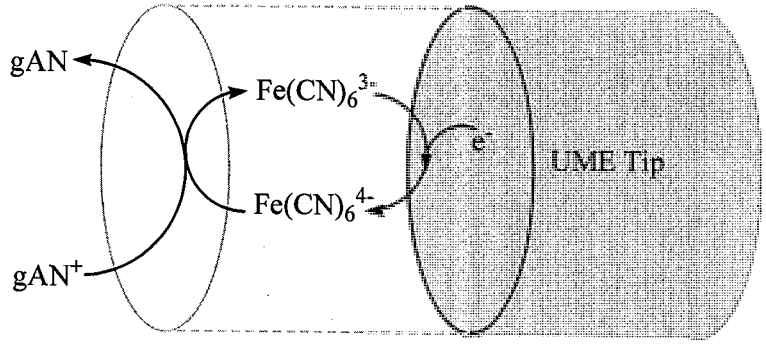

The exact theoretical treatment of IT and ET processess in this situation is complex and will need further investigations to obtain a complete theoretical analysis.

5.1.3 *The chemistry of Prussian Blue*

Prussian Blue (PB) ($Fe_4^{III}[Fe^{II}(CN)_6]$) has a basic cubic structure consisting of alternating Fe^{3+} and $Fe(CN)_6^{4-}$ located on a face centred cubic lattice (Figure 32). At the centre of the unit cell there is a cavity of sufficient size to entrap cations. The Fe^{3+} ions are surrounded by an octahedral arrangement of nitrogen atoms and the Fe^{2+} by carbon atoms. The unit cell has dimensions of 10.2 Å as determined by single crystal electron diffraction.[23] It is pertinent to give a brief introduction to PB chemistry here because its use as a dual-purpose electrolyte and electrochromic indicator will be encountered later on in this chapter.

In solution PB exists as a dispersed colloid, almost homogeneous in nature. At potentials negative of 0.2 V the outer sphere Fe^{3+} ions undergo reduction. The reduced compound, known as Everitt's salt (ES) ($K_2Fe^{II}[Fe^{II}(CN)_6]$), has less colour than PB and is charged balanced by entrapment of potassium ions in the central cavity. A fully oxidised form (Prussian Yellow (PY): $Fe^{III}[Fe^{III}(CN)_6]$) and mixed valence form (soluble Prussian Blue (sPB): $KFe^{III}[Fe^{II}(CN)_6]$) are also known.

$$Fe_4^{III}[Fe^{II}(CN)_6] \rightarrow 3\,Fe^{III}[Fe^{III}(CN)_6] + Fe^{3+} + 3e \qquad (72)$$

$$Fe^{III}[Fe^{III}(CN)_6] + K^+ + e = KFe^{III}[Fe^{II}(CN)_6]$$

$$KFe^{III}[Fe^{II}(CN)_6] + K^+ + e = K_2Fe^{II}[Fe^{II}(CN)_6]$$

Figure 32. *Prussian Blue unit cell.*

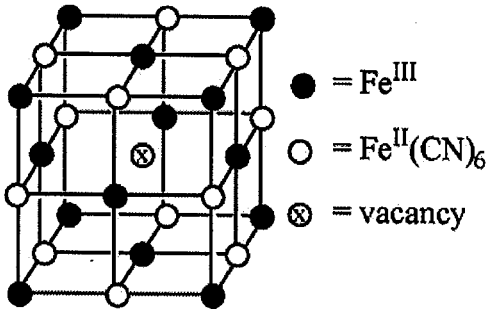

Schematic diagram of the Prussian Blue unit cell. The lines between the ions represent CN bridges. At potentials < 0.2 V the Fe^{3+} ions reduce and the charge is balanced by a cation occupying the central lattice vacancy.

Rb^+ and Tl^+ ions are also known to permeate the lattice structure, substituting the two K^+ ions of the ES.[24] Unlike K^+ containing ES, where the K^+ ions are free to permeate through the lattice structure, the Tl^+ / Rb^+ analogue has one of the cations irreversibly bound in the central cavity. This irreversible binding, due to lattice contraction associated with the first Tl^+ / Rb^+ being expelled during the initial stage of reoxidation, prevents the second ion from leaving the cavity thereby inhibiting complete oxidation back towards PY. At very low potentials (-1.36 V vs. Ag/AgCl) the entrapped Tl^+ ion can leave the central cavity and is reduced to metallic thallium. In this case the charge of the ES is balanced by influx of K^+ ions.

Robin performed the first, thus far only, detailed interpretation of the electronic spectrum of PB.[25] He concluded that the vivid blue colour was, on the most part, a result of charge transfer between the $Fe^{II}(CN)_6^{4-}$ and Fe^{3+} ions. Nearly all the optical electrons (99 %) are localised on the $Fe^{II}(CN)_6^{4-}$ ions in the ground state. The paper also suggested the molecular orbital (MO) diagram for PB, which is shown in Figure 33. Each iron ion has at least five d electrons and the remaining eleventh electron is located in either the carbon or nitrogen hole, hence the ambiguity in constitution. The MO diagram shows that the lowest available orbital in the nitrogen hole is less antibonding than the corresponding orbital in the carbon hole, so the eleventh electron

would be thought to favour a position there. Though the eleventh electron is thought to favour the nitrogen hole it is believed inter-electronic repulsion effects actually consort to place the electron in the carbon hole, which is the location depicted in the figure below. The definitive configuration is still in doubt.

Figure 33. *Molecular orbital diagram of PB (adapted from reference 25).*

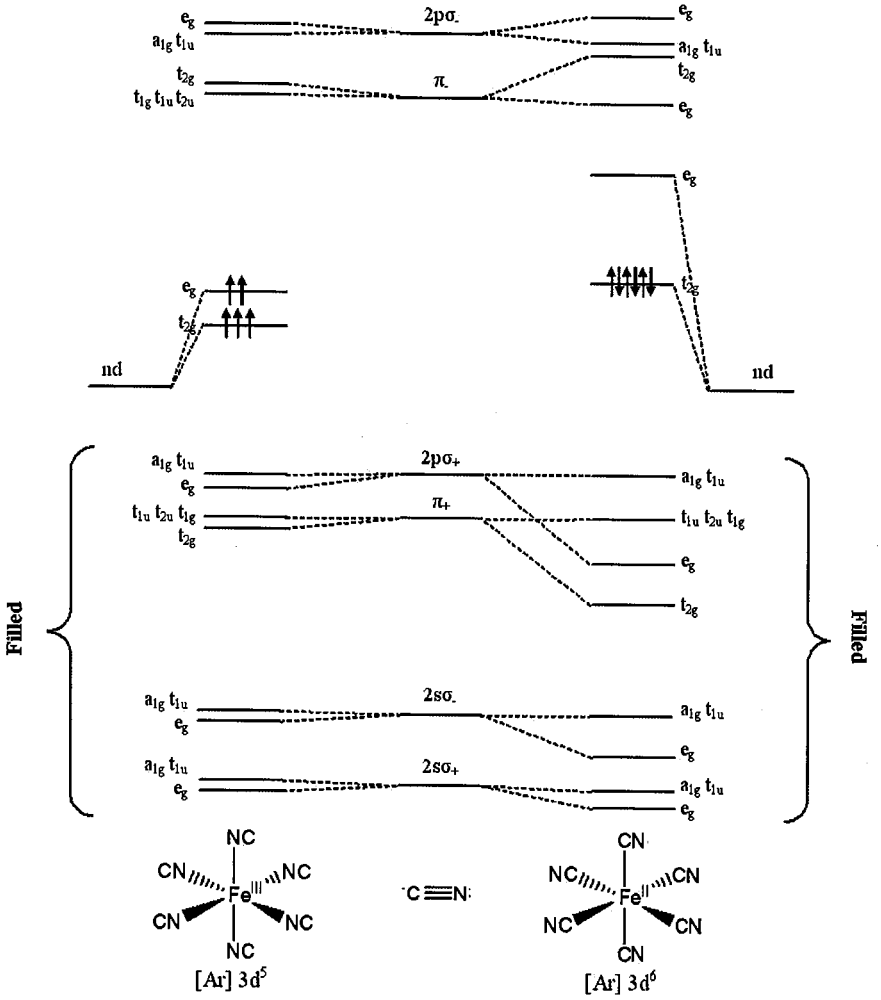

Since the size and charge of Tl^+ is comparable to that of K^+ it could make an interesting permeant ion for the gA and gAN channels. In previous studies Tl^+ has successfully been employed as a permeant cation for gA half-channels inserted in various lipid monolayers.[14,26] K^+ has an ionic radius of 152 pm (6 co-ordinate, octahedral) and Tl^+ has an ionic radius of 164 pm (6 co-ordinate, octahedral).[27] Furthermore the electroactivity of Tl^+ gave rise to the possibility of directly observing movement across the gAN channel, in contrast to the electroinactive K^+ ions, which can not be directly

monitored although their permeation is clearly inferred by the variation in tip current in proximity to the membrane.

5.1.4 *Summary of Chapter 5*

In this chapter SECM using UMEs was used for further investigation of the ionic conduction of gA and its potential-dependent synthetic analogue gAN. The peptide channels were introduced to polycarbonate supported BLMs, which were partitioned between two electrolyte solutions under experimental conditions. The potential-dependent switching properties of gAN have been determined by acquiring SECM feedback curves over a range of membrane applied potentials and electrolyte conditions.

An experiment was designed to test the permeation of gA / gAN to K^+ / Tl^+ using PB as dual-purpose electrolyte and electrochromic indicator. With a K^+ concentration gradient across the membrane biased at negative potential it was expected that K^+ ions would migrate across the peptide channels and pass through the cavities in the PB unit cell. Conversely, with a Tl^+ gradient and negative bias the Tl^+ ions should migrate across the peptide channels and become irreversibly bound in the cavities of the PB unit cell. The presence of Tl^+ ions in the PB central cavities can be expected to influence the $Fe^{II}(CN)_6^{4-} \rightarrow Fe^{3+}$ charge transfer process, resulting in a colour change detectable by UV spectroscopy. In the case of the K^+ gradient, any colour change due to K^+ occupation of the PB cavities should be less pronounced due to the transient nature of these ions.

5.2 **Experimental procedure**

5.2.1 *General approach used in all experiments*

5.2.1.1 *Apparatus*

SECM data was collected using a Uniscan Instruments SECM 270 (Uniscan Instruments, Buxton, UK) in approach curve or area scan mode. The SECM 270 incorporates two PG 580 potentiostats (Uniscan Instruments, Buxton, UK), a tip positioning device and software to allow data collection by personal computer. The cell was a two-compartment glass cell, with inter-compartment aperture on which to mount the sample. A 10 μm platinum UME tip (CH Instruments Ltd., Austin, US) was used as the WE, the RE was an aqueous Ag/AgCl electrode (Bioanalytical Systems, West Lafayette, US) and the CE was a self-fabricated 1 cm^2 platinum flag. Between

experiments the UME tip and platinum flag were thoroughly cleaned by soaking in 3:1 (v/v) concentrated sulphuric and nitric acids for 2 minutes, followed by sonication in high purity water for 2 minutes, rinsing with methanol and drying under a stream of nitrogen.

5.2.1.2 *Preparation of supported BLMs*

Supported BLMs were prepared on Whatman Track-Etched polycarbonate membranes (Whatman, Brentford, UK) of 25 mm diameter and 100 nm pore size. Egg phosphatidylcholine (EPC) in chloroform (200 µl of a 100 mg/ml EPC solution) was transferred to a 50 ml round-bottomed flask and the solvent removed *in vacuo*. The dried EPC residue was the redissolved in high purity water (1 ml) with vortexing for 15 minutes. The lipid solution was then painted onto polycarbonate membranes which were resting on a non-absorbent plastic surface. After fully air-drying the membranes were turned over, painted on the reverse and allowed to air-dry again.

Each sample was prepared by immersing an air-dried membrane in a solution of 100 µl of 0.12 mM peptide stock and 900 µl of high purity water (concentration of peptide ~ 10^{-5} M) and refrigerating for 24 hours prior to use. The peptide stock contained gA or gAN in methanol depending on the channel of interest. Control samples, containing methanol in the absence of peptide, were also prepared for comparison.

To avoid future repetition this method of preparing supported BLMs will be referred to as the '*standard brush technique*'.

5.2.1.3 *Cell set-up*

The two-compartment cell was clamped firmly in a Faraday cage within the limits of the UME tip motion. The cell was arranged so that the compartments were vertically aligned and the inter-compartment aperture was perpendicular to the tip axis. The two compartments were further separated by a tap which was kept open if the same electrolyte was used in both compartments. When two different electrolytes were used the lower (*trans*) compartment was filled with electrolyte first. To ensure no air bubbles were trapped in the tap region which could disturb the membrane during the measurements a small amount of *trans* compartment electrolyte was allowed to flow into the upper (*cis*) compartment before the tap was sealed. The *cis* compartment was then drained by pipette before being filled with its own electrolyte. The cell design, with

both compartments open to the air, ensures equal pressure on either side of the membrane. The sample membrane was then carefully positioned over the inter-compartment aperture and secured with a screw down plastic o-ring. The cell was approximately balanced using a spirit level. More precise balancing was achieved by measuring for reproducible feedback currents at different points on the membrane surface.

To avoid future repetition this method of setting up the two-compartment cell will be referred to as the '*standard cell set-up*'. A schematic of the standard cell set-up is shown in Figure 34.

Figure 34. *Schematic diagram of the SECM standard cell set-up.*

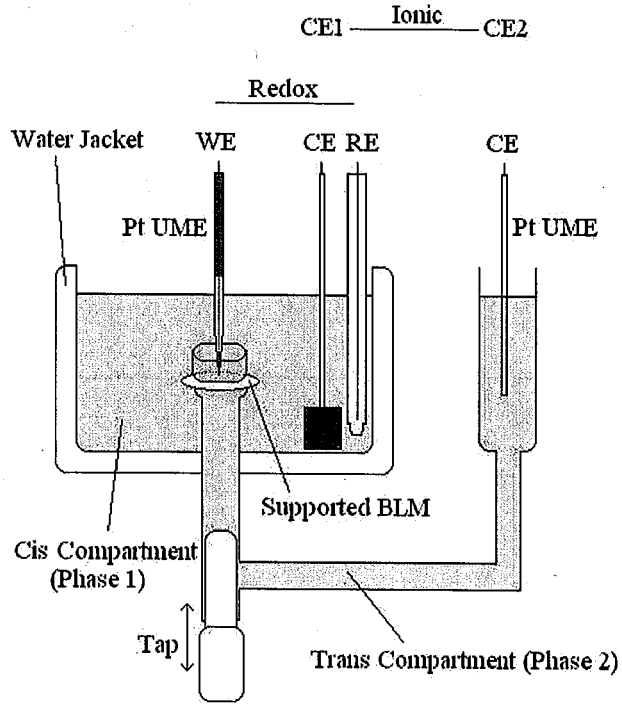

5.2.2 *Experiments using K_3FeCN_6 electrolyte*

5.2.2.1 *Feedback curves of gA and gAN channels in K^+ and $(CH_3)_4N^+$ solutions*

A gA sample, prepared by the standard brush technique, was fixed over the inter-compartment aperture of the standard cell set-up. Both compartments were filled with identical solutions of 0.1 mM $K_3Fe(CN)_6$ / 100 mM KCl electrolyte. The tip was lowered to a height of approximately 10 μm above the membrane surface. The tip-substrate distance was monitored by a video camera and carefully controlled by

carefully moving the tip towards the substrate to obtain maximum current. On occasions where the UME tip accidentally touched the membrane surface a dip in current was observed.

A potential of -1.0 V was applied to the UME tip which was then retracted from the membrane surface in 1 μm increments up to a tip-substrate distance of 110 μm (100 μm further from the membrane than the start position). The current was recorded as a function of distance throughout the divergent tip motion. Data were also collected for applied tip potentials at 0.1 V increments up to 1.0 V.

The feedback curve measurements described were repeated in 0.1 mM $K_3Fe(CN)_6$ / 100 mM KCl electrolyte with gAN and control membranes before the electrolyte was replaced with 0.1 mM $K_3Fe(CN)_6$ / 100 mM $(CH_3)_4NCl$ and otherwise identical measurements performed on the four membrane types.

5.2.2.2 *Area scan experiments*

The standard cell set-up was used with both compartments filled with 0.1 mM $K_3Fe(CN)_6$ / 100 mM KCl electrolyte and the tip was positioned at a tip-substrate distance of 10 μm. For platinum wire and foil targets the tip was biased at 0.6 V vs. Ag/AgCl. To observe the electroporation of a control membrane the tip was biased at -0.8 V. The tip was moved over the substrate region of interest at a rate of 1 μms^{-1} and the current recorded as a function of lateral tip position. Plots of the current profile were obtained.

5.2.2.3 *The variation of gAN switching potential with pH*

Potassium hydrogen phosphate buffers with pH 6.0, 6.5, 7.0, 7.5 and 8.0 were prepared by using the appropriate ratios of mono- and di-hydrogen phosphate salts. The buffers were made up to 0.1 mM in $K_3Fe(CN)_6$. A gAN sample, prepared by the standard brush technique, was fixed over the inter-compartment aperture of the standard cell set-up. Both compartments were filled with identical solutions of phosphate buffer electrolyte. Feedback curves were obtained at applied tip potentials of -1.0 V → 0.0 V at each buffer pH.

5.2.2.4 *The variation of gAN switching potential with temperature*

A gAN sample, prepared by the standard brush technique, was fixed over the inter-compartment aperture of the standard cell set-up. Both compartments were filled with identical solutions of pH 7.0 phosphate buffer which was also 0.1 mM in $K_3Fe(CN)_6$. The electrolyte temperature was regulated by passing heated water through the cell jacket. A thermostatic bath (Fisons Haake D8, accuracy ± 0.2 °C) was used and the electrolyte temperature was double-checked by digital thermometer. Feedback curves were obtained at applied tip potentials of -1.0 → 0.0 V over an electrolyte temperature range of 0 → 50 °C.

5.2.3 *Experiments using Prussian Blue electrolyte*

5.2.3.1 *Preparation of Prussian Blue*

An aqueous solution of iron(II) chloride (0.76 g, 6 mmol in 5 ml) was added to an aqueous solution of potassium ferricyanide (2.0 g, 6 mmol in 10 ml) with stirring. The dark blue solution was stirred for 30 minutes then left to stand overnight, resulting in the separation of the product as a fine black precipitate. The product was isolated by filtration, washed with water and dried at 80 °C for 24 hours.

5.2.3.2 *Feedback curves of gA and gAN channels in Prussian Blue solution*

A gA sample, prepared by the standard brush technique, was fixed over the inter-compartment aperture of the standard cell setup. A K^+ concentration gradient was established across the membrane by filling the *trans* compartment with 0.1 mM Prussian Blue / 10 mM KNO_3 and the *cis* compartment 0.1 mM Prussian Blue only. Feedback curves were obtained with the tap closed and then at 5 minute intervals after the tap was opened up to 30 minutes. Immediately before each feedback measurement a dip sample of the *cis* compartment electrolyte was obtained from the inter-compartment aperture region. The measurements were repeated with the *trans* compartment electrolyte substituted with 0.1 mM Prussian Blue / 10 mM $TlNO_3$. Data were also collected for gAN and control samples in both electrolyte compositions.

5.2.3.3 *UV spectra of Prussian Blue dip samples*

UV-visible spectroscopy was used to monitor the absorbance of the membrane surface PB electrolyte in the upper compartment of the cell. Samples were obtained by removing small (~ 0.5 ml) aliquots of electrolyte at regular time intervals throughout the

feedback curve experiments. The samples were then diluted to twice their original volume with high purity water.

Spectra were obtained using a Pharmacia Biotech Ultraspec 4000 UV-visible spectrophotometer and quartz cuvettes. The UV absorbance of the sample was measured over a wavelength range of 200 - 800 nm.

5.3 Results and discussion

5.3.1 *Experiments using K_3FeCN_6 electrolyte*

5.3.1.1 *Determination of the potential-dependent behaviour of gA and gAN channels by SECM feedback curve experiments*

In KCl supporting electrolyte the sample treated with gA displays positive feedback, indicative of conducting properties, in the tip potential range -1.0 → 0.8 V. At tip potentials of 0.8 → 1.0 V the sample displays negative feedback, which is characteristic of insulating properties. In $N(CH_3)_4Cl$ supporting electrolyte, a cation with known channel-blocking characteristics, the gA channel displays the negative feedback 'closed' state over a much wider potential range, from -0.7 V → 1.0 V, indicating channel occlusion by the $(CH_3)_4N^+$ ion. The transition from conducting to insulating behaviour in each supporting electrolyte is shown in Figure 35.

Figure 35. *Feedback curves of gA membranes in 0.1 mM $K_3Fe(CN)_6$ and either 100 mM KCl or 100 mM $N(CH_3)_4Cl$ supporting electrolyte.*

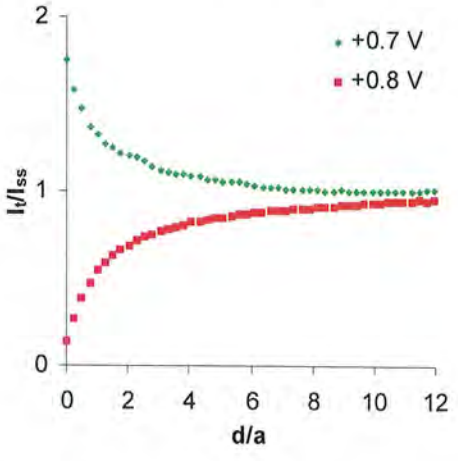

(a) In 0.1 mM $K_3Fe(CN)_6$ / 100 mM KCl.

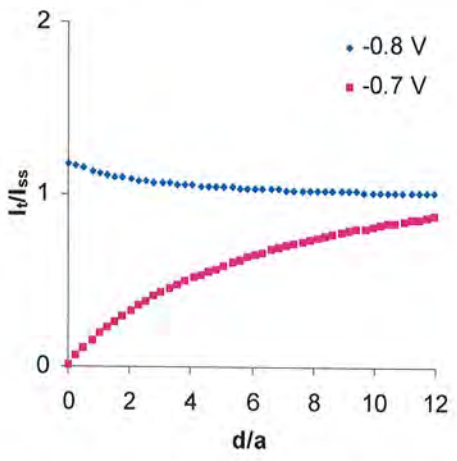

(b) In 0.1 mM $K_3Fe(CN)_6$ / 100 mM $N(CH_3)_4Cl$.

In KCl supporting electrolyte the sample treated with gAN displays positive feedback with an applied tip potential between -1.0 → -0.52 V. At potentials higher (less negative) than -0.52 V the tip current shows sudden decrease and negative feedback is observed in the region -0.51 → 1.0 V. This transition between conducting and insulating behaviour, an apparent potential-dependent switch like process, is shown in more detail in Figure 38. When $N(CH_3)_4Cl$ supporting electrolyte is used positive feedback is observed between -1.0 V → -0.8 V and negative feedback is observed between -0.7 V → 1.0 V. This data suggests, just as expected, that the membrane displays insulating behaviour over a much larger potential range in the $N(CH_3)_4Cl$ case than in the KCl case. The transition from conducting to insulating behaviour in each supporting electrolyte is shown in Figure 36.

Figure 36. *Feedback curves of gAN membranes in 0.1 mM $K_3Fe(CN)_6$ and either 100 mM KCl or 100 mM $N(CH_3)_4Cl$ supporting electrolyte.*

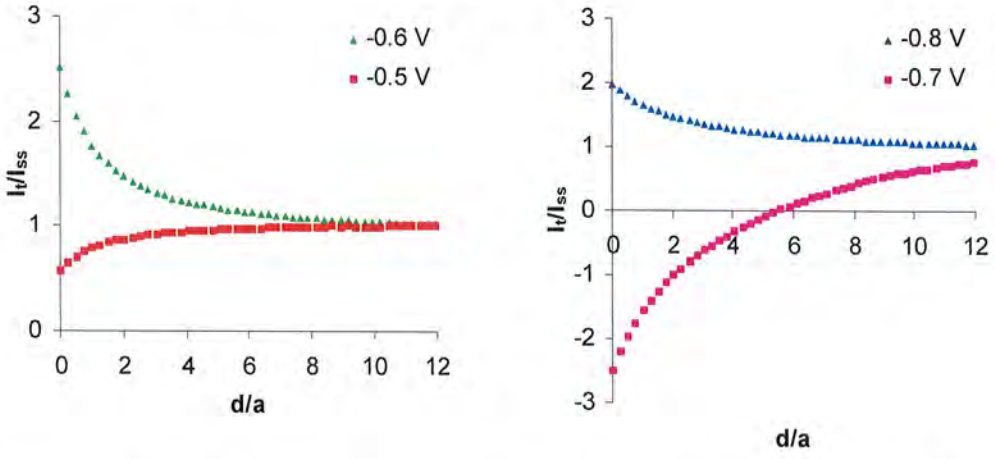

(a) In 0.1 mM $K_3Fe(CN)_6$ / 100 mM KCl.

(b) In 0.1 mM $K_3Fe(CN)_6$ / 100 mM $N(Me)_4Cl$.

In both KCl and $N(CH_3)_4Cl$ supporting electrolytes the control sample, treated with methanol in the absence of peptide, displays almost identical positive feedback with a tip potential between -1.0 → -0.9 V and negative feedback with a tip potential -0.9 → 1.0 V. The transition from conducting to insulating behaviour in each supporting electrolyte is shown in Figure 37.

Figure 37. *Feedback curves of control membranes in 0.1 mM $K_3Fe(CN)_6$ and either 100 mM KCl or 100 mM $N(CH_3)_4Cl$ supporting electrolyte.*

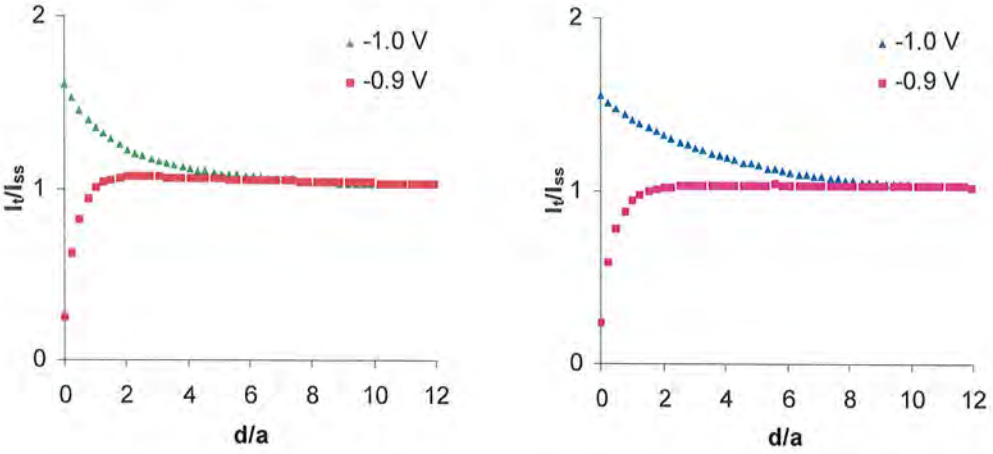

(a) In 0.1 mM $K_3Fe(CN)_6$ / 100 mM KCl. *(b) In 0.1 mM $K_3Fe(CN)_6$ / 100 mM $N(CH_3)_4Cl$.*

The slight positive feedback displayed by the controls at very negative potential (~ -1.0 V) can be explained in terms of an ionic 'leakage' current arising from electroporation of the membrane.

A profile of the tip current at the membrane surface ($z \rightarrow 0$, but not touching the membrane) shows that the behaviour of the gA channel is potential independent within experimental error, whereas the gAN channel displays a clear potential dependency highlighted by the sharp current change at -0.515 ± 0.005 V. The potential of this sharp change in channel current, referred to as the '*switching potential*' from here on in, is the potential at which the nicotinamide moiety is fully reduced allowing the channels to open. At potentials higher (more positive) than the switching potential the channel is occluded by the oxidised pendant nicotinamide moiety in a *ball and chain* fashion. This observation is supported by the chronoamperometric experiments (*vide supra*) discussed in Chapter 6.

Feedback curves at different tip potentials, but otherwise under the same experimental conditions as above are shown in Appendix 1. These data are not included here because they relate to the potential range away from the gAN channel switching.

Figure 38. *Comparison of gA and gAN membrane currents.*

Plots of the tip current at a height $z \rightarrow 0$ above the membrane surface. In the case of gAN a definite current step is observed between -0.52 and -0.51 V corresponding to the oxidation of the nicotinamide moiety and 'ball and chain' occlusion of the channel entrance. In the case of gA, absent of the tethered nicotinamide moiety, the current is approximately independent of the tip potential over the potential range studied.

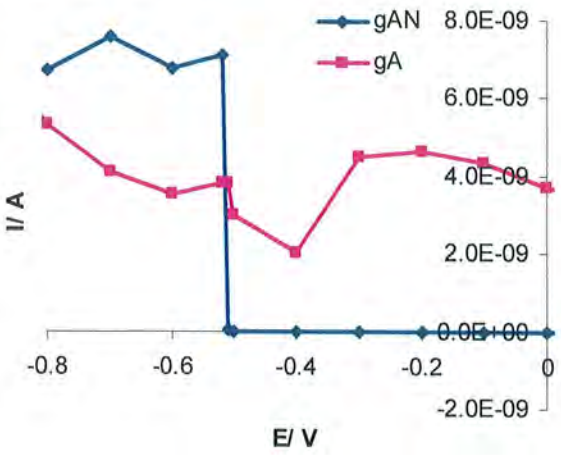

Cyclic voltammetry was also attempted in an effort to confirm the apparent switching potential of the gAN channel (Figure 39). In the case of gAN it was expected that oxidation and reduction peaks would present at ~ -0.515 V. Unfortunately, as Figure 39 shows, there are no obvious signs of heterogeneous ET in this region of the voltammogram. During these CV experiments there was noticeable fouling of the electrode surface, which gives rise to the possibility that the gAN redox peaks are in fact present but are masked by a very slow rate of heterogeneous ET. Further experiments will be needed to clarify these data.

Figure 39. *Attempted CVs of gA and gAN.*

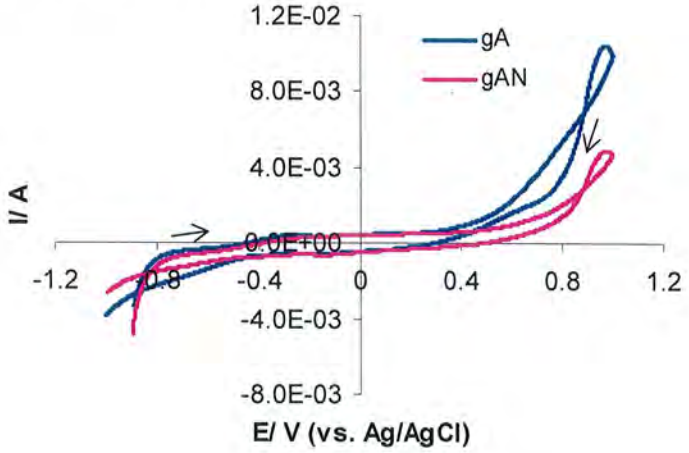

5.3.1.2 *Area scan experiments*

Area scans of platinum wire and ribbon were obtained in constant height mode in a 0.1 mM $K_3Fe(CN)_6$ / 100 mM KCl electrolyte with a tip bias of 0.6 V. The current profiles

are shown in Figure 40 where regions of high current are shown in red and regions of low current in blue. The tip was moved across the target substrate at 1 μms^{-1} and the tip current recorded as a function of lateral position relative to the starting point. When the tip was in close proximity to the underlying platinum target, as was the case when it encountered an upward substrate projection, an amplification of the current and positive feedback was observed due to tip-substrate-mediated regeneration of the ferri / ferrocyanide at the tip surface. The current profiles clearly display positive feedback in a cross-sectional wire shape (Figure 40(a)) and positive feedback due to the upwardly projecting ridges in the ribbon surface (Figure 40(b)).

Figure 40. *Area scans of platinum wire and ribbon.*

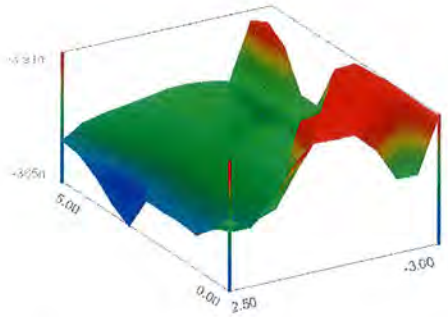

(a) Platinum wire scanned in constant height mode in 0.1 mM $K_3Fe(CN)_6$ / 100 mM KCl at tip potential 0.6 V.

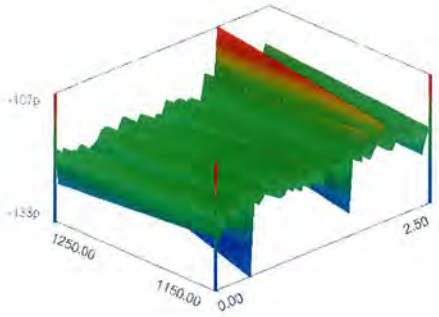

(b) Platinum ribbon scanned in constant height mode in 0.1 mM $K_3Fe(CN)_6$ / 100 mM KCl at tip potential 0.6 V.

In order to further examine the behaviour of the membrane at very negative potential, in the region where the positive feedback curves were observed, area scans was obtained at -0.8 V in 0.1 mM $K_3Fe(CN)_6$ / 100 mM KCl electrolyte. The scan shows high current peaks which, given their magnitude and random distribution, imply they originate from electroporation of the supported BLM. This is corroborated by the observation that a similar scan performed at a tip potential of 0.1 V displayed a perfectly uniform insulating surface with no evidence of poration.

Figure 41. *Area scans of porated and non-porated control membranes.*

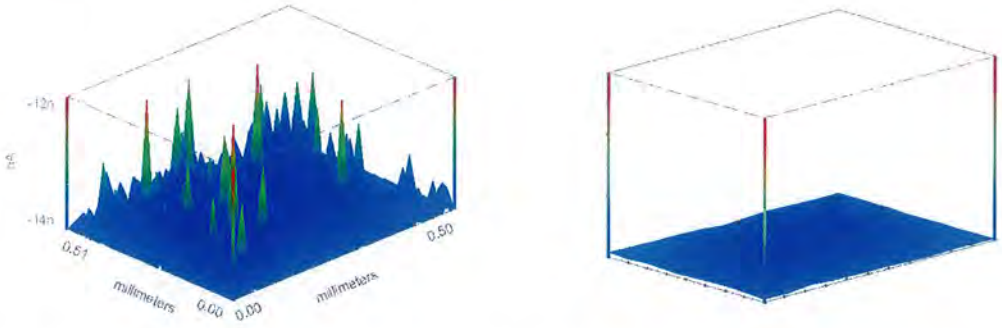

(a) Electroporated control membrane. Scan performed in fixed height mode in 0.1 mM $K_3Fe(CN)_6$ / 100 mM KCl at tip potential -0.8 V.

(b) Non-porated control membrane. Scan performed in fixed height mode in 0.1 mM $K_3Fe(CN)_6$ / 100 mM KCl at tip potential 0.1 V.

Using the same methodology attempts were also made to obtain area scan images of gA / gAN channels at around the switching potential. Unfortunately the lateral resolution of these area scan attempts was insufficient to observe the membrane inserted channels.

5.3.1.3 *The effect of temperature and pH on gAN switching potential*

Further investigations were performed with gAN treated membranes to determine the effect, if any, of electrolyte pH (Figure 42(a)) and temperature (Figure 42(b)) on the switching potential of the synthetic channel. Under conditions of physiological pH the switching potential of nicotinamide moiety tends towards a higher (less negative) value signifying increasing ease of oxidation with increased proton concentration. The voltage switch appears to be independent of temperature at the range of temperatures studied (0 – 50 °C).

Figure 42. *Switching potential variation of gAN with pH and temperature.*

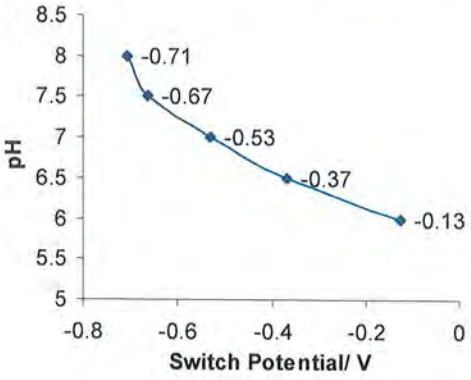

(a) Variation of gAN switching potential with pH. A range of physiological pH phosphate buffers were used as the supporting electrolyte.

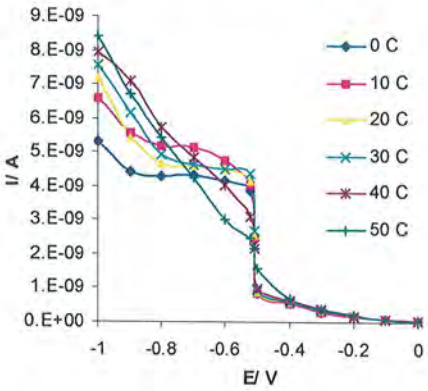

(b) Variation of gAN switching potential with temperature. Measurements were performed in pH 7.0 phosphate buffer as supporting electrolyte..

5.3.2 *Experiments using Prussian Blue electrolyte*

5.3.2.1 *Monitoring thallous ion transport with Prussian Blue as an indicator*

The variation of membrane surface normalised current (I_t/I_{ss} at $z \rightarrow 0$) with time is shown for K^+ (Figure 43(a)) and Tl^+ (Figure 43(b)) transmembrane concentration gradients below. The permeant cation electrolyte was placed in the *trans* compartment beneath the membrane. As the WE was positioned within 10 μm of the *cis* membrane surface, permeant ions diffused towards the WE when the cell inter-compartment tap was opened.

Figure 43. *Variation of surface ($z \rightarrow 0$) normalised current with permeation time. Tip potential -0.6 V.*

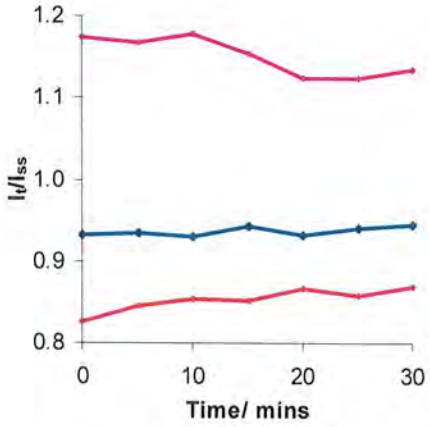

(a) Lower compartment = 0.1 mM PB / 10 mM KNO_3; Upper compartment = 0.1 mM PB only.

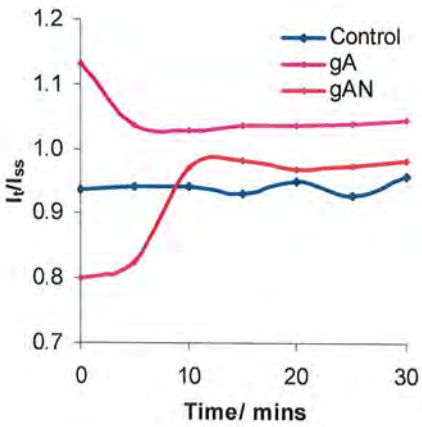

(b) Lower compartment = 0.1 mM PB / 10 mM $TlNO_3$; Upper compartment = 0.1 mM PB only.

Figure 43(a) shows that in the K^+ concentration gradient the normalised current of the gA treated membrane gradually decreases with time and that of the gAN treated membrane gradually increases with time. The gA current behaviour in this respect can be explained in terms of the equilibration of the ionic concentration of the two compartments with time. The rate of diffusion of K^+ ions through the gA channels decreases as equilibration is achieved, resulting in a decrease in current. The opposite trend in gAN current behaviour is unexpected given the transmembrane ionic concentration gradient is exactly the same as in the gA case. The only difference between the two channel types is the inclusion of the nicotinamide group at the C-terminal ends of the gAN channel dimer. This suggests some interaction between the gAN nicotinamide group and PB.

Figure 43(b) shows that the gA and gAN membranes in the Tl^+ concentration gradient behave in much the same manner as those in the K^+ gradient. The only notable difference is that the surface normalised current appears to reach a constant value much quicker with the passage of Tl^+.

In both cases the surface normalised current of the control membrane remains approximately the same with time, confirming negligible ion permeation in the absence of peptide channels. The steady current also suggests that there is minimal ion leakage through the membrane when the tip potential is applied.

The variation of membrane surface electrolyte UV absorbance with time is shown for K^+ (Figure 44(a)) and Tl^+ (Figure 44(b)) transmembrane concentration gradients below. Electrolyte samples were taken from the *cis* compartment membrane region at regular time intervals before (tap closed) and after (tap open) the concentration gradient was applied.

Figure 44. *UV absorbance of surface ($z \rightarrow 0$) electrolyte at different permeation times. Tip potential -0.6 V.*

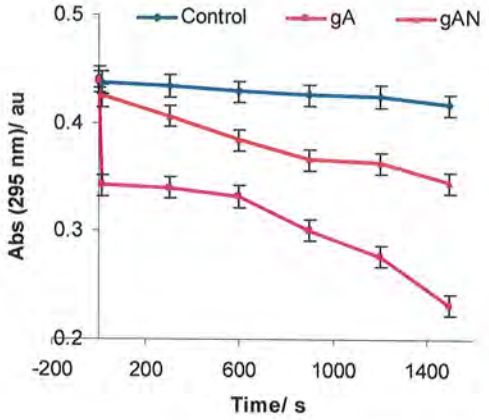

(a) *Lower compartment = 0.1 mM PB / 10 mM KNO_3; Upper compartment = 0.1 mM PB only.*

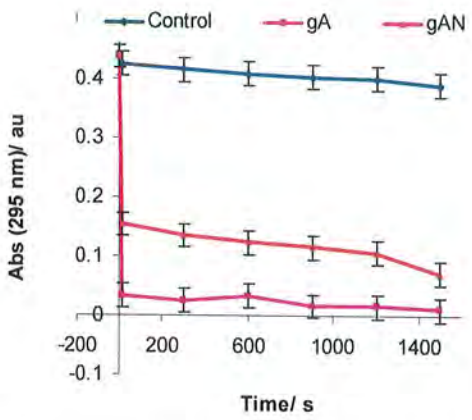

(b) *Lower compartment = 0.1 mM PB / 10 mM $TlNO_3$; Upper compartment = 0.1 mM PB only.*

In the case of the K^+ concentration gradient (Figure 44(a)) the electrolyte on the sampled side of the gA treated membrane shows a rapid decrease in absorbance the moment the tap is opened. This observation is due to K^+ ions diffusing up through the gA channels and interacting with PB at the upper face of the membrane. The presence of K^+ ions combined with the negative WE potential (-0.6 V) results in the formation of the less intensely coloured Everitt's Salt (ES). With time, as the K^+ concentration in the opposite cell compartment equalises, the rate of K^+ diffusion, ES formation and change in absorbance all decrease. The gAN membrane displays much the same behaviour, although the rate of ES formation is less than in the gA case due to temporary steric occlusion of the channel by the tethered nicotinamide moiety.

In the Tl^+ gradient the sampled electrolyte displayed a much quicker decrease in absorbance as the ions were allowed to flow. The change in absorbance also levelled off much quicker than in the K^+ case implying favourable and irreversible formation of the corresponding ES.

5.4 References

1. B. Bechinger, *Curr. Opin. Chem. Biol.*, 2000, **4**, 639
2. J. M. Sanderson and S. Yazdani. *Chem. Commun.*, 2002, **10**, 1154
3. D. J. Tobias, *Curr. Opin. Struct. Biol.*, 2001, **11**, 253
4. Y. N. Antonenko, P. Pohl and G. A. Denisov, *Biophys. J.*, 1997, **72**, 2187
5. Y. N. Antonenko and A. A. Bulychev, *Biochim. Biophys. Acta*, 1991, **1070**, 474

6. P. Pohl, S. M. Saparov and Y. N. Antonenko, *Biophys. J.*, 1998, **75**, 1403
7. A. J. Bard and M. V. Mirkin, editors, *Scanning Electrochemical Microscopy*, Marcel Dekker Inc., New York, 2001
8. S. Amemiya, Z. Ding, J. Zhou and A. J. Bard, *J. Electroanal. Chem.*, 2000, **483**, 7
9. J. Zhang and P. R. Unwin, *Langmuir*, 2002, **18**, 2313
10. S. Amemiya and A. J. Bard, *Anal. Chem.*, 2000, **72**, 4940
11. C. Wei, A. J. Bard and M. V. Mirkin, *J. Phys. Chem.*, 1995, **99**, 16033
12. M. -H. Delville, M. Tsionsky and A. J. Bard, *Langmuir*, 1998, **14**, 2774
13. M. Tsionsky, A. J. Bard and M. V. Mirkin, *J. Am. Chem. Soc.*, 1997, **119**, 10785
14. J. Mauzeroll, M. Buda, A. J. Bard, F. Prieto and M. Reuda, *Langmuir*, 2002, **18**, 9453
15. J. P. Wilburn, D. W. Wright and D. E. Cliffel, *Analyst*, 2006, **131**, 311
16. H. T. Tien and E. A. Dawidowics, J. Colloid Interface Sci., 1966, 22, 438
17. D. P. Tieleman, H. J. C. Berendsen and M. S. P. Sansom, *Biophys. J.*, 2001, **80**, 331
18. V. P. Ivanova, I. M. Makarov, T. E. Schaffery and T. Heimburg, *Biophys. J.*, 2003, **84**, 2427
19. G. Favero, A. D'Annibale, L. Campanella, R. Santucci and T. Ferri, *Anal. Chim. Acta*, 2002, **460**, 23
20. S. Ulmeanu, H. J. Lee, D. J. Fermin, H. H. Girault and Y. Shao, *Electrochem. Commun.*, 2001, **3**, 219
21. Z. Samec, E. Samcová and H. H. Girault, *Talanta*, 2004, **63**, 21
22. T. Matsue, H. Shiku, Y. Yamada and I. Uchida, *J. Phys. Chem.*, 1994, **98**, 11001
23. F. Herren, P. Fisher, A. Ludi and W. Haig, *Inorg. Chem.*, 1980, **19**, 956
24. A. Dostal, G. Kauschka, S. J. Reddy and F. Scholz, *J. Electroanal. Chem.*, 1996, **406**, 155
25. M. B. Robin, *Inorg. Chem.*, 1962, **1**, 337
26. C. Whitehouse, D. Gidalevitz, M. Cahuzac, R. E. Koeppe II and A. Nelson, *Langmuir*, 2004, **20**, 9291
27. R. D. Shannon, *Acta Cryst.*, 1976, **A32**, 751

Chapter 6

Chronoamperometry and Voltammetry

6.1 Introduction

6.1.1 *Monitoring the passage of ions across gramicidin channels*

Chronoamperometry is a convenient method of monitoring the passage of electroactive ions across transmembrane peptide channels at the electrode surface. Nelson and co-workers have previously used chronoamperometry and cyclic voltammetry to study the reduction of Tl^+ at gA-treated DOPC-coated mercury electrodes.[1,2] The Tl(I) / Tl(Hg) reduction process is known to occur very rapidly at uncoated mercury electrodes[3] meaning the rate limiting step is the diffusion of Tl^+ through the gA channel in the system studied. In these experiments chronoamperometry was performed by applying potential steps in the potential range and more negative of the Tl(I) / Tl(Hg) redox process. The resulting current-time plots showed two distinct regions – the first of which, an exponential current decay, was attributed to inactivation of the monomer channel conduction and the second region, a current *quasi*-steady-state, was due to diffusion of ions to the surface reaction. Normalised current-potential plots demonstrate a linear relationship between Tl^+ permeation and gA concentration and show that, in contrast to the behaviour of the Tl^+ permeant ion, Cd^{2+} ions are unable to pass across the gA channel. At potentials more negative than -0.7 V the membrane becomes non-selectively permeable due to an increase in structural defects. It was also reported that incorporation of aromatic or conjugated compounds into the DOPC monolayer caused an increase in the reduction current by decreasing the rate of channel inactivation and increasing their stability.

The permeation of Tl^+ ions through gA half channels has been further studied by Mauzeroll and co-workers.[4] In their experiments they prepared DOPC monolayers at the surface of an HMDE which was preloaded with thallium. The lipid coated HMDE acted as substrate in a substrate-generation tip-collection (SG-TC) mode SECM experiment. When positively biased, so as to oxidise the HMDE-borne Tl^0 to Tl^+, the untreated monolayer displayed negligible voltammetric response indicating uniformity and completeness of surface lipid coverage. Conversely, treatment of the lipid substrate with gA resulted in an increase in voltammetric response due to Tl^+ collection at the SECM tip, clearly indicating the passage of ions from the HMDE across the DOPC monolayer.

The UME collection tip current for Tl^+ generated at the HMDE that diffuses through the gA half channels is given by:

$$i_t = 4nFDC_0(b,t)a \qquad (73)$$

where i_t is the tip current, n the number of electrons, a the tip radius and D the diffusion coefficient. In this case $C_0(b,t)$ represents the concentration gradient of Tl^+ at the electrode surface. $C_0(b,t)$ is a complicated Laplace transformation dependent on the apparent heterogeneous rate constant (k_{het}) for the transport of Tl^+ through the gA half channels. Calculation of $C_0(b,t)$ gave a k_{het} value of 2.8 ($\pm$ 0.1) $\times$ 10^{-4} cms^{-1}. Heterogeneous electrode kinetics like those exhibited by the reaction of Tl^+ at the electrode surface are considered further below.

6.1.2 *Heterogeneous electrode kinetics*

The rate of heterogeneous electron transfer is a fundamental issue of electrochemistry. In the late 1950s Rudolph A. Marcus, winner of the 1992 Nobel Prize for Chemistry,[5] developed a theory to account for outer sphere electron transfer.[6,7] Marcus' work has subsequently been extended to inner sphere electron transfer by Noel Hush and further refined to take into consideration heterogeneous electron transfer.[8,9] Marcus suggested the following expression for the theoretical calculation of k^o in a heterogeneous electron transfer process:

$$k^o = k_{el} Z_{het} \exp\left(-\frac{\Delta G^*}{k_B T}\right) \qquad (74)$$

Where $k_{el} = 1$ for an adiabatic process (where there is no loss or gain of heat), Z_{het} is the collision frequency of a reactant molecule on the electrode surface, ΔG^* is the free energy of activation for the forward electron transfer and the other symbols have their usual significance. The value of Z_{het} is obtained from:

$$Z_{het} = \sqrt{\left(\frac{k_B T}{2\pi m}\right)} = \sqrt{\left(\frac{RT}{2\pi m N_L}\right)} = \sqrt{\left(\frac{RT}{2\pi M}\right)} \qquad (75)$$

Where N_L is Avogadro's number, m and M are the reduced and molecular mass of the reacting species. The value of ΔG^* is obtained from:

$$\Delta G^* = w^O + \left(\frac{\left(\lambda + w^R - w^O\right)^2}{4\lambda} \right) \qquad (76)$$

Where w^O and w^R represent the work required to transport oxidised and reduced species, respectively, from bulk solution to the reaction site. The term λ represent the reorganisation energy, which is composed of the inner (λ_i) and outer (λ_o) components as follows:

$$\lambda = \lambda_i + \lambda_o \qquad (77)$$

The values of λ_o can be obtained from the following equation:

$$\lambda_o = \left(\frac{e^2 N_L}{8\pi\varepsilon_0} \right) g(r \cdot R_e) \left(\frac{1}{n^2} - \frac{1}{\varepsilon_s} \right) \qquad (78)$$

Where r is the radius of the reactant molecule, R_e the distance from the centre of the molecule to the electrode surface, N_L is Avogadro's constant, g the intrinsic barrier term, ε_0 the permittivity of free space, n the refractive index and ε_s the static dielectric constant of the solvent.

Although Marcus' equations give a thorough evaluation of k^o they can not conveniently be applied directly to CV. Several investigations have sought to relate the CV peak potentials, the separation of which depends on the reaction rate, to the heterogeneous rate constant, k^o. Early polarography and CV investigations by Nicholson proposed a direct relationship between a function ψ (which depends on the CV peak separation) and the rate constant, k^o:[10,11]

$$\psi = \frac{k^o}{\sqrt{(\pi a D)}} \qquad (79)$$

$$a = \frac{nF\nu}{RT} \qquad (80)$$

Eisner's method also provides a comparatively simple method of evaluating k^o from CV data:[12]

$$\log k^o = -0.48\alpha + 0.52 + \log\sqrt{\left(\frac{nF\alpha vD}{2.303RT}\right)} \qquad (81)$$

One of the most recent methods of evaluating k^o is that of Kochi who reported the following expression:[13]

$$k^o = 2.18\sqrt{\left(\frac{\alpha vnFD}{RT}\right)}exp\left(-\frac{\alpha^2 nF\Delta E_p}{RT}\right) \qquad (82)$$

Where α is the dimensionless transfer coefficient, n is the number of electrons transferred, v is the scan rate, ΔE_p is the peak separation, D is the diffusion coefficient in cm^2s^{-1} and the other symbols have their usual significance.

6.1.3 *The relationship between homo- and heterogeneous electron-transfer in solution*

Marcus proposed[14,15] that for an $ML_n^{(z+1)+/z+}$ couple (like $Fe(CN)_6^{3-}/Fe(CN)_6^{4-}$) the free energy of activation of the heterogeneous electron-transfer, ΔG_{el}^*, should be approximately half that of the corresponding bimolecular homogeneous electron-transfer, ΔG_{ex}^*. In the case of an adiabatic outer-sphere mechanism the free energies of activation, ΔG_i^*, are given by the following equation:

$$k_i = Z_i exp\left(-\frac{\Delta G_i^*}{RT}\right) \qquad (83)$$

Where k_i is the rate constant of the electron-transfer process and Z_i is the pre-exponential factor.

Given that $\Delta G_{el}^* \sim \frac{1}{2}\Delta G_{ex}^*$ then:

$$\frac{k_{el}}{Z_{el}} = \left(\frac{k_{ex}}{Z_{ex}}\right)^{1/2} \qquad (84)$$

Unfortunately the pre-exponential factor values Z_{el} and Z_{ex} have different dimensions and are not clearly definable, meaning equation 84 is difficult to test experimentally. Yu and Swaddle have used AC voltammetry to observe the effect of pressure on the volumes of activation, ΔV_{el} and ΔV_{ex}, of the hetero- and homogeneous processes respectively.[16] The value of ΔV_i at constant temperature is given by:

$$\Delta V_i = -RT\left(\frac{\partial \ln k_i}{\partial P}\right)_T \qquad (85)$$

If Z_{el} and Z_{ex} are assumed to be independent of pressure, then given equation 85 it should also be true that:

$$\Delta V_{el} \approx \tfrac{1}{2}\Delta V_{ex} \qquad (86)$$

The volumes of activation can therefore be used as a convenient means of observing the relative magnitudes of Z_{el} and Z_{ex} and testing the accuracy of Marcus' predictions. AC voltammograms were obtained over a pressure range up to 200 MPa for several common redox couples. Values of k_{el} obtained from equation 85 were converted to the corresponding ΔV_{el} values, which were then compared to previously calculated ΔV_{ex} values.

$$[\cot\phi]_{max} = 1 + \left(\frac{\left(2{D_O}^{\beta}{D_R}^{\alpha}\omega\right)^{1/2}}{\left(\alpha^{-\alpha}\beta^{-\beta}k_{el}\right)}\right) \qquad (87)$$

Where ϕ is the phase angle, D_O and D_R the diffusion coefficients of the oxidised and reduced species respectively, α and β the transfer coefficients for the reduction and oxidation processes respectively and $\omega = 2\pi f$. Note that $\beta = 1 - \alpha$.

The data obtained showed a good correlation between ΔV_{el} and ΔV_{ex}, the latter being approximately twice as large for each of the couples investigated, leading to the

relationship being termed the '*fifty percent rule*'. Subsequent work by Fu and Swaddle has applied this method to a wide range of common organometallate redox couples.[17,18]

6.1.4 *The influence of supporting electrolyte on the $Fe(CN)_6^{3-}/Fe(CN)_6^{4-}$ couple*

Voltammetry of the $Fe(CN)_6^{3-}/Fe(CN)_6^{4-}$ couple with carbon microelectrodes in the absence of KCl supporting electrolyte shows complete suppression of the reduction process. This suppression was attributed to the '*dynamic diffuse layer effect*' in which transport of the charged reactants across the diffuse part of the electrolyte double layer limits their rate of reduction.[19] The influence of ion pair formation between the $Fe(CN)_6^{3-}/Fe(CN)_6^{4-}$ couple and supporting electrolyte alkali metal cations on the rate and mechanism of electron transfer has also been investigated.[20,21]

Using microelectrodes and the current impulse method Peter and co-workers[21] demonstrated that the rate of the $Fe(CN)_6^{3-}/Fe(CN)_6^{4-}$ redox process showed first order dependence on the concentration of supporting electrolyte cation. They showed that the catalytic influence of the supporting electrolyte cation increases in the order $Li^+ < Na^+ < K^+ \sim Cs^+$. The apparent anodic exchange current density, i_a^o, of a simple electrode process can be written as:

$$i_a^o = nFk_a^o\left(\gamma_O^{1-\alpha}\gamma_R^{\alpha}/\gamma^*\right)C_O^{1-\alpha}C_R^{\alpha} \qquad (88)$$

Where k_a^o is the apparent rate constant, C_O, C_R and γ_O, γ_R are the concentrations and activity coefficients of the oxidised and reduced species respectively, α is the transfer coefficient and γ^* is the activity coefficient of the activated (transition state) complex. A special case arises where $C_O = C_R = C_E$, where C_E is the concentration of the electroactive species if the term $\gamma_O^{1-\alpha}\gamma_R^{\alpha}/\gamma^*$ is independent of C_E:

$$i_a^o = nFk_a^o\left(\gamma_O^{1-\alpha}\gamma_R^{\alpha}/\gamma^*\right)C_E \qquad (89)$$

According the equation 89 a linear dependence of i_a^o on C_E should be observed if C_E is independent of $\gamma_O^{1-\alpha}\gamma_R^{\alpha}/\gamma^*$, however, deviation from linearity was observed when the concentration of hexacyanoferrate ions was changed in a KCl background electrolyte.

This unexpected observation caused Peter and co-workers to refine the equation for an experimental rate constant, k^o_{exp}, to simply the following:

$$k^o_{exp} = \frac{i^o_{exp}}{nFC_E} \qquad (90)$$

This refinement takes into account that in very dilute solutions $\gamma \rightarrow 0$ and that $\alpha \sim 0.5$. The changes in k^o_{exp} brought about by varying the nature and concentration of the supporting electrolyte were large enough to justify the use of this approximation for the purposes of comparison. The first order relationship between rate constant and electrolyte concentration was later corroborated by Campbell and Peter, who used AC impedance spectroscopy to observe the effect of K^+ concentration on the heterogeneous rate constant of the $Fe(CN)_6^{3-}/Fe(CN)_6^{4-}$ couple.[22]

Beriet and Pletcher carried out a cyclic voltammetry investigation of the $Fe(CN)_6^{3-}/Fe(CN)_6^{4-}$ couple using platinum microelectrodes.[23] It showed that the formal potential shifted to a more positive value with increasing electrolyte concentration. This potential shift was attributed to greater interaction between the supporting electrolyte cation and Fe^{2+} form over the Fe^{3+} form. Beriet and Pletcher also observed that inclusion of Sr^{2+} in the supporting electrolyte resulted in the potential shift being even more pronounced than in the case of the monovalent cations. This observation implies that divalent cations interact with the Fe^{2+} form much more than monovalent cations do. From their observations they were able to slightly revise the catalytic trend proposed by Peter and co-workers which was mentioned earlier. For a given concentration of supporting electrolyte the $Fe(CN)_6^{3-}/Fe(CN)_6^{4-}$ rate constant occurs in the order of $Li^+ < Na^+ < K^+ < Sr^{2+}$. Furthermore it was observed that when the rate constant and electrolyte concentration were low it was difficult to obtain reproducible voltammetric results. It was suggested that low concentrations of supporting electrolyte meant there were insufficient cations to associate with the highly charged $Fe(CN)_6^{3-}/Fe(CN)_6^{4-}$ ions thereby inhibiting their decomposition at the electrode surface. As a consequence of this $Fe(CN)_6^{3-}/Fe(CN)_6^{4-}$ ions became adsorbed to the electrode surface in low concentration electrolyte.

6.1.5 *Summary of Chapter 6*

In this chapter the reproducibility of the gAN potential-dependent switching behaviour, commented on in the SECM experiments of Chapter 5, was tested by observing the current response to successive potential pulses in chronoamperometry. By analogy to the work of Nelson, Mauzeroll and co-workers cyclic voltammetry was used to test the permeation of Tl^+ and Eu^{3+} across peptide ion channels. Unlike previous work that utilised HMDE-supported lipid monolayers this investigation involved the preparation of supported BLM directly on a gold electrode surface. The supported lipid bilayer was then treated with the channel forming peptides gA or gAN and cyclic voltammetry performed in a range of electrolyte solutions containing $K_3Fe(CN)_6$, $TlNO_3$, $Eu(NO_3)_3$ and KNO_3. Finally, cyclic voltammetry was used to observe the influence of a wide range of supporting electrolyte cations on the transfer coefficient, diffusion coefficient and heterogeneous rate constants of the $Fe(CN)_6^{3-}/Fe(CN)_6^{4-}$ redox couple.

6.2 **Experimental procedure**

6.2.1 *Apparatus*

CA, DP and slow scan CV data were collected using a PG 580 potentiostat (Uniscan Instruments, Buxton, UK) and associated software. Fast scan CV was performed using a Potentiostat-Galvanostat Model 283 (Princeton Applied Research, Oak Ridge, US) connected to an Amel 7805 High Speed Wave Generator (Amel, Milan, Italy) via the external input.

A self-fabricated 10 ml glass cell was used. The RE was an aqueous Ag/AgCl electrode (Bioanalytical Systems, West Lafayette, US) and the CE was a self-fabricated 1 cm^2 platinum flag. The working electrode was either a 1.6 mm gold or platinum electrode (Bioanalytical Systems, West Lafayette, US) or a 10 μm platinum UME (CH Instruments Ltd., Austin, US) depending on the experiment.

6.2.2 *Chronoamperometric measurements*

A polycarbonate membrane was secured over a 1.6 mm diameter platinum electrode (Bioanalytical Systems, US) with a rubber o-ring. The membrane was positioned so that the polycarbonate was tight to the underlying platinum surface. EPC aqueous suspension prepared as before was painted onto the polycarbonate surface. During EPC application the polycarbonate was smoothed with the brush to prevent air bubbles being

trapped between the platinum and membrane and to ensure a flush seal between the membrane and active electrode surface. The membrane coated electrode was inverted and the EPC allowed to air dry before the electrode was suspended in a solution of 100 µl of 0.12 mM gAN in methanol and 900 µl of high purity water (concentration of gAN = 1.2×10^{-5} M) and refrigerated overnight. The electrode was then immersed in a 100 mM tris buffer (pH 7.0) / 1 mM K_3FeCN_6 solution and CA performed with a sequence of 10 s potential-steps between -0.55 V (t = 0 s) and -0.1 V. The electrolyte solutions were purged with argon for the 5 minutes immediately prior to the chronoamperograms being recorded. A plot of current against time was recorded for each potential-step. Measurements were repeated with identically prepared membrane coated electrodes immersed in tris buffer with $TlNO_3$ and $Eu(NO_3)_3$.

6.2.3 *Cyclic voltammetry of self-assembled BLMs on gold electrodes*

A 1.6 mm diameter gold electrode (Bioanalytical Systems, West Lafayette, US) was immersed in a solution of 20 mg phosphatidylthioethanol (PTE)(Avanti Polar Lipids Inc., Alabaster, US) in 1 ml of chloroform and refrigerated. In order to monitor the formation of the surface thiolated monolayer CVs were performed with the electrode on 1 mM $K_3Fe(CN)_6$ / 100 mM KNO_3 solution. These CVs were performed at 1 hour intervals up to 6 hours, then after 12 and 24 hours of PTE immersion time. The CV of 1 mM $K_3Fe(CN)_6$ / 100 mM KNO_3 at 24 hours was identical to a CV of 100 mM KNO_3 indicating complete coverage of the electrode surface. After coating with PTE monolayer the electrode was rinsed and dried under a stream of nitrogen before being fused with PC vesicles, to form an overall bilayer. This was achieved by immersing the PTE treated electrode in a PC vesicle solution, resulting in vesicle fusion and a mixed-bilayer (PTE lower and PC upper) at the gold surface.

Multilamellar PC vesicles were prepared as follows: PC (10 mg: equivalent to 100 µl of a standard 100 mg in 1 ml chloroform solution) was placed in a 50 ml round bottomed flask and chloroform (1 ml) was added. The mixture was spun on a rotary evaporator for ~ 1 hour until a fine lipid film was deposited on the flask sides. The film was dried under high vacuum for ~ 5 hours to ensure removal of residual organic solvent. The lipid film was hydrated by addition of high purity water (1 ml) to the flask and vortexing for 30 minutes on a test tube shaker. There was no need to size the vesicles since they would burst anyway during fusion with the PTE monolayer.

The gold electrode supporting the mixed-bilayer was immersed in a solution of 100 µl of 0.12 mM peptide stock and 900 µl of high purity water (concentration of peptide ~ 10^{-5} M) and refrigerating for 24 hours prior to use. The peptide stock contained gA or gAN in methanol depending on the channel of interest. Control samples, containing methanol in the absence of peptide, were prepared for comparison.

CVs were performed with the peptide treated mixed-bilayer electrode immersed in three different electrolytes: 1 mM $K_3Fe(CN)_6$ / 100 mM KNO_3, 1 mM $Eu(NO_3)_3$ / 100 mM KNO_3 and 1 mM $TlNO_3$ / 100 mM KNO_3. The electrolyte solutions were purged with argon for the 5 minutes immediately prior to the CVs being recorded. In each CV the WE potential was swept from -1.2 V → 0.5 V and a range of scan rates were used. The CVs of the peptide treated mixed-bilayer electrodes were compared to those of untreated mixed-bilayer.

6.2.4 *Slow scan voltammetry of $K_3Fe(CN)_6$ in monocationic supporting electrolytes*

CVs were performed on various 1 mM $K_3Fe(CN)_6$ / XNO_3 electrolyte solutions, where X^+ = Li^+, Na^+, K^+, Rb^+, Cs^+, NH_4^+, NMe_4^+ and Tl^+. CV measurements were also performed in 1 mM $K_3Fe(CN)_6$ / 100 mM $Eu(NO_3)_3$ electrolyte to observe the affect of the trivalent Eu^{3+} ion on the position and shape of the $Fe(CN)_6^{3-}$ reduction peak. In each CV the WE potential was swept from -1.2 V → 0.5 V and a range of scan rates were used. CVs of the supporting electrolyte in the absence of $K_3Fe(CN)_6$ were also obtained. A 1.6 mm gold electrode (Bioanalytical Systems, West Lafayette, US) was used as the WE. The working and counter electrodes were cleaned thoroughly between each experimental run. This was achieved by soaking in a 3:1 (v/v) mixture of concentrated sulphuric and nitric acids for 2 minutes, rinsing and polishing with fine alumina slurry and then sonicating in high purity water for 2 minutes. The electrolyte solutions were purged with argon for the 5 minutes immediately prior to the CVs being recorded.

DP measurements were performed on the same electrolytes between -0.1 V → 0.5 V with a pulse height of 0.025 V at various scan rates.

6.2.5 *Fast scan voltammetry of $K_3Fe(CN)_6$ in monocationic supporting electrolytes*

CVs were performed on various 1 mM $K_3Fe(CN)_6$ / XNO_3 electrolyte solutions, where X^+ = Li^+, Na^+, K^+, Rb^+, Cs^+, NH_4^+, NMe_4^+ and Tl^+. CV measurements were also

performed in 1 mM $K_3Fe(CN)_6$ / 100 mM $Eu(NO_3)_3$ electrolyte. A 10 μm platinum UME (CH Instruments Ltd., Austin, US) was used as the WE. The electrolyte solutions were purged with argon for the 5 minutes immediately prior to the CVs being recorded. In each CV the WE potential was swept from 0.5 V → -0.1 V at 2 scan rates: 500 Vs^{-1} and 1000 Vs^{-1}. CVs of the supporting electrolyte in the absence of $K_3Fe(CN)_6$ were also obtained.

6.3 **Results and discussion**

6.3.1 *Chronoamperometry of gAN*

The half wave potential, $E_{1/2}$, of gAN at pH 7.0 was measured at -500 mV vs. the saturated calomel electrode (SCE) compared to -560 mV for the NAD^+ / NADH couple.[24] The $E_{1/2}$ for aqueous solutions for the $Fe(CN)_6^{3-}/Fe(CN)_6^{4-}$ couple is approximately 121 mV vs. SCE. At potentials lower than the redox potential of gAN (< 515 mV) the ion-channel should be open. The limit of the potential window is defined by the $E_{1/2}$ of the $Fe(CN)_6^{3-}/Fe(CN)_6^{4-}$ couple and is adequate for our measurements.

Chronoamperometric experiments at which the electrode potential was switched between gAN channel opened (-0.55 V) and channel closed (-0.1 V) potentials (as determined by the SECM feedback experiments detailed in Chapter 5) were performed in the presence of $TlNO_3$, $Eu(NO_3)$ or $K_3Fe(CN)_6$ mediators (Figures 45 and 46).

Figure 45. *Chronoamperometry of a PC supported BLM treated with gAN.*

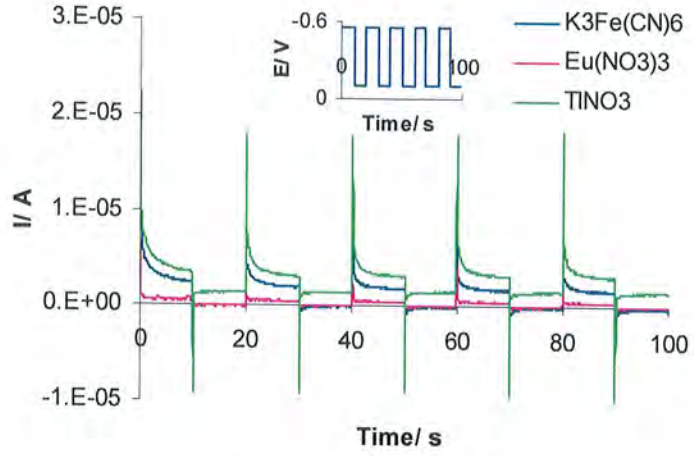

Chronoamperograms obtained by a platinum electrode covered in polycarbonate supported BLM in different electrolytes. The polycarbonate was mounted on the electrode and BLM prepared by the standard brush technique in situ. The BLM was immersed in gAN solution 24 hours prior to use. The electrolyte used was 1 mM in $K_3Fe(CN)_6$, $Eu(NO_3)_3$ or $TlNO_3$ / 100 mM tris buffer (pH 7.0).

Figure 46. *Chronoamperometry of a PC supported BLM untreated with peptide.*

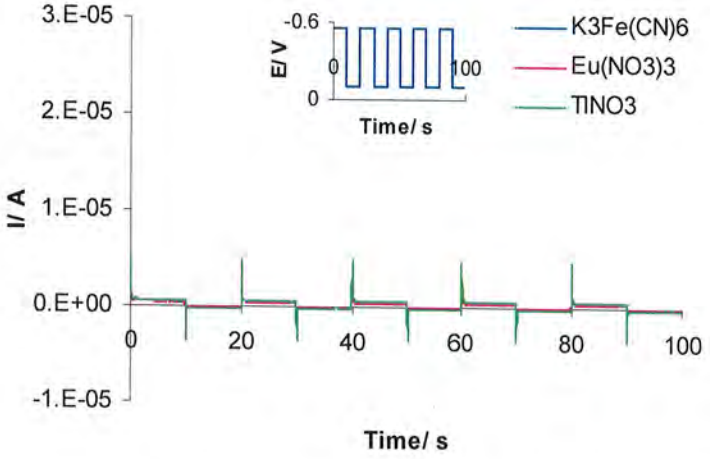

Chronoamperograms obtained by a platinum electrode covered in polycarbonate supported BLM in different electrolytes. The polycarbonate was mounted on the electrode and BLM prepared by the standard brush technique in situ. The BLM was immersed in a 1:10 (v/v) methanol / water (gAN substitute) solution 24 hours prior to use. The electrolyte used was 1 mM in $K_3Fe(CN)_6$, $Eu(NO_3)_3$ or $TlNO_3$ / 100 mM tris buffer (pH 7.0).

The chronoamperograms show a definite, reproducible current response for successive potential steps applied to gAN in the Tl^+- and K^+-containing solutions, although not in the presence of Eu^{3+}. Gramicidin channels are ideally permeable to monovalent alkali

metal cations, however higher valence cations like Eu^{3+} are known to occlude the channel by binding at the mouth.[25] Results obtained with control membranes absent of gAN showed a dramatic current decrease in the potential-step response. Slight leakage currents are evident when the potential switches from one extreme to the other. Identical current behaviour is observed for all three controls, again suggestive of ionic leakage rather than channel mediated ionic migration.

Recall that the current response at a given time during chronoamperometry is given by the Cottrell equation:

$$i(t) = \frac{nFAD_O^{1/2}[O]}{\pi^{1/2}t^{1/2}} \qquad (47)$$

In the case of linear (1-dimensional) diffusion of the electroactive species to the electrode surface a plot of I against $t^{-1/2}$ should result in a straight line. To compliment Figure 45 such a plot was prepared. The plot (Figure 47) shows part-linear part-curved regions for each supporting electrolyte. This suggests that each electroactive ion reaches the electrode surface via a combination of linear and radial diffusion paths. Unfortunately it is not possible to quantify the linear and radial components of the overall diffusion process.

Figure 47. *Cottrell equation plot.*

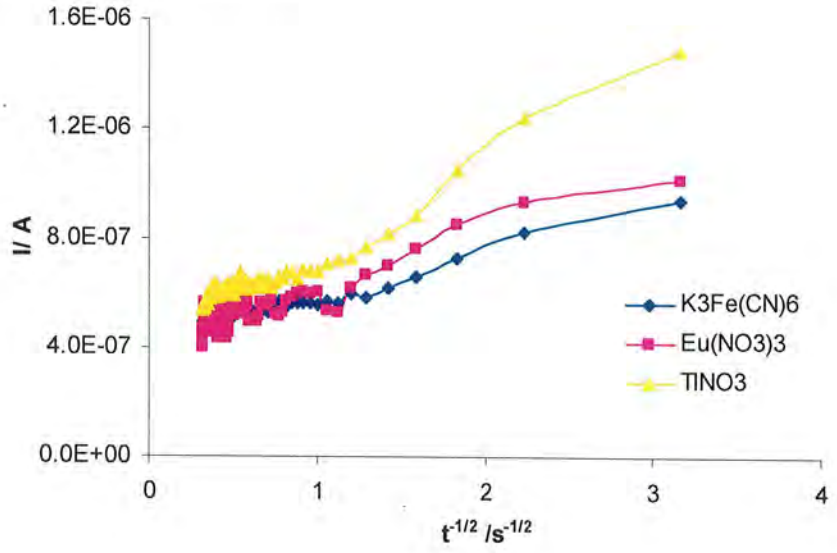

6.3.2 *Voltammetry of gold supported BLMs*

A gold electrode was used as the solid support for BLM construction (Figure 48). The BLM chosen was of mixed layers – PTE was chosen for the surface layer due to the ease of attaching the sulphur terminal group to the gold and PC was chosen as the upper layer for consistency with our SECM experiments. Addition of the PC upper layer was achieved by vesicle fusion.

Figure 48. *Schematic diagram of peptide ion channels inserted into gold-supported BLM.*

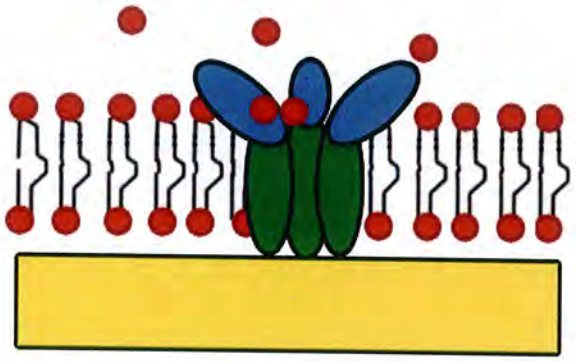

The formation of the lower PTE monolayer was observed by cyclic voltammetry (Figure 49). The non-halide containing KNO_3 was chosen as the supporting electrolyte to overcome the problem of halide ion adsorption to the electrode surface.[26] Complete coverage of the electrode was demonstrated by blockage of $Fe(CN)_6^{3-}$ to the electrode surface: this was achieved after 24 hours immersion in PTE solution (Figure 50).

Figure 49. *BLM formation.*

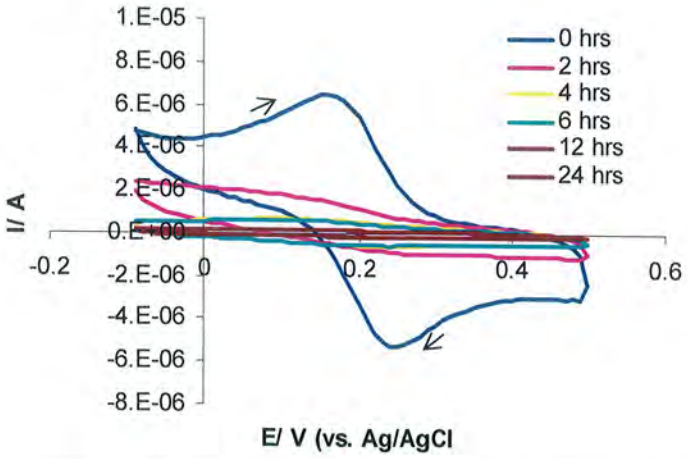

Cyclic voltammograms of 1 mM $K_3Fe(CN)_6$ / 100 mM KNO_3 using a gold electrode treated with PTE for various lengths of time. Scan rate 200 mVs^{-1}. At 0 hours no PTE monolayer has assembled on the gold surface. After 24 hours there is complete coverage demonstrated by $K_3Fe(CN)_6$ being blocked from the electrode surface.

Figure 50. *Complete blockage of $Fe(CN)_6^{4-}$ after 24 hours.*

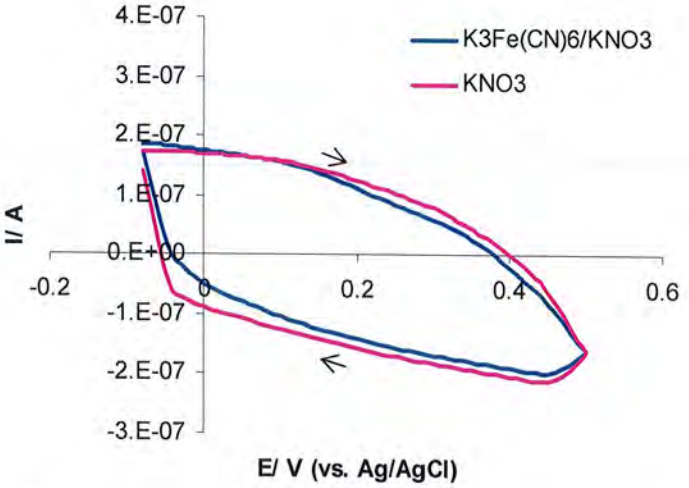

Comparison of the CVs obtained by the PTE coated electrode (after 24 hours treatment) in either 1 mM $K_3Fe(CN)_6$ / 100 mM KNO_3 or 100 mM KNO_3 only. Scan rate 200 mVs^{-1}.

In the case of the bare gold electrode the oxidation of $Eu^{2+} \rightarrow Eu^{3+}$ shows as a peak at -0.66 V and the $Eu^{3+} \rightarrow Eu^{2+}$ reduction shows as a peak at -0.60 V (Figure 51). The value of $E_{pc} - E_{pa}$ = 60 mV and closely matched peak currents indicate a reversible single electron process. Complete blockage of the electroactive Eu^{2+} was observed when

the BLM is present and this remained the case even when gA or gAN channels were introduced.

Figure 51. *CV of BLM coated electrode with and without ion channels in $Eu(NO_3)_3$.*

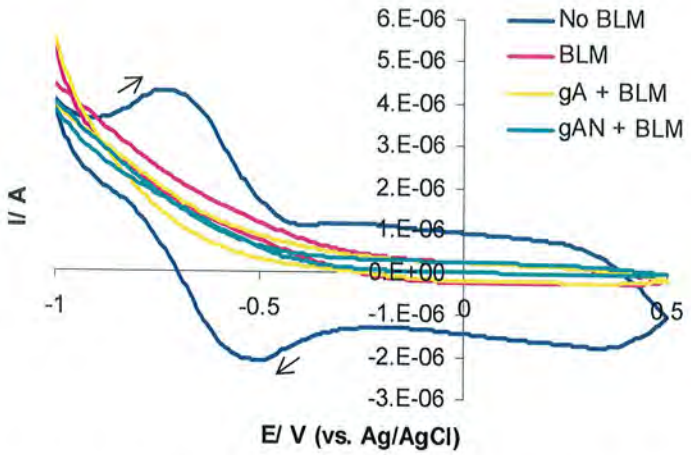

Cyclic voltammograms obtained by uncoated / BLM coated / BLM coated and peptide-treated gold electrodes in 1 mM $Eu(NO_3)_3$ / 100 mM KNO_3.

Differential pulse voltammetry was performed in the same potential region as the Eu^{2+} oxidation peak and demonstrates even more clearly the occlusion of the channels by Eu^{2+} ions. The oxidation current produced by permeation of Eu^{2+} through the different channel types and reacting at the electrode surface is negligible (Figure 52).

Figure 52. *DPV of BLM coated electrode with and without ion channels in $Eu(NO_3)_3$.*

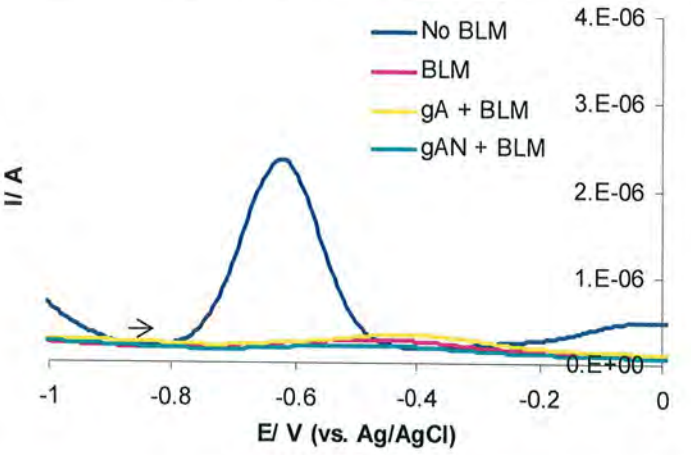

Differential pulse voltammograms of 1 mM $Eu(NO_3)_3$ / 100 mM KNO_3 with the gold electrode coated in BLM and then treated with gA or gAN.

The CV obtained by the bare electrode in Tl^+ solution shows a $Tl^0 \rightarrow Tl^+$ oxidation peak at -0.83 V and a $Tl^+ \rightarrow Tl^0$ reduction peak at -0.72 V. The relative shape and position of these peaks is in reasonable agreement with those reported by Mauzeroll and co-workers, notwithstanding the fact that their experiments were performed using a platinum disc electrode in phosphate buffer electrolyte.[4] The oxidation peak is much smaller than the reduction peak due to there being only a finite amount of Tl^0 adsorbed at the gold surface which can be oxidised, whereas there is an excess of Tl^+ in solution available for reduction. The value of $E_{pc} - E_{pa} = 110$ mV and broadened oxidation peak also indicate *quasi*-reversible electrode kinetics of the $Tl^0 \rightarrow Tl^+$ oxidation process, which is again indicative of a surface adsorbed reactant. Complete blockage of the electroactive Tl^+ was observed when the BLM is present however, unlike the Eu^{2+} case, a voltammetric response for the oxidation of $Tl^0 \rightarrow Tl^+$ was observed with the incorporation of gA and gAN channels (Figure 53).

Figure 53. *CV of BLM coated electrode with and without ion channels in $TlNO_3$.*

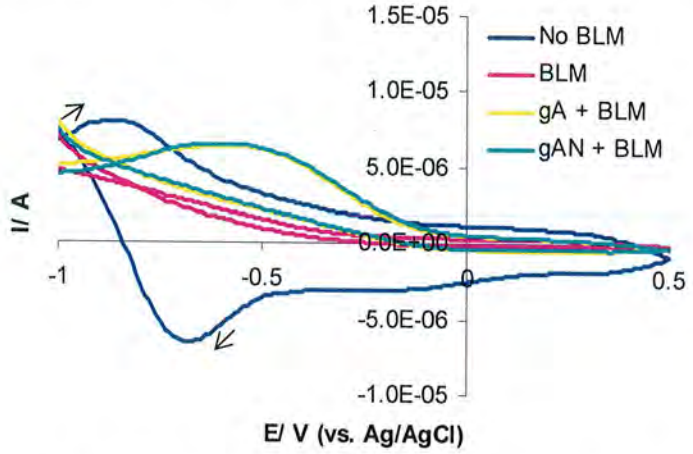

Cyclic voltammograms obtained by uncoated / BLM coated / BLM coated and peptide-treated gold electrodes in 1 mM $TlNO_3$ / 100 mM KNO_3.

This is an interesting observation because since the WE is initially biased at negative potential the thallium must be in the Tl^0 oxidation state at the beginning of the sweep. It can not permeate through the channels in this uncharged Tl^0 state, so how can it get to the gold surface to generate the $Tl^0 \rightarrow Tl^+$ oxidation peak in the forward direction? The only explanation is that Tl^+ spontaneously diffuses through the channels when the electrode is immersed in the $TlNO_3$ electrolyte solution before a potential is applied. This would suggest there was a thin layer of Tl^+ at the electrode surface that would

reduce to Tl^0 the moment the electrode was biased at -1.0 V. Previous *in situ* STM measurements have shown underpotential deposition (UPD) of thallium on gold at potentials negative of about -0.4 V.[27] When the potential is swept to more positive values the surface Tl^0 begins to oxidise, but because it is gold-adsorbed and trapped in the channel recess the kinetics are slow and elongation of the oxidation peak is observed.

Figure 54. *DPV of BLM coated electrode with and without ion channels in $TlNO_3$.*

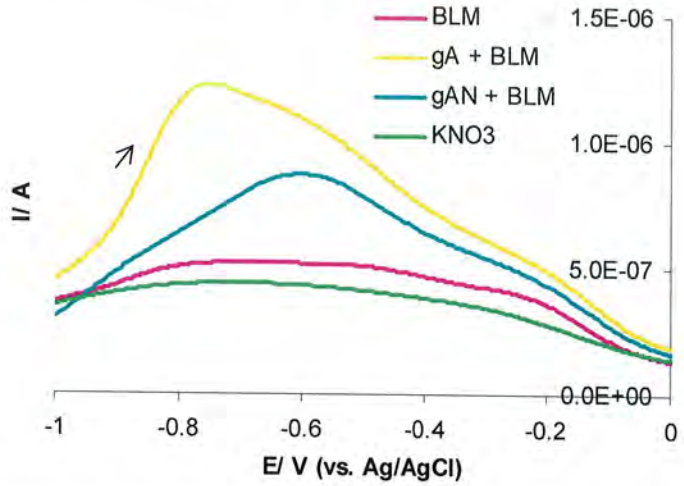

Differential pulse voltammograms of 1 mM $TlNO_3$ / 100 mM KNO_3 with the gold electrode coated in BLM and then treated with gA or gAN. The green line shows the voltammogram obtained with a bare electrode in KNO_3 only. The voltammogram using the uncoated electrode, which has a large (2.4×10^{-5} A) peak at -0.72 V, has been omitted from the plot for scale reasons.

The differential pulse voltammogram (Figure 54) further highlights the elongation of the Tl^0 oxidation peak and appears to show a slight shoulder suggesting a second peak could be present at slightly higher potential. It was initially thought this second peak was due to reduction of hydrogen (from water) although no hydrogen evolution was observed at the electrode surface during the CV experiments. This idea can be dismissed because a voltammogram obtained with an uncoated electrode in KNO_3 supporting electrolyte shows no response over the potential range of the $Tl^0 \rightarrow Tl^+$ transition.

6.3.3 *The influence of supporting electrolyte on the $Fe(CN)_6^{3-}$ / $Fe(CN)_6^{4-}$ couple*

CV was also used to monitor the effect of different supporting electrolyte cations on the size and position of the $Fe(CN)_6^{3-}$ / $Fe(CN)_6^{4-}$ redox peaks. Heterogeneous rate constant,

diffusion coefficient and transfer coefficient values for the $Fe(CN)_6^{3-}/Fe(CN)_6^{4-}$ couple in a variety of supporting electrolytes were calculated and are shown later in Tables 7 and 8.

When the alkali metal nitrates are used there is a slight shift in the $Fe(CN)_6^{4-}$ oxidation peak to more positive potential. For alkali metal nitrate electrolytes the extent of this shift appears related to the ionic radius of the cation, with $LiNO_3$ having least effect and $CsNO_3$ the most as shown in the upper plot of Figure 55. The CV obtained in $LiNO_3$ electrolyte differs from the others in that it shows slight elongation and increased peak separation, indicative of slower heterogeneous kinetics and uncompensated solution resistance. Li^+ differs from the other electrolyte cations studied in that it has the smallest radius (90 pm)[28] and the lowest ionic conductivity (38.7 S cm^2 mol^{-1})[29] explaining the greater solution resistance.

The middle plot of Figure 55 shows the results obtained for NH_4NO_3 and NMe_4NO_3 supporting electrolytes. The CVs obtained in NH_4NO_3 electrolyte are closely matched to those obtained in KNO_3, differing only slightly in the double-layer capacitance at the electrode surface. This capacitive variation is accounted for by the different ionic radii of electrolyte ions specifically adsorbed at the electrode surface. K^+ has a larger ionic radius than NH_4^+ (152 pm vs. 143 pm according to Table 6) meaning the distance between the capacitor plates of the double layer is greater, resulting in the capacitance being lower (equation 4). Also note that since K^+ and NH_4^+ have identical values of ionic conductivity (Table 6) this factor is precluded from having any influence on the differing voltammogram peak currents. In NMe_4NO_3 electrolyte the voltammogram is elongated and flattened similar to, although not quite as pronounced, as the $LiNO_3$ case. Unlike the $LiNO_3$ case the voltammogram recorded in NMe_4NO_3 has retained the shape of its peaks, suggesting the electrode reaction proceeds at a greater rate. The narrower shape of the voltammogram also suggests lower solution resistance than the $LiNO_3$ case, which is in agreement with the slightly greater ionic conductivity of the NMe_4^+ ion.

The lower plot of Figure 55 shows the effect of including the Tl^+ and Eu^{3+} cations in the supporting electrolyte. Immediately obvious is that, in agreement with Beriet and Pletcher's observations with the Sr^{2+} ion,[23] the multicharged Eu^{3+} cation (in the 3+

oxidation state over the potential range of the $Fe(CN)_6^{3-}/Fe(CN)_6^{4-}$ couple) causes the formal potential to shift more positive than lesser charged electrolyte cations do. The Eu^{3+} ion produces a much larger potential shift (~ 120 mV) than the Sr^{2+} ion does (~ 20 mV). The trend in peak heights ($Eu^{3+} < K^+ < Tl^+$) matches the trend in cationic radii, which is again attributable to the thickness and capacitance of the electrolyte double-layer. Considering ionic radii only the oxidation peak current recorded in the presence of Eu^{3+} appears slightly lower than it should do in relation to the neighbouring peaks obtained in K^+ and Tl^+. This slight irregularity in peak current can be explained in terms of the increased electrostatic influence of the multicharged ion on the double-layer. In the presence of $TlNO_3$ the forward oxidation peak is shifted to a slightly more positive potential than in the presence of the alkali metal nitrates.

Figure 55. *CV data for the $Fe(CN)_6^{3-}/Fe(CN)_6^{4-}$ couple in various supporting electrolytes.*

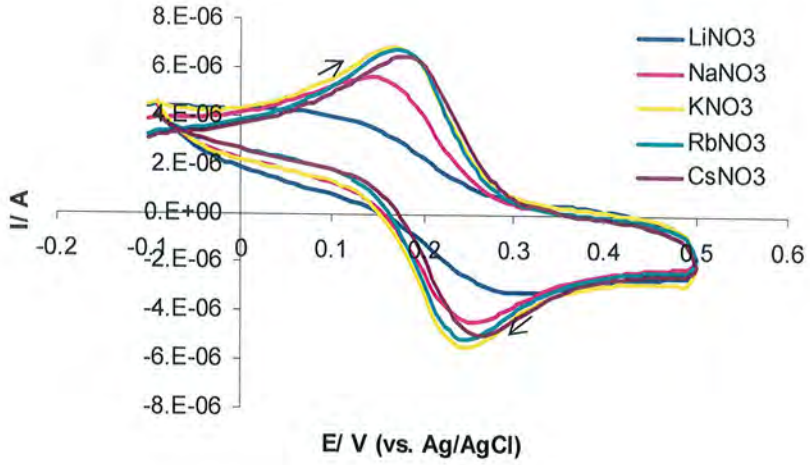

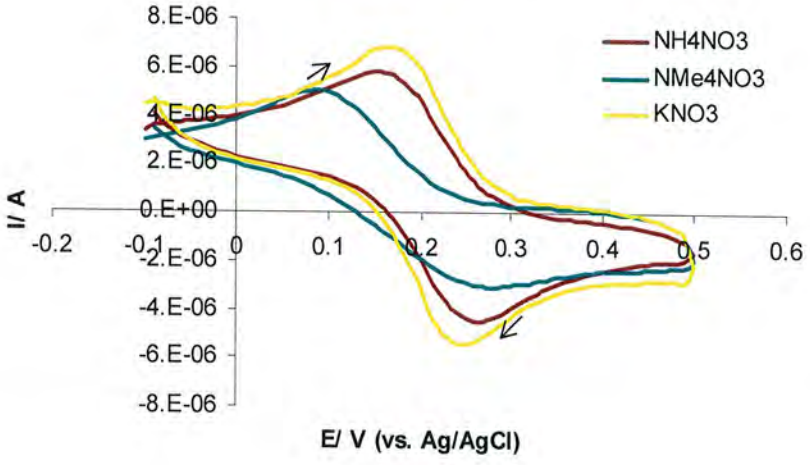

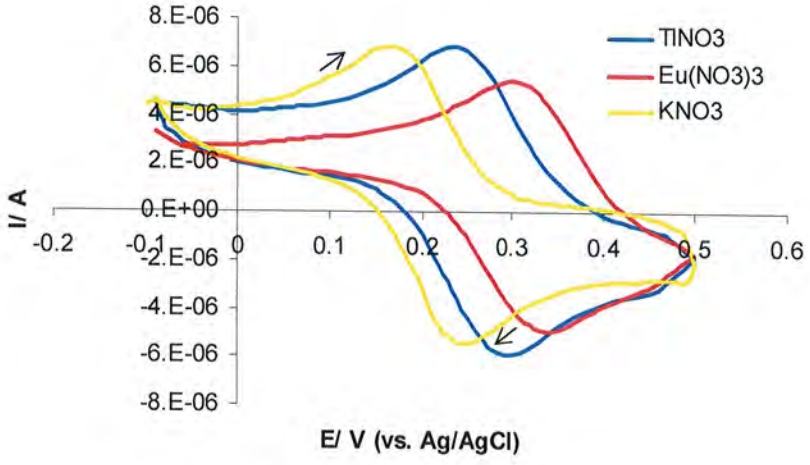

CVs data for the $Fe(CN)_6^{3-}/Fe(CN)_6^{4-}$ couple in various supporting electrolytes at a scan rate of 200 mVs^{-1}. Samples contain 1 mM $K_3Fe(CN)_6$ / 100 mM XNO_3. For comparison the KNO_3 voltammogram is overlaid on each plot above.

Table 6. *Ionic radii and conductivity data.*

Ion	*Ionic radius/ pm**	*Ionic conductivity in water/ S cm^2 mol^{-1}*	*References*
Li^+	90	38.7	28, 29
Na^+	116	50.7	
K^+	152	73.5	
Rb^+	166	77.8	
Cs^+	181	77.2	
Tl^+	164	-	
Eu^{2+}	131	-	
Eu^{3+}	109	-	
NH_4^+	143	73.5	30, 29
NMe_4^+	251	44.9	
$Fe(CN)_6^{4-}$	433	442.0	31, 29
$Fe(CN)_6^{3-}$	445	302.7	

**This is the radius of the unsolvated ion.*

The dimensionless transfer co-efficient, α, of the $Fe(CN)_6^{4-}$ reaction is related to the transition state structure of the heterogeneous electron transfer. Rapid electron transfer reactions at metal electrodes tend to have $\alpha \sim 0.5$, corresponding to a transition state exactly half way between the reactant and product. When $\alpha > 0.5$ the transition state is closer to the product and when $\alpha < 0.5$ the transition state is closer to the reactant. Variation in the value of α tends to influence the shape of the voltammogram, but not the peak position. The values of α (Table 7) were determined from a Tafel plot constructed from each 200 mVs^{-1} set of CV data (Figure 56).

Figure 56. *Tafel plot data for the $Fe(CN)_6^{3-}$ / $Fe(CN)_6^{4-}$ couple in various supporting electrolytes.*

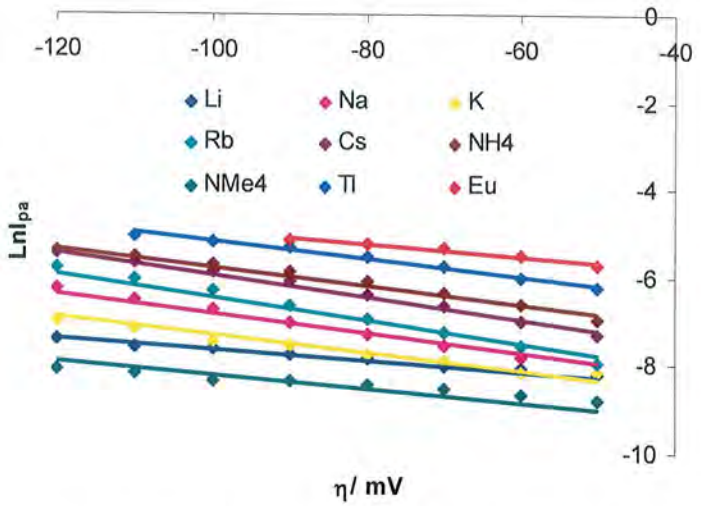

The Tafel region is shown for each supporting cation. Plots were obtained from CVs with a scan rate 200 mVs^{-1}. Note that the data corresponding to the Tl^+ and Eu^{3+} cations deviates sharply from linearity at more negative overpotential.

Of the nine electrolyte cations studied only three, Li^+, NMe_4^+ and Eu^{3+}, result in values of $\alpha < 0.5$. Li^+, the smallest cation (r = 90 pm), corresponds to α = 0.32; NMe_4^+, the largest cation (r = 251 pm), corresponds to α = 0.40; and Eu^{3+}, the only multicharged cation (r = 109 pm), corresponds to α = 0.36. Considering the alkali metal cation electrolytes the general trend is the overall increase of α with ionic radius. The value of α increases due to the larger cations imposing an increasingly product-like transition state on the $Fe(CN)_6^{4-}$ ion, corresponding to lower activation energy for the electrode process. This compliments previous suggestions that the larger alkali metal ions are more effective catalysts of $Fe(CN)_6^{4-}$ oxidation than the smaller ions in the group.[21,23] Of these three $\alpha < 0.5$ cations it should be noted that the CVs obtained in Li^+ and NMe_4^+ electrolytes have similarly low E_{pa} values (~ 100 mV vs. Ag/AgCl) whereas the Eu^{3+} electrolyte results in the highest E_{pa} of all the cations studied (~ 290 mV). It therefore follows that the value of E_{pa} can not be attributed solely to the ionic radius of the electrolyte cation, although the ionic charge must be an important factor. Also of interest is that similarly low values of α can be observed with very small (Li^+, Eu^{3+}) or very bulky (NMe_4^+) ionic participation in the transition state. In general terms the medium sized cations studied result in higher values of α although, as will be discussed later, the value of α seems to have little influence on the heterogeneous rate constant.

Figure 57. *Plots used to determine D values.*

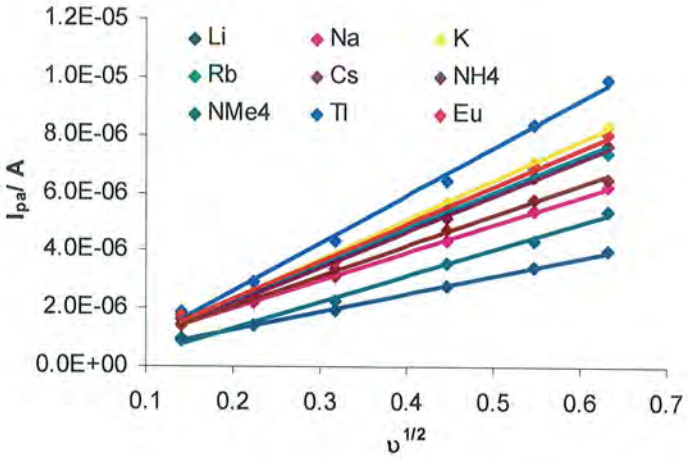

According to the Randles-Sevcik equation (equation 42) a plot of i_{pa} against $v^{1/2}$ was used to evaluate the diffusion coefficient of $Fe(CN)_6^{4-}$ in each supporting electrolyte (Figure 57).

$$i_p = (2.69 \times 10^5) n^{3/2} A D_A^{1/2} v^{1/2} [A]_{bulk} \qquad (42)$$

Where A is the electrode area (cm^2), $[A]_{bulk}$ is the concentration of the electroactive species (mol cm^{-3}), D_A is the diffusion coefficient ($cm^2\ s^{-1}$) and v is the scan rate ($V\ s^{-1}$). The $Fe(CN)_6^{4-}$ oxidation current in each supporting electrolyte displays good ($R^2 > 0.99$ in all cases) linear relationship with the square root of the scan rate.

Table 7. *CV data for the $Fe(CN)_6^{3-}/Fe(CN)_6^{4-}$ couple in various supporting electrolytes.*

Supporting electrolyte	*Scan rate/ mVs^{-1}*	*E_{pa}/ (± 5) mV*	*I_{pa}/ (± 0.05) μA*	*α* (± 0.05)	*D/ $(\pm 0.10) \times 10^{-6}$ cm^2s^{-1}*
$LiNO_3$	*20*	*150*	*0.93*	*0.32*	*1.35*
	50	*140*	*1.40*		
	100	*120*	*1.96*		
	200	*110*	*2.79*		

$LiNO3$ (cont.)	300	90	3.46		
	400	80	4.00		
$NaNO_3$	20	160	1.45	0.57	3.24
	50	150	2.18		
	100	150	3.12		
	200	140	4.35		
	300	130	5.38		
	400	130	6.21		
KNO_3	20	170	1.61	0.54	6.46
	50	170	2.60		
	100	170	3.72		
	200	170	5.67		
	300	160	7.08		
	400	160	8.30		
$RbNO_3$	20	170	1.60	0.67	5.19
	50	170	2.52		
	100	170	3.67		
	200	170	5.44		
	300	170	6.88		
	400	160	7.37		
$CsNO_3$	20	190	1.59	0.65	5.35
	50	180	2.41		
	100	180	3.39		
	200	180	5.10		
	300	180	6.54		
	400	180	7.66		
NH_4NO_3	20	160	1.45	0.53	3.80
	50	160	2.27		
	100	160	3.13		
	200	150	4.72		
	300	150	5.79		
	400	150	6.50		
NMe_4NO_3	20	100	0.99	0.40	2.81
	50	90	1.40		

NMe_4NO_3 (cont.)	100	90	2.26		
	200	90	3.60		
	300	80	4.37		
	400	80	5.37		
$TlNO_3$	20	230	1.86	0.51	9.36
	50	230	2.93		
	100	230	4.33		
	200	230	6.42		
	300	230	8.36		
	400	230	9.95		
$Eu(NO_3)_3$	20	290	1.74	0.36	5.82
	50	290	2.55		
	100	290	3.63		
	200	290	5.38		
	300	290	6.94		
	400	290	8.02		

The heterogeneous rate constant, k^o_{calc}, of the $Fe(CN)_6^{4-}$ oxidation was calculated by the methods of Nicholson,[11] Eisner[12] and Kochi[13] discussed earlier. The alternative methods provide a similar trend in k^o_{calc} value for each electrolyte cation, although Nicholson's method (Table 8, column A) gave a much higher k^o_{calc} value for the Eu^{3+} ion than the others. The anomalously high Eu^{3+} result, combined with the fact that Nicholson's original experiments were based on a value of $\alpha = 0.5$, suggest it is the least reliable method of the three. Furthermore the only method to explicitly consider the peak potentials, that of Kochi (Table 8, column C), appears to have the closest relationship between k^o_{calc} and E_{pa} for the data obtained. The data obtained by Kochi's method shows that Li^+ and NMe_4^+, the ions resulting in the lowest E_{pa} values, display the lowest k^o_{calc} values and Tl^+ and Eu^{3+}, the ions resulting in the highest E_{pa} values, display the highest k^o_{calc} values. This agrees with the idea that the smaller alkali metal cations like Li^+ somehow bind to the $Fe(CN)_6^{4-}$ ion and catalyse the oxidation process much less efficiently than multicharged but similarly sized ions like Eu^{3+}. This implies that it is

charge density rather than ionic radius of the electrolyte cation that is the most influential factor.

For the alkali metal cation electrolytes the trend in the value of k^o_{calc} is consistent across all three methods of calculation, namely: $Li^+ < Na^+ < Rb^+ \sim Cs^+ < K^+$. This suggests that K^+ is the most efficient catalyst of the $Fe(CN)_6^{4-}$ oxidation process, which differs slightly from the previous results of Peter and coworkers,[21] which puts Cs^+ at the top. Despite the apparent relationship between alkali metal ionic radius and k^o_{calc} (notwithstanding the anomalous position of K^+ within the series) the ionic radius and indeed transition state structure can not be the only factor to influence the rate of catalysis. This is evidenced by the observation that the small Eu^{3+} ion, despite creating a reactant like transition state, results in the largest peak potential (E_{pa}) and largest heterogeneous rate constant (k^o). Conversely the large NMe_4^+ ion also results in a reactant like transition state, but in this case small values of E_{pa} and k^o. The poor relationship between ionic radius, α and k^o is confirmed by the observation that the Tl^+ ion, although being similar in size and charge to Rb^+ (164 pm vs. 166 pm), results in a much smaller α (α = 0.514 vs. 0.671) and faster heterogeneous rate (k^o = 6.50 vs. 2.80 × 10^{-3} cms^{-1}).

These preliminary observations suggest that the values of E_{pa} and k^o are not directly related to either the transition state structure or the size of the electrolyte cation alone. Eu^{3+} has a very similar radius to Na^+ (109 pm vs. 116 pm) yet the transition state structures (α = 0.357 vs. α = 0.570) and k^o values (1.81 vs. 6.51 × 10^{-3} cms^{-1}) are very different suggesting that cation charge as well as radius affect the rate of heterogeneous electron transfer.

An interesting point is that the rate constants obtained by all three methods are low and tending towards *quasi*-reversibility. This has no bearing on the relative order of the rate constants obtained, but is an unusual observation because the hexacyanoferrate couple is often quoted as a textbook example of reversible electron transfer. The rate constants reported in table 8 are similar to those previously obtained at a platinum electrode in a KCl electrolyte.[18] However, unusually low rate constants have been observed before with platinum,[32] boron-doped diamond[33] and gold electrodes[34] and have been attributed

to the surface adsorption of polymeric hexacyanoferrate film, which can occur at even low millimolar concentrations of $Fe(CN)_6^{3-}/Fe(CN)_6^{4-}$.

Table 8. *Tafel and kinetic data.*

Supporting electrolyte	*Ln i_0**	*i_0/ $\mu A\ cm^{-2}$*	*k^o_{calc}/ $\times 10^{-3}$ cms^{-1} †*		
			A	*B*	*C*
$LiNO_3$	*-8.898*	*6.797*	*0.632*	*4.961*	*1.794*
$NaNO_3$	*-9.070*	*5.723*	*3.116*	*5.835*	*1.808*
KNO_3	*-9.374*	*4.233*	*16.334*	*8.623*	*4.700*
$RbNO_3$	*-9.067*	*5.740*	*14.650*	*6.611*	*2.796*
$CsNO_3$	*-8.457*	*10.564*	*14.874*	*6.906*	*3.093*
NH_4NO_3	*-7.854*	*19.307*	*4.243*	*6.576*	*2.551*
NMe_4NO_3	*-9.807*	*2.739*	*1.244*	*6.555*	*1.967*
$TlNO_3$	*-7.182*	*37.807*	*36.018*	*10.557*	*6.495*
$Eu(NO_3)_3$	*-6.369*	*85.241*	*238.670*	*9.900*	*6.511*

**This is the Ln i_0 value obtained directly from the 1.6 mm diameter (0.0201 cm^2 area) gold electrode. Recall that Tafel plots were drawn as Ln i (mA) against η (mV) - therefore exp(Ln i_0) gives a mA value which is converted to μA and normalised in the i_0 column.*

†Rate constants obtained by the following methods - A: Nicholson,[11] B: Eisner,[12] C: Kochi.[13]

From the data collected a few conclusions can be made. Firstly the E_{pa}, α and k^o values obtained indicate that either very small or very large electrolyte cations impose a reactant like transition state on the oxidation reaction by reinforcing (rather than distorting) the $Fe(CN)_6^{4-}$ ionic structure. The data also indicate that small and highly charged ions, despite imposing low α values, result in the fastest heterogeneous electron transfer as confirmed by the shift in E_{pa} and k^o values. Electroactive cations (Eu^{3+} and Tl^+) appear to have more catalytic influence that similarly sized and charged electroinactive ions. It is also likely that the slow heterogeneous kinetics result from an electrode surface adsorbed hexacyanoferrate film.

6.3.4 *Fast scan cyclic voltammetry of the $Fe(CN)_6^{3-}/Fe(CN)_6^{4-}$ couple*

From the slow scan CV data it was clear that further investigation of the $Fe(CN)_6^{4-}$ oxidation process was required. To this end fast scan CV at platinum UMEs was attempted using the same electrolyte systems. Unlike slow scan CV, where the

duration of the potential sweep is sufficiently long to allow complete reaction at the electrode surface, the rapid sweep of fast scan CV means the concentration of the reactant may never reach zero. A consequence of this is that the oxidation peak occurs at a much higher potential than the reactant actually begins to oxidise. The inverse is true of the reduction peak. This time lag results in enhanced peak separation and allows the study of ultrafast heterogeneous kinetics and coupled homogeneous events that are masked by conventional diffusional controlled voltammetry.

The preliminary fast scan CV data collected in this investigation are shown in Appendix 2.

6.4 References

1. A. Nelson and D. Bizzotto, *Langmuir*, 1999, **15**, 7031
2. A. Nelson, *Biophys. J.*, 2001, **80**, 2694
3. S. G. Blankenborg, M. Sluyers-Rehbach and J. H. Sluyters, *J. Electroanal. Chem.*, 1993, **349**, 255
4. J. Mauzeroll, M. Buda, A. J. Bard, F. Prieto and M. Reuda, *Langmuir*, 2002, **18**, 9453
5. R. A. Marcus, *Angew. Chem. Intl. Ed. Engl.*, 1993, **32**, 1111
6. R. A. Marcus, *J. Chem. Phys.*, 1956, **24**, 966
7. R. A. Marcus, *J. Chem. Phys.*, 1965, **43**, 679
8. N. S. Hush, *J. Chem. Phys.*, 1958, **28**, 962
9. N. S. Hush, *Trans. Faraday Soc.*, 1961, **57**, 557
10. R. S. Nicholson, *Anal. Chem.*, 1964, **36**, 706
11. R. S. Nicholson, *Anal. Chem.*, 1965, **37**, 1351
12. E. Gileadi and U. Eisner, *J. Electroanal. Chem.*, 1970, **28**, 81
13. R. J. Klingler and J. K. Kochi, *J. Phys. Chem.*, 1981, **85**, 1731
14. R. A. Marcus, *Electrochim. Acta*, 1968, **13**, 995
15. R. A. Marcus and N. Sutin, *Biochim. Biophys. Acta*, 1985, **811**, 265
16. Y. Fu and T. W. Swaddle, *Chem. Commun.*, 1996, 1171
17. Y. Fu and T. W. Swaddle, *J. Am. Chem. Soc.*, 1997, **119**, 7137
18. Y. Fu and T. W. Swaddle, *Inorg. Chem.*, 1999, **38**, 876
19. C. Lee and F. C. Anson, *J. Electroanal. Chem.*, 1992, **323**, 381
20. D. J. Bieman and W. R. Fawcett, *J. Electroanal. Chem.*, 1972, **34**, 27
21. L. M. Peter, W. Durr, P. Bindra and H. Gerischer, *J. Electroanal. Chem.*, 1976, **71**, 31
22. S. A. Campbell and L. M. Peter, *J. Electroanal. Chem.*, 1994, **364**, 257
23. C. Beriet and D. Pletcher, *J. Electroanal. Chem.*, 1993, **361**, 93
24. A. J. Bard, M. Stratmann and G. S. Wilson (eds), *Encyclopedia of Electrochemistry, Volume 9: Bioelectrochemistry*, Wiley-VCH, Weinheim, 2002
25. F. Macias and M. E. Starzak, *Biochim. Biophys. Acta*, 1993, **1153**, 331
26. Z. Shi, S. Wu and J. Lipowki, *J. Electroanal. Chem.*, 1995, **384**, 171
27. W. Polewska and R. Adzic, *Proc. SPIE*, 1999, **3725**, 249
28. R.D. Shannon, *Acta Cryst.*, 1976, **A32**, 751

29. P. W. Atkins and J. de Paula, *Physical Chemistry (7th Edition)*, Oxford University Press, Oxford, 2004
30. W. L. Masterton, D. Bolocofsky and T. P. Lei, *J. Phys. Chem.*, 1971, **75**, 2809
31. D. B. Brown and D. F. Shriver, *Inorg. Chem.*, 1969, **8**, 37
32. C. M. Pharr and P. R. Griffiths, *Anal. Chem.*, 1997, **69**, 4673
33. M. C. Granger and G. M. Swain, *J. Electrochem. Soc.*, 1999, **146**, 4551
34. J. Oslonovitch, Y. -J. Li, C. Donner and K. Krischer, *J. Electroanal. Chem.*, 2003, **541**, 163

Chapter 7

Scanning Kelvin Nanoprobe and Impedance Spectroscopy

7.1 Introduction

7.1.1 *Scanning Kelvin nanoprobe*

The Kelvin probe method of measuring work functions, the theory of which was discussed previously in Chapter 2.1, has primarily been used for surface chemistry applications such as monitoring corrosion, stress and semi-conductors. Biological applications have thus far been limited to the study of protein and nucleic acid microarrays. The Kelvin probe is well suited to this sort of work due to its ability to sense changes in conducting properties of the substrate surface. With microarray spot density continually increasing the errors encountered with standard confocal fluorescent microscopy are magnified. The low brightness of fluorescent dyes, combined with background interference and the dyes themselves interfering with the arrangement of the nucleic acids, all cause issues with detecting hybridisation. The Kelvin probe is a useful high-resolution, non-contact, label-free method of collecting data from each array.

Figure 58 depicts the power of the SKN detection protocol.[1] In this experiment a conventional glass slide, which had been subjected to DNA hybridisation events (the 'zipping' of this single strand with a complimentary strand) followed by fluorescence detection, was examined under the SKN. A 4 × 4 spot array was observed in finer detail, revealing a clear correlation between fluorescent intensity (Figure 58(a)) and work function (Figure 58(b)). CPD and topography measurements were also obtained to assess the homogeneity of a single spot.

Figure 58. *DNA microarrays imaged by the SKN.*[1]

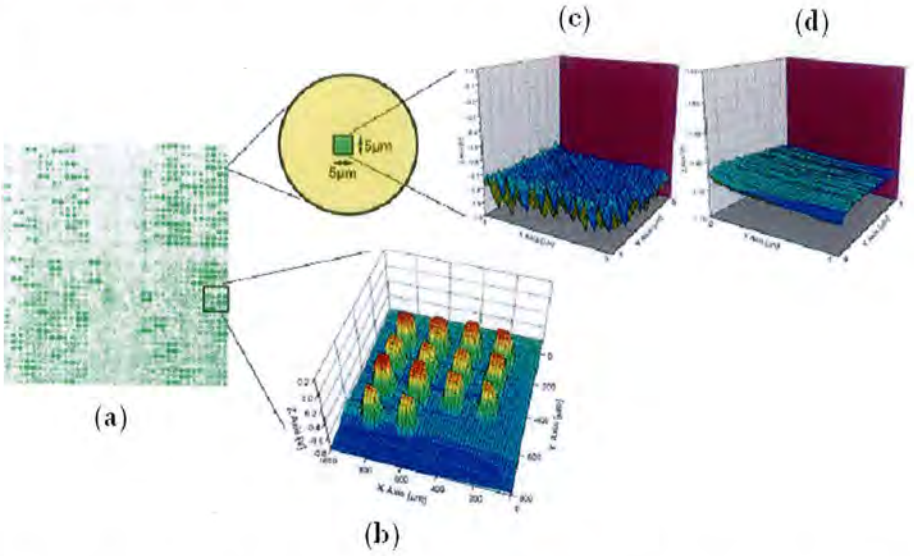

DNA microarray imaged by (a) fluorescence microscopy; (b) SKN CPD measurement with 20 μm scan increment; (c) SKN CPD measurement with 100 μm scan increment; (d) SKN topography measurement with 100 μm scan increment.

The group of Thompson in Toronto has been particularly active in the field of SKN research and were the first to monitor changes in nucleic acid microarrays due to hybridisation by SKN measurements.[2] In this work a new modified Kelvin probe, capable of obtaining tandem measurements of contact potential and surface topography at resolutions of 1 mV and 10 nm respectively, was used to study substrates modified by the attachment of biochemical macromolecules. The high-resolution SKN measurements obtained were sufficient to differentiate between conjugated and unconjugated microarray spots without the need for conventional fluorescent labelling. Subsequent work in this area showed that resolution was possible due to a change in dipole moment between hybridised and unhybridised DNA molecules.[3] An unhybridised single DNA strand has a large lateral dipole moment due to the distribution of negative charge along its length and the fact it is surrounded by negative counterions. During the hybridisation process the overall dipole moment is cancelled out so that the net dipole moment of the strand is zero. A similar change is noticed with protein molecules, where the overall dipole moment depends on the contributions of the constituent parts, which will change with intermolecular interaction. This property allows the Kelvin nanoprobe to be used for the investigation of bimolecular interactions in protein arrays.

7.1.2 *Electrochemical impedance spectroscopy*

Electrochemical impedance spectroscopy (EIS) provides a useful, non-invasive method of characterising the electrical properties of many systems.[4] The theory behind EIS was discussed previously in Chapter 2.5. The technique was first used in 1925 to provide an estimation of the membrane thickness of red blood cells.[5] It wasn't until some 30 years later that the impedance-measured thickness was confirmed by electron microscopy. Low frequency EIS has proved an invaluable probe for the submolecular domains of bilayer membranes and has achieved a spatial resolution in the order of 0.1 nm.[6,7] Even modern day X-ray crystallography and electron microscopy can not match the high resolution results afforded by EIS.

The interaction of gA, g-BOC and g-des with DOPC and DOPC/PS mixed monolayers has been studied by Nelson and co-workers.[8] HMDE supported monolayers were utilised because the N-terminal modified peptides, which are physically prevented from stacking N-terminal-to-N-terminal, display very poor channel cation conduction in phospholipids bilayers. Passage of Tl^+ across the channels was observed voltammetrically and peptide-lipid interaction was assessed by membrane capacitance determined by EIS.

Gold electrode EIS studies have largely been confined to measurements of unsupported 'black' lipid membranes. The group of Naumowicz and co-workers are particularly active in this field and have used EIS to study the dimerisation of gramicidin D (gD) and subsequent transport of monovalent cations across the BLM.[9] A point to note is that the naturally occurring gD mixture was used in these experiments and no effort was made to separate out the component structural variants. BLMs of comparible thickness to those occurring in nature were obtained as bubbles at a Teflon aperture segregating two KCl electrolyte solutions. The equivalent circuit is shown below in Figure 59. Recall from section 2.5.2 that the total (observed) impedance, Z, of the system is a combination of real, R, and imaginary, X, values.

Figure 59. *Equivalent circuit of PC membranes modified with gD.*

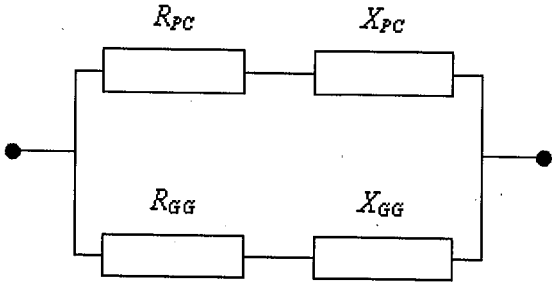

R_{PC}, X_{PC} – impedance of pure phosphatidylcholine bilayer; R_{GG}, X_{GG} – impedance associated with gD dimers.

Assuming the membrane and channel impedance components are in parallel (as shown in Figure 59) the total impedance of the membrane is given by the following equation:

$$\frac{1}{R-jX}=\frac{1}{R_{PC}-jX_{PC}}+\frac{1}{R_{GG}-jX_{GG}} \qquad (91)$$

The real and imaginary components of the total impedance associated with the gD channels are given by:

$$R_{GG}=\frac{R\left(R_{PC}^2+X_{PC}^2\right)-R_{PC}\left(R^2+X^2\right)}{\left(R_{PC}-R\right)^2+\left(X_{PC}-X\right)^2} \qquad (92)$$

$$X_{GG}=\frac{X\left(R_{PC}^2+X_{PC}^2\right)-X_{PC}\left(R^2+X^2\right)}{\left(R_{PC}-R\right)^2+\left(X_{PC}-X\right)^2} \qquad (93)$$

The dimerisation equilibrium constant, K_{GG}, of gD can be written in the form:

$$K_{GG}=\frac{c_{GG}}{c_G^{-2}} \qquad (94)$$

$$c_T=c_G+c_{GG} \qquad (95)$$

$$c_T=\frac{s_{PC}M_{PC}}{nM_G} \qquad (96)$$

$$K_{GG}^{-1/2}=c_T c_{GG}^{-1/2}-c_{GG}^{1/2} \qquad (97)$$

Where c_G is the surface concentration of gD monomer (mol cm^{-2}), c_{GG} is the surface concentration of gD dimers (mol cm^{-2}), c_T is the total concentration of gD in the BLM,

s_{PC} is the surface concentration of phosphatidylcholine in a pure lipid membrane (mol cm^{-2}), M_{PC} is the phosphatidylcholine molar weight (752.08 g mol^{-1}), M_G is the gD molar weight (1880 g mol^{-1})[10] and n is the gD to phosphatidylcholine weight ratio in the forming solution.

Nyquist plots were obtained for BLMs in five different concentrations of gD and KCl as well as for unmodified BLMs. Both imaginary and real impedance components were observed to be 2 orders of magnitude less for the gD treated membranes compared to the untreated ones. Semicircular plots were obtained consistent with the BLM acting as a dielectric with leakage. Slight distortion of the circles arose due to uneven distribution of lipid. The imaginary and real impedances due to the presence of gD dimers (X_{GG} and R_{GG}) only show a linear relationship indicating Warburg impedance, Z_W, predominates. Z_W is the impedance characteristic of a diffusional process at the electrode layer. Calculation of the Warburg coefficient, σ, allowed the determination of the surface fraction occupied by active gD dimers (the coverage), Θ ($0 < \Theta < 1$), and the area occupied by a single gD dimer, A_G. The A_G value obtained, 124 ± 1 Å^2 per molecule, was reported unequivocally for the first time although most previous reports have placed the value in the range 120 – 150 Å^2 per molecule.[11,12,13]

The same research group has also used EIS to study a two-component lipid membrane composed of phosphatidylcholine (PC) and phosphatidylethanolamine (PE).[14] These lipids were chosen due to their high occurrence in nature and are known to assemble into a 1:1 bilayer complex.[15] As with their earlier work, the BLM bubble was assembled on the aperture of a Teflon cap and KCl electrolyte was used. The Nyquist plots obtained showed impedance semicircles (Figure 60).

Figure 60. *Nyquist plots of different BLMs.*[14]

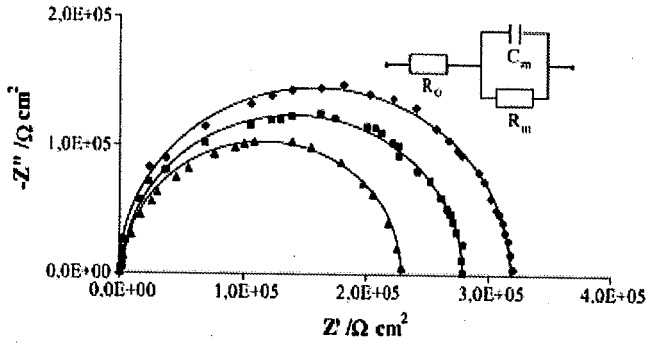

Nyquist plots over the frequency range 0.1 Hz – 10 kHz for a membrane made of PC (▲), PC-PE (■) or PE (◆). The solid line represents best fit in all cases. Inset shows equivalent circuit.

The Nyquist plot shows that the spectra of the PC-PE bilayers are higher than those of PC only membranes, confirming the successful incorporation of PE into the bilayer and demonstrating the effect on membrane capacitance and resistance. The dependence of PC-PE membrane capacitance, C_m, on molar fraction of PE was also plotted. The plot produced deviated from linearity suggesting the presence of some inter-layer bonding within the membrane. A general trend of decreasing capacitance with increasing PE molar fraction was observed. This was explained in terms of increasing membrane thickness with PE incorporation. The dielectric constant of the membrane also decreases with increasing PE mole fraction.

As series of equations were deduced, that would lead to the calculation of the PC-PE stability constant and complex dimer surface area. Capacitance values of 0.62 ± 0.02 μF cm^{-2} (PC) and 0.32 ± 0.02 μF cm^{-2} (PE) and resistances of $(2.30 \pm 0.25) \times 10^5$ Ω cm^2 (PC) and $(3.20 \pm 0.42) \times 10^5$ Ω cm^2 (PE) were reported, corresponding to the pure mono-lipid bilayers. Knowledge of the maximal surface concentrations of PC (1.96×10^{-6} mol m^{-2}) and PE (2.23×10^{-6} mol m^{-2}) in the pure mono-lipid bilayers allowed the determination of the area occupied by one PC-PE complex molecule. This value was calculated as 155 $Å^2$, which compares favourably with an earlier reported value of 154 $Å^2$.[15] A stability constant of $(2.66 \pm 0.42) \times 10^8$ m^2 mol^{-1} was reported for a BLM with equal mole fractions of PC and PE.

7.1.3 *Summary of Chapter 7*

Our experiments are aimed at the preliminary characterisation of a similar two-component lipid membrane by EIS and SKN. The lipid components, PC and PTE, have

been chosen primarily because the PTE terminal sulphide provides a convenient anchor to a gold electrode surface. Unlike the previous experiments with black lipid membranes our investigations utilised gold-supported PTE-PC bilayers. The reason for this was two-fold: firstly, our SKN set-up at Durham does not allow for the analysis of liquid samples and secondly, an underlying gold surface allows for the detection of analyte ions immediately beyond the BLM ion channels.

7.2 **Experimental procedure**

7.2.1 *Electrochemical impedance spectroscopy of self-assembled BLMs on gold electrodes*

EIS measurements were performed using a Solartron 1260 Impedance/Gain-Phase Analyzer connected to a personal computer. The ZPlot software supplied with the Solartron 1260 was used to collect, plot and interpret the raw impedance data. A self-fabricated 10 ml glass cell was used. The working electrode was a 1.6 mm gold electrode (Bioanalytical Systems, West Lafayette, US). The geometrical area of the gold electrode was 0.02 cm^2. The RE was an aqueous Ag/AgCl electrode (Bioanalytical Systems, West Lafayette, US) and the CE was a self-fabricated 1 cm^2 platinum flag.

BLM was applied to the gold WE in the same manner as described previously (section 6.2.3). Once again, the supported BLMs were treated with gA, gAN or methanol (control). EIS was performed with the peptide treated mixed-bilayer electrode immersed in three different electrolytes: 1 mM $K_3Fe(CN)_6$ / 100 mM KNO_3, 1 mM $Eu(NO_3)_3$ / 100 mM KNO_3 and 1 mM $TlNO_3$ / 100 mM KNO_3. In each case a DC bias of -0.6 V was applied to the WE and an AC frequency range of 1 MHz $\rightarrow$ 0.1 Hz was used. A Nyquist plot of imaginary current, I_{imag}, against real current, I_{real}, was obtained for each electrode / electrolyte combination. Results were also obtained for a range of DC bias values up to 0.5 V.

7.2.2 *Scanning Kelvin nanoprobe scans of self-assembled BLMs on gold substrates*

A gold coated glass slide was used as the substrate. The slide, fabricated by Durham University, Department of Engineering, was produced by electron beam evaporation of gold and the flatness of the bare surface assessed by AFM (Figure 61). BLM was applied to the gold in the same manner as described previously (section 6.2.3). The slide was placed onto the piezo table and clamped with a conducting wire to ensure ground connection. The Scanning Kelvin nanoprobe was controlled via a desktop PC running a

customised LabVIEW application. The scan range was 500 × 500 μm in 10 μm increments. The SKN tip was manually moved within 1 mm of the substrate surface, and controlled thereafter by the computer, which brought it within 100 nm of the surface, close enough to detect the image force of the substrate. The computer thereafter controlled the scan and saved the results in a comma-separated values ASCII file.

Figure 61. *AFM image of gold SKN substrate.*

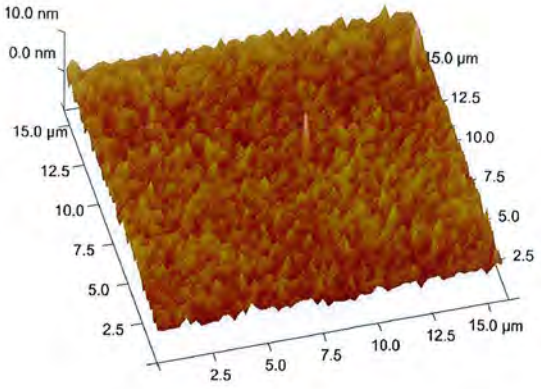

AFM scan showing a 15 × 15 μm portion of the SKN bare gold substrate. The surface topography variation is < 1 nm (0.04 %).

7.3 Results and discussion

7.3.1 *SKN studies of gold supported BLMs*

The CPD value of a mixed (PTE-PC) lipid coated gold substrate was observed to be significantly larger than that of an otherwise identical plain gold substrate. This difference arises because it requires a larger backing potential to equalise the Fermi levels of the tungsten tip and lipid coated gold substrate, than it does the tungsten tip and plain gold substrate. The plots, displayed on identically scaled axes for ease of comparison, are shown below. In each plot the Z-axis corresponds to CPD and X and Y-axes correspond to tip position.

Figure 62. *CPD plots of bare gold and lipid coated gold.*

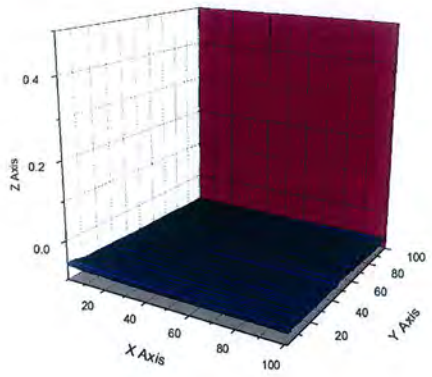

(a) CPD plot of bare gold substrate surface.

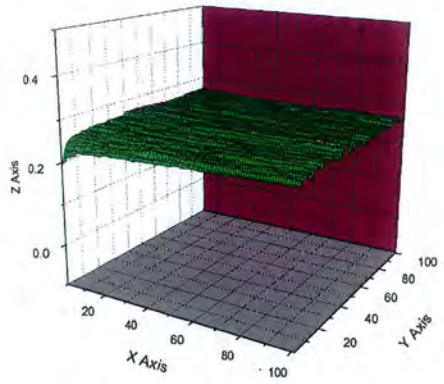

(b) CPD plot of mixed lipid (PTE-PC) coated gold substrate surface.

Fresh PTE-PC substrates were immersed in aqueous peptide solutions overnight to allow channel self-assembly within the membrane. Solutions of gA, gAN and Ala were used for this purpose. The pore diameters of gA / gAN (0.4 nm)[16] and Ala (1.8 nm)[17] are such that the lateral resolution of the Kelvin nanoprobe, 10 nm, should be insufficient to sense the location of individual channels although the cumulative effect on CPD of closely neighbouring channels should be evident. The CPD plots obtained for lipid treated with each peptide, plotted in the same scale as previously, are shown below:

Figure 63. *CPD plots of bare gold and lipid coated gold treated with peptide.*

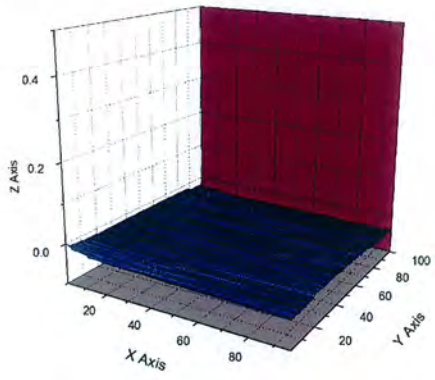

(a) CPD plot of mixed lipid (PTE-PC) coated gold substrate surface treated with gA.

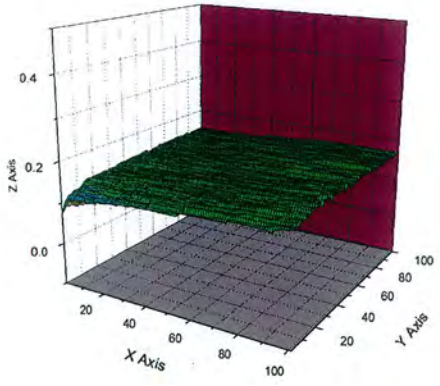

(b) CPD plot of mixed lipid coated gold substrate surface treated with gAN.

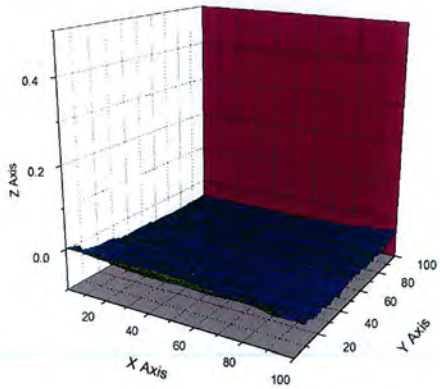

(c) CPD plot of mixed lipid coated gold substrate surface treated with Ala.

Table 9. *Mean CPD values for treated and untreated gold substrates.*

Substrate	*Mean CPD/ mV*	*Std. Deviation/ mV*
Bare gold	-71	3
Lipid coated gold	261	6
Lipid coated gold treated with gA	-24	6
Lipid coated gold treated with gAN	154	18
Lipid coated gold treated with Ala	-43	9

Mean CPD values were obtained by averaging all data points shown on the corresponding CPD plots shown in Figures 62 and 63.

As indicated by Figure 62(a) the CPD plot of bare gold shows that over the surface area probed the mean CPD is ~ -0.07 V. Application of PTE-PC increases the mean CPD to ~ 0.26 V, consistent with the lipid acting as an insulating dielectric between the probe tip and underlying gold surface. Figure 63(a) shows that treatment of the PTE-PC bilayer with gA results in a marked change in mean CPD value to ~ -0.03 V, which is tending towards the plain gold value of ~ -0.07 V. This reduction in CPD value, indicative of a reduced backing potential between substrate and probe tip suggests, as expected, that the integrity of the PTE-PC bilayer is disrupted by introduction of gA channels. This is in agreement with the results presented in chapter 6, in which CV with an identically PTE-PC coated gold electrode demonstrated ion permeation upon treatment with peptide. Figure 63(c) shows that treatment of the PTE-PC bilayer with Ala results in a change in mean CPD ~ -0.04 V, which is in agreement with the change observed for treatment with gA although slightly greater in magnitude indicating a greater extent of membrane disruption. This is accounted for by the larger pore size of Ala compared to gA. Alamethicin pores are composed of bundles of 6 – 8 monomers.[18] Figure 63(b) shows that treatment of the PTE-PC layer with gAN shows only a slight deviation of mean CPD from the untreated lipid case. This is consistent with the idea that the gAN channels are occluded by the oxidised pendant nicotinamide moiety under the ambient conditions of SKN operation. The occlusion means that, in effect, the lipid coating is continuous hydrocarbon with the nicotinamide groups lying at the surface and perpendicular to the membrane plane.

7.3.2 *EIS studies of gold supported BLMs*

EIS measurements also showed a marked difference between a bare gold WE and that coated with PTE-PC. Nyquist plots are shown in Figure 64:

Figure 64. *Nyquist plots obtained with a bare and PTE-PC coated gold electrode in KNO_3.*

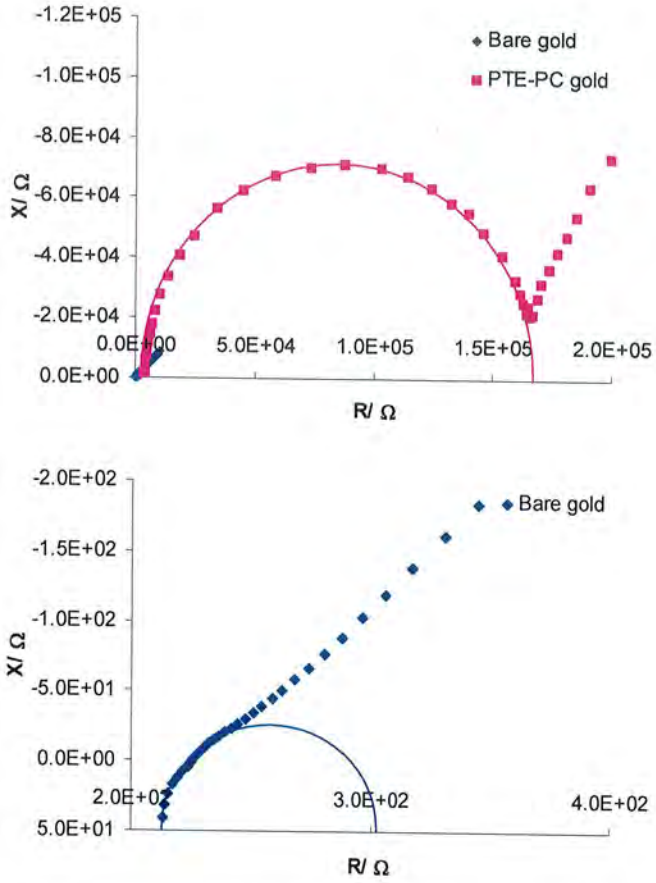

Top figure: Nyquist plots obtained using either a bare or PTE-PC coated gold electrode in 100 mM KNO_3 solution. DC bias = -0.6 V, AC frequency = 1 MHz → 0.1 Hz. Bottom figure: Bare gold plot in finer detail. Resistance values were obtained by subtracting the fitted upper R-intercept from the lower R-intercept.

Data corresponding to these plots are shown in Table 10 towards the rear of this chapter.

Figure 65. *Bode plots corresponding to Figure 64.*

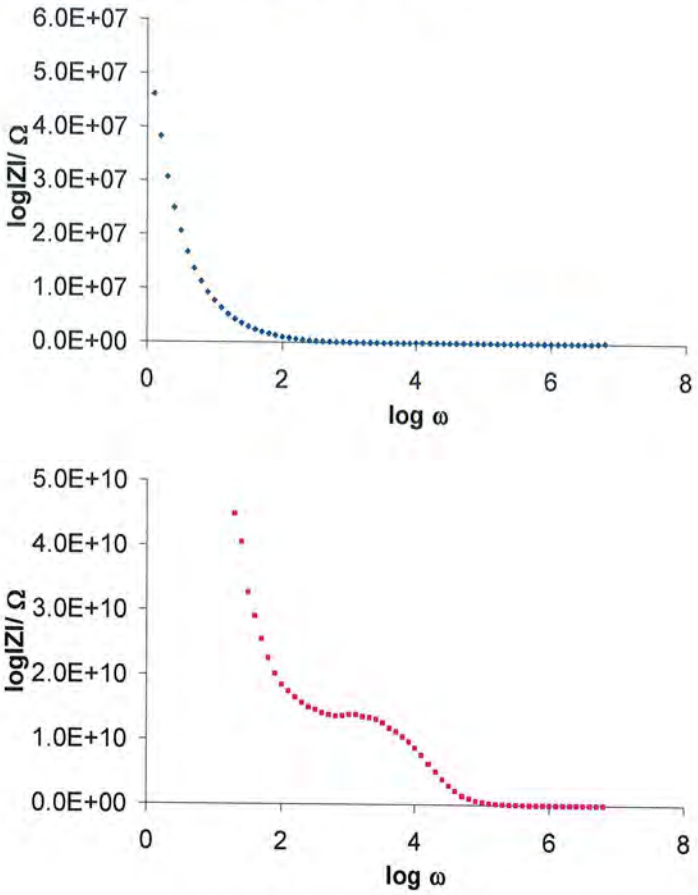

Bode plots obtained using either a bare (top figure) or PTE-PC coated (bottom figure) gold electrode in 100 mM KNO_3 solution. DC bias = -0.6 V, AC frequency = 1 MHz → 0.1 Hz.

Resistance values were obtained from the corresponding Nyquist plot and are equal to the difference between the upper and lower *R*-intercept values on the fitted curve. The double-layer capacitance values (C_{DL}) can be estimated from the impedance measurements using the following equivalent circuit:

Figure 66. *Equivalent circuit used to fit impedance data.*

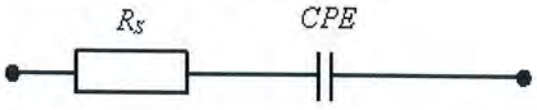

Equivalent circuit used to fit impedance data. R_S and CPE represent the solution resistance and constant phase element respectively.

The CPE is a power-law dependent interfacial capacity, which accounts for the topological imperfections of the electrode surface caused by different crystal facets and

surface roughness.[19] C_{DL} values can be estimated from the impedance of the CPE, which is given by:

$$Z_{CPE} = \frac{1}{Q(j\omega)^{\varphi}} \qquad (98)$$

Where Q is a constant, φ is fractional with a value between 0.5 (for an ideally porous electrode) and 1 (for a perfectly smooth electrode), $j = \sqrt{-1}$ and $\omega = 2\pi f$. If $\varphi = 1$ the CPE is an ideal capacitor and $Q = C_{DL}$.[19] Upon modifying the gold electrode with the low dielectric PTE-PC bilayer the C_{DL} value drops markedly from 1.047×10^{-6} F to 1.512×10^{-8} F.

Another important parameter that can be calculated from R_{CT} values is the electrode coverage, θ. Assuming that all the current is passed by pinholes on the electrode surface, the electrode coverage can be calculated from:[20]

$$(1-\theta) = \frac{R_{CT}^{0}}{R_{CT}} \qquad (99)$$

Where R_{CT}^{0} is the charge-transfer resistance at the bare gold surface and R_{CT} is the charge-transfer resistance at a lipid coated electrode under the same condition. Using this equation a θ value of 99.956% is obtained for the lipid coated electrode in KNO_3 results shown above. This coverage value agrees well with previous studies where impedance measurements were taken of gold SAMs composed of thiolated carboxylic acids of various chain lengths.[21]

A lower DC bias of -0.6 V was used consistently throughout our EIS experiments to ensure that in the case of gAN the nicotinamide moiety was reduced and the channel open. Recall from the SECM feedback curve results in Chapter 3 that the gAN $\rightarrow$ gAN^{+} oxidation occurs at -0.515 ± 0.005 V. The impedance values obtained are of the same magnitude as the previous experiments (Figure 60), although there is understandable variation due to the gold-supported nature of our PTE-PC bilayer in contrast to the free-flowing black lipid membranes of Naumowicz. Furthermore our bilayer is directly attached to the sensing electrode, whereas the earlier results were obtained by placing

the electrode in close proximity to, although not touching, the black lipid surface. Real impedance values of $3.031 \times 10^2\ \Omega$ (bare gold) and $1.668 \times 10^5\ \Omega\ cm^2$ (PTE-PC gold) are obtained by extrapolating the semicircular line of best fit down to the *R*-axis. The curved line of best fit is modelled on the real impedance high frequency intercept (towards left of plot) and low frequency 'turning point' (towards the right of the plot). The high density of data points in these two regions mean there is less margin of error associated with the fitted curve. In contrast to the black lipid membrane the gold-supported PTE-PC data points are a close match to the line of best fit, indicating the lipid coating has a high degree of uniformity. This is unsurprising considering the smooth, inflexible nature of the substrate, slow self-assembly process and rinsing of non-adsorbed and physisorbed lipid from the substrate prior to use.

EIS measurements were also performed using a gold electrode coated with peptide treated PTE-PC bilayers. In order to observe the passage of Tl^+ ions across the peptide channels gA / gAN electrodes were prepared in this manner, immersed in $TlNO_3$ electrolyte and biased at -0.6 V, the potential at which the open state of the gAN channel is observed. The data obtained is shown in the Nyquist plot below (Figure 67):

Figure 67. *Nyquist plots obtained with differently coated gold electrodes in $TlNO_3$.*

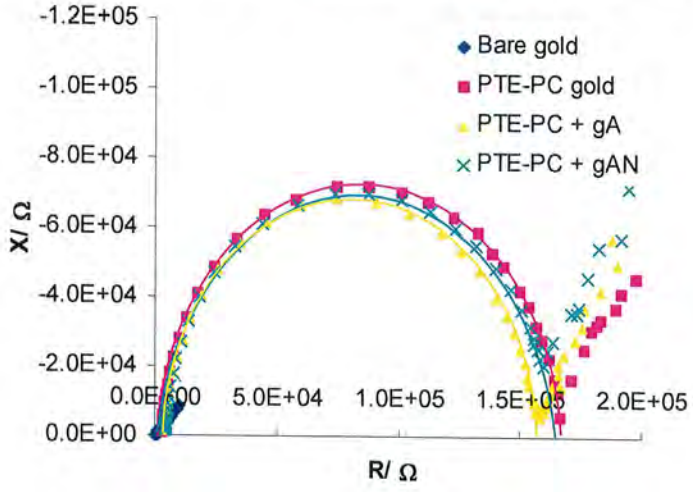

Nyquist plots obtained using either a bare, PTE-PC coated or PTE-PC coated and peptide-treated gold electrode in 1 mM $TlNO_3$ / 100 mM KNO_3 solution. DC bias = -0.6 V, AC frequency = 1 MHz → 0.1 Hz. Data corresponding to these plots are shown in Table 10 towards the rear of this chapter.

The estimated resistance of the gAN treated layer ($1.616 \times 10^5\ \Omega$) falls intermediate between that of the gA treated layer ($1.532 \times 10^5\ \Omega$) and untreated layer ($1.654 \times 10^5$

Ω). This can be explained in terms of temporary steric occlusion of the gAN pore entrance by the reduced nicotinamide pendant group. The nicotinamide unit is free to move within the limits of its tether so on occasion temporarily obstructs the channel mouth thereby preventing the passage of Tl^+ ions. In gA channels, absent of the tethered nicotinamide and with potential independent function, the channel is in a continually open state.

In an attempt to observe the potential-switching of the gAN channels measurements were also obtained with a DC bias of -0.5 V and higher. The gAN impedance curves are compared to the gA curves at the same potential and are shown in the figures below (Figure 68):

Figure 68. *Nyquist plots of PTE-PC coated gold electrodes in $K_3Fe(CN)_6$.*

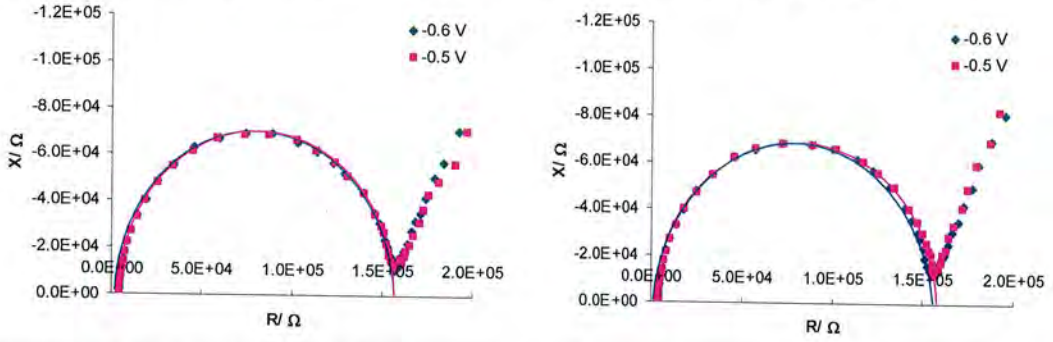

(a) Nyquist plots obtained using PTE-PC coated gA-treated gold electrode in 1 mM $K_3Fe(CN)_6$ / 100 mM KNO_3 solution. DC bias as indicated, AC frequency = 1 MHz → 0.1 Hz.

(b) Nyquist plots obtained using PTE-PC coated gAN-treated gold electrode in 1 mM $K_3Fe(CN)_6$ / 100 mM KNO_3 solution. DC bias as indicated, AC frequency = 1 MHz → 0.1 Hz.

Data corresponding to these plots are shown in Table 10 towards the rear of this chapter.

Figure 69. *Nyquist plots of PTE-PC coated gold electrodes in $TlNO_3$.*

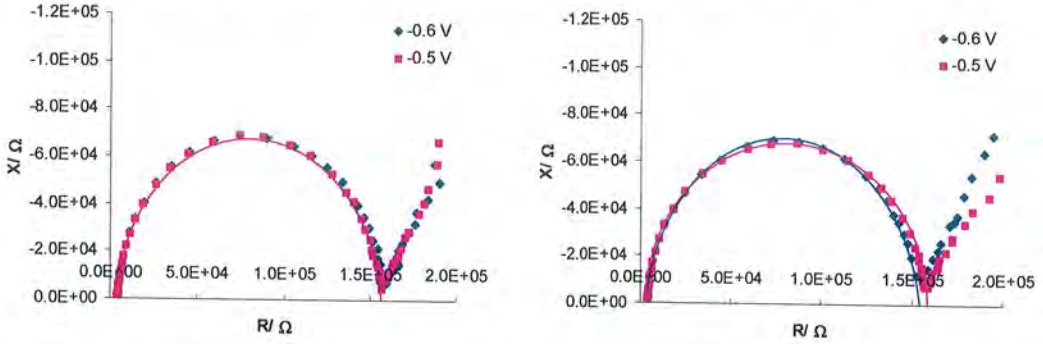

(a) Nyquist plots obtained using PTE-PC coated gA-treated gold electrode in 1 mM $TlNO_3$ / 100 mM KNO_3 solution. DC bias as indicated, AC frequency = 1 MHz → 0.1 Hz.

(b) Nyquist plots obtained using PTE-PC coated gAN-treated gold electrode in 1 mM $TlNO_3$ / 100 mM KNO_3 solution. DC bias as indicated, AC frequency = 1 MHz → 0.1 Hz.

Data corresponding to these plots are shown in Table 10 towards the rear of this chapter.

As Figures 68 & 69(b) demonstrate the gAN real impedance curves in $K_3Fe(CN)_6$ and $TlNO_3$ electrolytes display an increase in resistance of ~ 2 kΩ and ~ 3 kΩ respectively as the membrane potential is stepped from -0.6 V to -0.5 V. This resistance increase is not evident in the gA case (Figures 68 & 69(a)), implying it is the result of the differing peptide functionality and channel occlusion during the gAN → gAN^+ oxidation process. In both $K_3Fe(CN)_6$ and $TlNO_3$ electrolytes, the C_{DL} values increase in magnitude as the gAN electrode potential is switched from -0.6 V to -0.5 V. Considering the ordered array of ions at the lipid surface and gold electrode surface as the parallel plates of a capacitor, this increase in C_{DL} be explained in terms of an increased plate area, A, and dielectric constant, ε, when the pendant nicotinamide moves to occlude the channels.

$$C = \frac{A\varepsilon\varepsilon_0}{d} \qquad (100)$$

In order to further corroborate the switching behaviour the impedance measurements were repeated in $Eu(NO_3)_3$ electrolyte. The Nyquist plots obtained are shown in Figure 70.

Figure 70. *Nyquist plots of PTE-PC coated gold electrodes in $Eu(NO_3)_3$.*

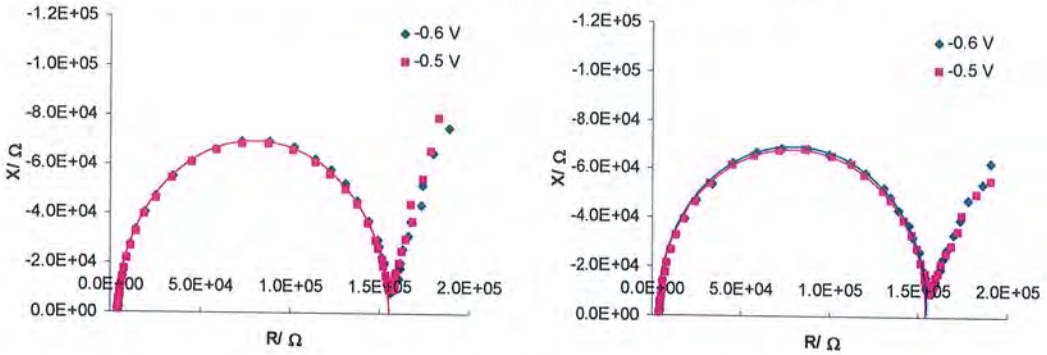

(a) Nyquist plots obtained using PTE-PC coated gA-treated gold electrode in 1 mM $Eu(NO_3)_3$ / 100 mM KNO_3 solution. DC bias as indicated, AC frequency = 1 MHz → 0.1 Hz.

(b) Nyquist plots obtained using PTE-PC coated gAN-treated gold electrode in 1 mM $Eu(NO_3)_3$ / 100 mM KNO_3 solution. DC bias as indicated, AC frequency = 1 MHz → 0.1 Hz.

Data corresponding to these plots are shown in Table 10 towards the rear of this chapter.

Our chronoamperometry experiments in Chapter 6 showed that Eu^{3+}, an ion known to block gramicidin channels by binding at the mouth,[22] failed to pass across the gAN channel when the potential was stepped from channel-open to channel-closed extremes. It therefore follows that in $Eu(NO_3)_3$ electrolyte the gAN channel should show negligible change in impedance between the potentials of -0.6 V and -0.5 V. The impedance results are in good agreement with this with negligible variation in R_{CT} as the applied potential is stepped from -0.6 to -0.5 V.

The θ values obtained (Table 10) show only a slight decrease in coverage when the PTE-PC bilayer is treated with peptide. This can be explained in terms of the conformation constraint imposed on the bilayer by the rigid gold support. This lack of membrane fluidity may inhibit the lateral diffusion and association of the gA / gAN monomers resulting in decreased channel formation. An increase is θ is observed during the gAN → gAN^+ oxidation process consistent with the nicotinamide moiety occluding the peptide channels during this transition.

The apparent charge-transfer rate constants, k_{app}, for the heterogeneous electron-transfer processes (Table 10) can be calculated from the corresponding Nyquist plots by using the following equation:[21]

$$k_{app} = \frac{RT}{F^2 R_{CT}[A]} \qquad (101)$$

where *[A]* is the concentration of electroactive species at the electrode surface.

Table 10. *Impedance data corresponding to the charts in this chapter.*

Figure	Electrode treatment	Electrolyte	Applied potential/ V	Low (R_S)/ Ω	High (R_S + R_{CT})/ Ω	Estimated R_{CT}/ Ω	Estimated C_{DL}/ F	θ/ %	k_{app}/ s^{-1}
Figure 64.	Bare gold	100 mM KNO_3	-0.6	2.308×10^2	3.031×10^2	72.3	1.047×10^{-6}	0	-
	PTE-PC gold			3.324×10^3	1.668×10^5	1.635×10^5	1.512×10^{-8}	99.956	-
Figure 67.	Bare gold	1 mM $TlNO_3$ / 100 mM KNO_3	-0.6	2.307×10^2	3.034×10^2	72.7	1.052×10^{-6}	0	-
	PTE-PC gold			2.943×10^3	1.683×10^5	1.654×10^5	1.191×10^{-8}	99.956	1.610×10^{-9}
	PTE-PC gA			3.957×10^3	1.572×10^5	1.532×10^5	1.275×10^{-8}	99.952	1.738×10^{-9}
	PTE-PC gAN			3.894×10^3	1.655×10^5	1.616×10^5	1.210×10^{-8}	99.955	1.648×10^{-9}
Figure 68(a).	PTE-PC gA	1 mM $K_3Fe(CN)_6$ / 100 mM KNO_3	-0.6	3.832×10^3	1.572×10^5	1.534×10^5	1.275×10^{-8}	99.953	1.736×10^{-9}
			-0.5	3.872×10^3	1.569×10^5	1.531×10^5	1.277×10^{-8}	99.952	1.739×10^{-9}
Figure 68(b).	PTE-PC gAN		-0.6	3.753×10^3	1.571×10^5	1.533×10^5	1.275×10^{-8}	99.952	1.737×10^{-9}
			-0.5	3.767×10^3	1.593×10^5	1.556×10^5	2.509×10^{-8}	99.953	1.711×10^{-9}
Figure 69(a).	PTE-PC gA	1 mM $TlNO_3$ / 100 mM KNO_3	-0.6	3.957×10^3	1.582×10^5	1.542×10^5	2.527×10^{-8}	99.952	1.729×10^{-9}
			-0.5	3.947×10^3	1.581×10^5	1.541×10^5	2.529×10^{-8}	99.952	1.728×10^{-9}
Figure 69(b).	PTE-PC gAN		-0.6	3.894×10^3	1.540×10^5	1.501×10^5	5.180×10^{-9}	99.951	1.774×10^{-9}
			-0.5	3.243×10^3	1.573×10^5	1.541×10^5	1.274×10^{-8}	99.953	1.728×10^{-9}
Figure 70(a).	PTE-PC gA	1 mM $Eu(NO_3)_3$ / 100 mM KNO_3	-0.6	4.006×10^3	1.574×10^5	1.534×10^5	2.540×10^{-8}	99.953	1.736×10^{-9}
			-0.5	4.007×10^3	1.571×10^5	1.531×10^5	2.545×10^{-8}	99.953	1.739×10^{-9}
Figure 70(b).	PTE-PC gAN		-0.6	3.548×10^3	1.571×10^5	1.536×10^5	2.021×10^{-8}	99.953	1.734×10^{-9}
			-0.5	3.552×10^3	1.575×10^5	1.539×10^5	2.016×10^{-8}	99.953	1.730×10^{-9}

7.4 References

1. L. -E. Cheran, S. Sadeghi and M. Thompson, *Analyst*, 2005, **130**, 1569
2. L. -E. Cheran, M. E. McGovern and M. Thompson, *Faraday Discuss.*, 200, **116**, 23
3. M. Thompson, L. -E. Cheran, M. Zhang, M. Chacko, H. Huo and S. Sadeghi, *Biosensors and Bioelectronics*, 2005, **20**, 1471
4. H. G. L. Costa, T. C. Chilcott and A. C. F. Costa, *Bioelectrochemistry and Bioenergetics*, 1996, **40**, 79
5. H. Fricke and S. Morse, *J. Gen. Physiol.*, 1925, **9**, 153
6. H. G. L. Coster and J. R. Smith, *Biochim. Biophys. Acta*, 1974, **373**, 151
7. R. G. Ashcroft, H. G. L. Coster, D. R. Laver and J. R. Smith, *Biochim. Biophys. Acta*, 1983, **730**, 231
8. C. Whitehouse, D. Gidalevitz, M. Cahuzac, R. E. Koeppe II and A. Nelson, *Langmuir*, 2004, **20**, 9291
9. M. Naumowicz and Z. Figaszewski, *Bioelectrochemistry*, 2003, **61**, 21
10. W. Kleinekofort, A. Pfenninger, T. Plomer, Ch. Griesinger and B. Brutschy, *Int. J. Mass Spectrom. Ion Process.*, 1996, **156**, 195
11. M. Diociaiuti, F. Bordi, A. Motta, A. Carosi, A. Molinari, G. Arancia and C. Coluzza, *Biophys. J.*, 2002, **82**, 3198
12. A. Kemp and C. E. Wenner, *Arch. Biochem. Biophys.*, 1976, **176**, 547
13. H. E. Ries and H. Swift, *J. Colloid Interface Sci.*, 1987, **117**, 584
14. M. Naumowicz, A. D. Petelska and Z. A. Figaszewski, *Electrochim. Acta*, 2006, **51**, 5024
15. A. D. Petelska, M. Naumowicz and Z. A. Figaszewski, *Cell. Biochem. Biophys.*, 2006, **44**, 205
16. A. P. Golovanov, I. L. Barsukov, A. S. Arseniev, V. F. Bystrov, S. V. Suchanov and L. I. Barsukov, *Biopolymers*, 1991, **31**, 425
17. H. W. Huang, *Biochemistry*, 2000, **29**, 8347
18. O. S. Smart, J. Breed, G. R. Smith and M. S. P. Sansom, *Biophys. J.*, 1997, **72**, 1109
19. L. V. Protsailo and W. R. Fawcett, *Electrochim. Acta*, 2000, **45**, 3497
20. E. Sabatani and I. Rubinstein, *J. Electroanal. Chem.*, 1987, **219**, 365
21. R. K. Mendes, R. S. Freire, C. P. Fonseca, S. Neves and L. T. Kubota, *J. Braz. Chem. Soc.*, 2004, **15**, 849
22. F. Macias and M. E. Starzak, *Biochim. Biophys. Acta*, 1993, **1153**, 331

Chapter 8

Conclusions

8.1 Main findings

The purpose of the research presented in this thesis was the design and synthesis of a novel peptide ion channel with controllable, potential-dependent channel switching properties which could be tested by a range of electrochemical techniques and under a range of different physiological conditions.

To this end an analogue of the naturally occurring peptide antibiotic gA has been synthesised. The analogue gAN, comprised of the gA chain C-terminus functionalised with a nicotinamide moiety, has been chosen because its channels are likely candidates to undergo the *ball and chain* model of inactivation.

SECM feedback curves were performed on gAN treated polycarbonate supported BLMs. A range of tip potentials were employed so as to determine the limits of any channel ionic transport. The feedback curves clearly demonstrate that the gAN channels are open, thereby allowing the passage of K^+ ions, at potentials negative of -0.515 ($\pm$ 0.005) V. This is in contrast to unmodified gA channels, normally considered potential-independent, which display similar K^+ conduction properties over a much wider potential range and control membranes, absent of peptide channels, which display insulating properties at all but the most negative of potentials (< 0.9 V) where the membrane is believed to electroporate. The repetitive open-closed switching of the gAN channel was demonstrated by the application of successive potential steps in chronoamperometry. A consistent current response was observed for each successive potential cycle, further confirming the good switch-like characteristics of the gAN channel.

Chronoamperometry also indicated the gAN channel was permeable to Tl^+ ions, which are known to permeate the unmodified gA channel, and impermeable to Eu^{3+} ions, which are known to occlude the gA channel by binding at the channel mouth. The passage of Tl^+ across both gA and gAN has been further observed by SECM feedback measurements using Prussian Blue as a dual-purpose electrolyte and electrochromic indicator. A marked decrease in the absorbance of the *cis*-compartment electrolyte

occurs when a Tl^+ concentration gradient is allowed to flow across the opened gAN channels. We attribute this change in absorbance to the permeation of Tl^+ into the PB unit cell and formation of the corresponding Everitt's Salt. Identical experiments with a K^+ concentration gradient result in a much less pronounced colour change, reflective of the transient nature of the K^+ ions within the PB lattice and differing ES composition.

Cyclic voltammetry was used as a way of monitoring gA and gAN ion transport directly at the electrode surface. For these experiments BLMs were created adsorbed on the gold electrode surface and were treated with the peptide of interest. Passage of Tl^+ ions from the electrolyte, via the gA / gAN channels, to the electrode surface was confirmed by the presence of a $Tl^0 \rightarrow Tl^+$ oxidation peaks at ~ -0.5 V. These peaks are slightly offset from the corresponding peak obtained by an uncoated electrode (at -0.83 V), which is probably due to slower heterogeneous kinetics at the membrane coated electrodes. It is also possible that underpotential deposition (UPD) of thallium on the gold electrode surface plays some role in the kinetics. CV measurements performed with Eu^{3+} as the analyte cation indicate there is no Eu^{3+} transport across either channel type, corroborating the chronoamperometry observations and reinforcing the idea that Eu^{3+} obstructs gramicidin based peptide channels.

As the $Fe(CN)_6^{3-}/Fe(CN)_6^{4-}$ couple was used as mediator in most of the SECM measurements it seemed appropriate to consider this redox process in more detail. CV was used to observe the voltammetric response of the $Fe(CN)_6^{3-}/Fe(CN)_6^{4-}$ couple with variance of the supporting electrolyte cation. The E_{pa}, α and k^o values obtained indicate that either very small or very large electrolyte cations impose a reactant like ($\alpha < 0.5$) transition state on the oxidation reaction by reinforcing the $Fe(CN)_6^{4-}$ ionic structure. Three different methods of calculating the heterogeneous rate constant, k^o_{calc}, were used and all three show a similar trend across the alkali metal cations, namely: $Li^+ < Na^+ < Rb^+ \sim Cs^+ < K^+$. This suggests, notwithstanding the higher than expected position of K^+ within the series, there is a relationship between cation radius and k^o_{calc} value. But a straightforward trend between ionic radius and k^o_{calc} can be discounted by the observation that Tl^+ and Rb^+, of equal charge and similar radius (164 pm vs. 166 pm), result in very different α ($\alpha = 0.514$ vs. 0.671) and k^o_{calc} values ($k^o = 6.50$ vs. 2.80×10^{-3} cms^{-1}). Considering the case of Na^+ and Eu^{3+}, again ions of comparable size (116 pm vs.

108 pm), but resulting in significantly different transition states (α = 0.570 vs. α = 0.357) and heterogeneous kinetics (k^o = 6.51 vs. 1.81 × 10^{-3} cms^{-1}). In this case the differences are likely to be attributable to the differing ionic charges. The relationship between electrolyte cation, k^o and α requires more investigation.

The SKN scans collected clearly demonstrated that inclusion of gA, gAN or alamethicin channels in a gold-supported BLM result in a decrease in CPD compared to the value obtained with an untreated BLM. Alamethicin and gA display similar CPD values (-42 vs. -24 mV), with the alamethicin value slightly suppressed owing to the larger size of the channel lumen. The CPD of a gAN treated BLM lies intermediate between the CPD values for the gA / alamethicin and untreated BLM. This reflects the closed status of the channel under ambient experimental conditions.

EIS measurements performed directly on gAN-treated BLMs show a R_{CT} increase when the working electrode potential is increased from -0.6 V to -0.5 V. The magnitude of this increase is ~ 2 kΩ and ~ 3 kΩ for measurements obtained in $K_3Fe(CN)_6$ and $TlNO_3$ electrolytes respectively. When $Eu(NO_3)_3$ electrolyte is used there is no obvious change in R_{CT} over the same potential increase. In contrast a membrane treated with gA subjected to the same potential increase shows no change in R_{CT} in any of the electrolytes studied. Coverage and C_{DL} values were also calculated for each electrode environment.

The combined data from all of the electrochemical techniques reinforce the proposal that gAN, unlike gA, is a potential-dependent channel that switches from an open conducting state to a closed insulating state over a narrow potential range. SECM feedback curves of gAN in KNO_3 electrolyte pinpoint this transition at -0.515 ± 0.005 V. The good reproducibility of the channel switching behaviour is highlighted by the almost identical current responses when the membrane is exposed to the successive potential pulses of chronoamperometry. The work function of a gold substrate coated with gAN-treated membrane is much greater than the corresponding gA and alamethicin treated membranes, further demonstrating the channel is in the oxidised (closed) state under the ambient conditions of SKN operation. CV and CA both show that Tl^+ ions are able to permeate the open (reduced) gAN channels at potentials negative of -0.515 V. Unlike Tl^+ ions, there is no evidence to suggest that Eu^{3+} ions permeate through gAN channels, which is in agreement with the idea that Eu^{3+} ions occlude the channel by

binding at its entrance. The values of R_{CT} and C_{DL} obtained by EIS are also in agreement with gAN potential-dependent channel switching.

8.2 Future work

Future avenues of research include the development and characterisation of a range C-terminus modified gA analogues, each of slightly differing potential-dependence. This could be achieved by the incorporation of sterically discreet electron-donating or withdrawing groups at various positions of the NAD^+ pyridine ring.

The CV data presented in this thesis also leave an incomplete picture of the relationship between $Fe(CN)_6^{3-}/Fe(CN)_6^{4-}$ couple E_{pa}, α and k^o values. This requires a more thorough investigation by fast scan CV and EIS.

Appendix 1

SECM Feedback Curve Data

The following feedback curves were collected in addition to those previously shown in Chapter 5. These figures were omitted from the main body of text as they show the channel current behaviour outside the range of the gAN potential switching.

Figure 71. *SECM feedback curves.*

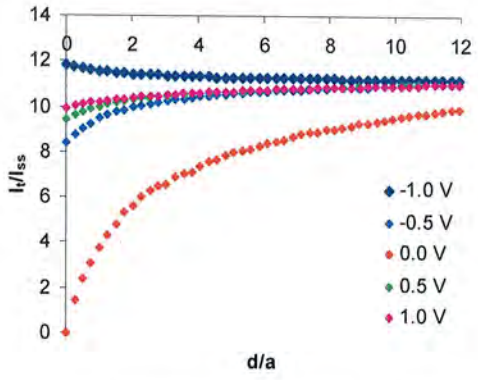

(a) Control membrane in 0.1 mM $K_3Fe(CN)_6$ / 100 mM KCl.

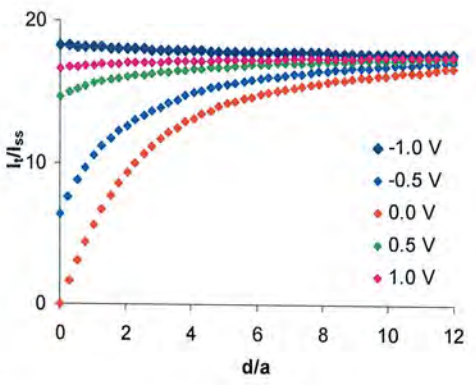

(b) Control membrane in 0.1 mM $K_3Fe(CN)_6$ / 100 mM $N(CH_3)_4Cl$.

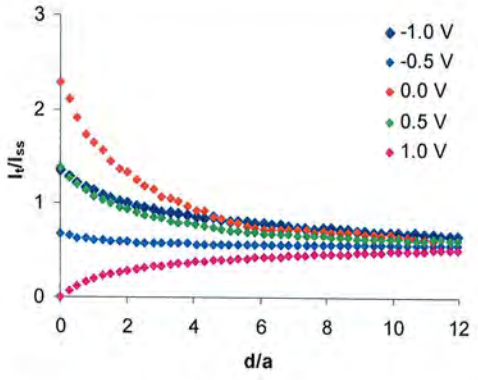

(c) gA membrane in 0.1 mM $K_3Fe(CN)_6$ / 100 mM KCl.

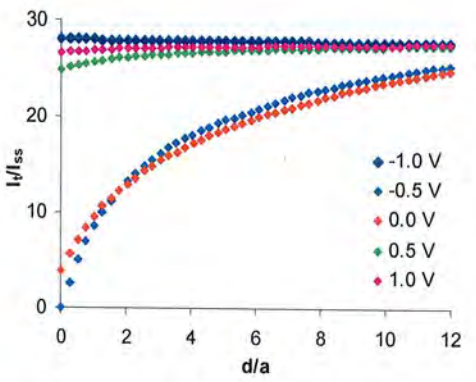

(d) gA membrane in 0.1 mM $K_3Fe(CN)_6$ / 100 mM $N(CH_3)_4Cl$.

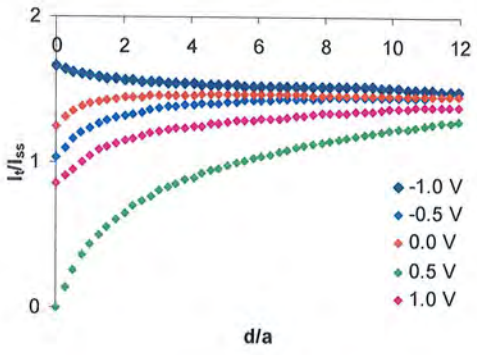

(d) gAN membrane in 0.1 mM $K_3Fe(CN)_6$ / 100 mM KCl.

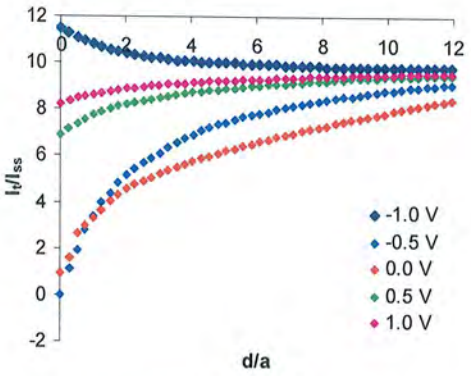

(e) gAN membrane in 0.1 mM $K_3Fe(CN)_6$ / 100 mM $N(CH_3)_4Cl$.

Appendix 2

Fast Scan CV Data

The following preliminary CV data were obtained in the fast scan experiments mentioned at the end of Chapter 6. At scan rates greater than 50 Vs^{-1} the ferricyanide CVs displayed typical characteristics of a capacitive response, where the current density is relatively constant over a wide potential range. The capacitive contribution increased with scan rate.

Figure 73 shows the voltammograms obtained with each supporting electrolyte at 1000 Vs^{-1}. At this scan rate we expected to observe the effect of the background electrolyte on the capacitive current. The slightly diagonal shape of the CVs indicates a small Faradaic contribution to current, but this is masked by the much larger capacitive effect. For each electrolyte the capacitance per unit area (specific capacitance) was calculated using equation 102 and is shown below in Table 11.

$$C_d = \frac{i}{vS} \qquad (102)$$

Where i represents the anodic (or cathodic) current, C_d the capacitance per unit area and S the scan rate.

A point to note is that the cut marks on the voltammograms arise due to the removal of errant data points caused by the equipment overshooting the initial and final values of the potential range.

From the specific capacitance values it can be seen that the minimum capacitances are observed with $LiNO_3$ and $NaNO_3$. This may be related to the size of these ions and their solution resistances. With $TlNO_3$ the redox peaks observed at approximately -0.05 V and 0.025 V are probably due to the Tl^+ / Tl^{3+} redox process. These very preliminary experiments indicate interesting trends, although further experiments will need to be performed to gain a fuller picture of the role of the cation.

Figure 72. *Fast scan CVs of the* $Fe(CN)_6^{3-}/Fe(CN)_6^{4-}$ *couple.*

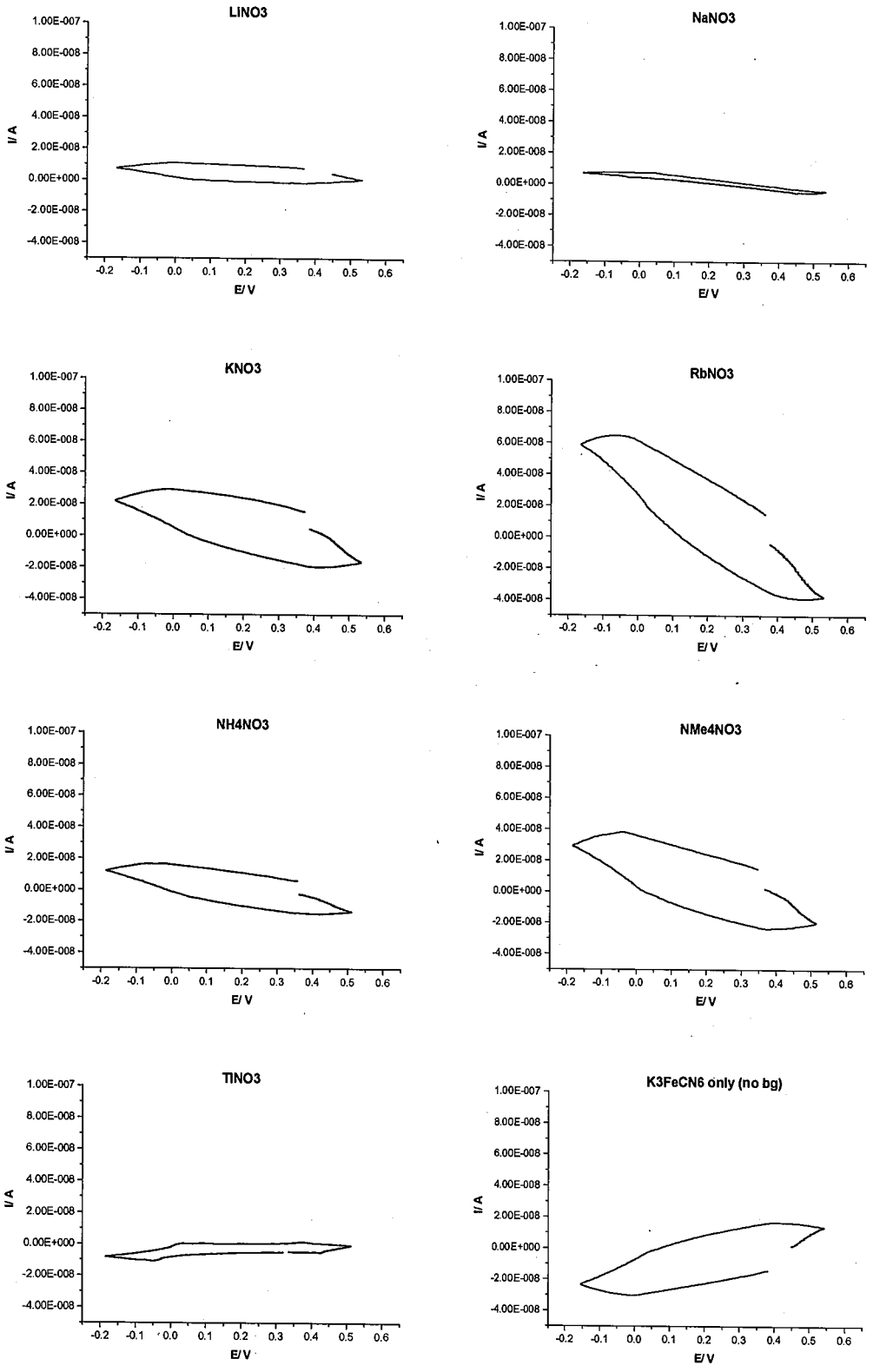

Table 11. *Fast scan CV capacitance data.*

Electrolyte	i_2/ A	i_1/ A	Δi/ A (= i_2 – ([i_2 - i_1]/2))	C/ F (= Δi / ν)	C/ F cm^{-2}
$LiNO_3$	*9.50×10^{-9}*	*-8.68×10^{-10}*	*5.18×10^{-9}*	*5.18×10^{-12}*	*6.60×10^{-6}*
$NaNO_3$	*3.35×10^{-9}*	*7.49×10^{-10}*	*1.30×10^{-9}*	*1.30×10^{-12}*	*1.65×10^{-6}*
KNO_3	*2.40×10^{-8}*	*-1.02×10^{-8}*	*1.71×10^{-8}*	*1.71×10^{-11}*	*2.17×10^{-5}*
$RbNO_3$	*3.72×10^{-8}*	*-1.17×10^{-8}*	*2.45×10^{-8}*	*2.45×10^{-11}*	*3.12×10^{-5}*
NH_4NO_3	*1.10 × 10-8*	*-1.02×10^{-8}*	*1.06×10^{-8}*	*1.06×10^{-11}*	*1.35×10^{-5}*
NMe_4NO_3	*2.42×10^{-8}*	*-1.43×10^{-8}*	*1.93×10^{-8}*	*1.93×10^{-11}*	*2.45×10^{-5}*
$TlNO_3$	*-5.44×10^{-9}*	*2.90×10^{-10}*	*-2.86×10^{-9}*	*-2.86×10^{-12}*	*-3.65×10^{-6}*
$K_3Fe(CN)_6$ only	*-2.24×10^{-8}*	*8.44×10^{-9}*	*-1.54×10^{-8}*	*-1.54×10^{-11}*	*-1.96×10^{-5}*

Appendix 3

Conferences, Lecture Courses and Colloquia

1. Lecture courses completed between 1st October 2003 and 30th September 2006:

   (a) *Medicinal Chemistry*, Dr. S. J. Cooper, Dr. P. G. Steel and Dr. J. A. G. Williams.

   (b) *Electroanalytical Techniques*, Dr. R. Kataky.

2. Conferences attended between 1st October 2003 and 30th September 2006:

   (a) *BioNEt Advanced Protein Characterisation Workshop* (University of Newcastle upon Tyne, UK), 18th December 2003.

   (b) *New Developments in Potentiometric Analysis: Towards Lower Levels of Detection and Higher Precision* (University of Durham, UK), 31st March – 1st April 2004 (Poster presentation).

   (c) *7th International Synopsium on Bio-Organic Chemistry* (University of Sheffield, UK), 27th June – 1st July 2004 (Poster presentation).

   (d) *Electrochem 2004* (University of Leicester, UK), 13th – 15th September 2004 (Poster presentation).

   (e) *Particle Characterisation: New Electroanalytical Opportunities* (LGC, Runcorn, UK), 23rd March 2005.

   (f) *BioNEt Meeting: Introducing the New Centre for Bioactive Chemistry at Durham* (University of Durham, UK), 20th April 2005 (Poster presentation).

   (g) *BioNEt Meeting: Bioimaging and Informatics: Across the Spectrum* (University of Newcastle upon Tyne, UK), 16th May 2005 (Poster presentation).

   (h) *BioNEt Meeting: Chemical Genetics* (University of Durham, UK), 24th June 2005.

   (i) *Electrochem 2005* (Northumbria University, UK), 4th – 7th September 2005 (Poster presentation).

(j) *4th Postgraduate Research Topics in Electroanalysis* (Birkbeck College, University of London, UK), 30th November 2005 (Oral presentation).

(k) *BioNEt Meeting: Natural Product Isolation, Synthesis and Applications of Natural Products as Potential Medicines* (University of Durham, UK), 16th January 2006.

(l) *New Perspectives in Voltammetry* (University of Bath, UK), 3rd April 2006.

(m) *Electrochem 2006* (Heriot Watt University, UK), 27th August – 1st September 2006.

(n) *Robin Hood Interdisciplinary Network in Electrochemistry (RHINE) Meeting* (University of Hull, UK), 13th December 2006 (Poster presentation).

3. Royal Society of Chemistry lectures and postgraduate colloquia attended between 1st October 2003 and 30th September 2006:

(a) *Applications of Catalytic Asymmetric C-H Activation to Organic Systems*, Prof. H. Davies (University of Buffalo, US), 15th October 2003.

(b) *Homogeneous Catalysis: A Key Technology for Environmentally Benign Synthesis of Fine Chemicals and Pharmaceuticals*, Dr. M. Beller (Inst. für Organische Katalyseforschung an der Universität Rostock, Germany), 22nd October 2003.

(c) *Urease... A Muse for the Coordination Chemist*, Dr. D. Fenton (University of Sheffield, UK), 18th November 2003.

(d) *Customising Selection Rules in Solid-State NMR and the Determination of Biomolecular Structures*, Dr. M. Levitt (School of Chemistry, Southampton University, UK), 3rd December 2003.

(e) *Arrays and Combinatorial Chemistry*, Prof. M. Bradley (School of Chemistry, Southampton University, UK), 21st January 2004.

(f) *Electrochemical and Spectroelectrochemical Studies of Transition Metal Complexes*, Dr. L. Yellowlees (Department of Chemistry, Edinburgh University, UK), 28th January 2004.

(g) *Quantum Dots: Realising the Potential*, Prof. P. O'Brien (Department of Chemistry, University of Manchester, UK), 4th February 2004.

(h) *Luminescent Molecules as Information Processors*, Prof. A. P. de Silva (Queen's University, Belfast, UK), 17th February 2004.

(i) *Protein Folding and Misfolding From an NMR Perspective*, Prof. J. Waltho (Molecular Biology and Biochemistry, University of Sheffield, UK), 18th February 2004.

(j) *Bottom-Up Assembly of Peptide-Based Supramolecular and Nanoscale Structures*, Dr. D. N. Woolfson (Department of Biochemistry, University of Sussex, UK), 24th March 2004.

(k) *Supramolecular Chemistry: Concepts and Perspectives*, Prof. J. -M. Lehn (Collége de France, Paris), 24th June 2004.

(l) *Telomerase and Telometric DNA: New Targets for Chemical Biology*, Prof. S. Niedle (School of Pharmacy, University of London, UK), 19th October 2004.

(m) *Light Relief*, Prof. D. Phillips (Imperial College, University of London, UK), 16th November 2004.

(n) *Recent Advances in the Total Synthesis of Antibiotic Natural Products*, Prof. T. Barnett (Department of Chemistry, Imperial College, London, UK), 23rd November 2004.

(o) *Hydrogenases: Electrocatalysis and Implications for Future Energy Technology*, Prof. F. Armstrong (Department of Chemistry, University of Oxford, UK), 27th April 2005.

(p) *Electrochemical Imaging of Carbon Based Materials – from Single Walled Carbon Nanotubes to Diamond*, Dr. J. V. MacPherson (Department of Chemistry, University of Warwick, UK), 4th October 2005.